POLITECNICO DI TORINO

Master of Science in Automotive Engineering



Master's Degree Thesis

Computationally Efficient Modelling of Electric Vehicle Thermal Systems

Supervisor:

Candidate:

SORNIOTTI ALDO
VELARDOCCHIA MAURO
CIRAVEGNA LUCA
ALBERTI FABIO

Francesca DELLEANI

Abstract

The increasing adoption of electric vehicles and stringent global sustainability targets highlighted the challenge of improving energy efficiency, particularly through an optimisation of the thermal management system. Considering this, the aim of this thesis is to develop in Matlab/Simulink a model of the Thermal Management System (TMS) that can serve as a foundation for the future implementation of a Model Predictive Control (MPC) strategy, designed to maximise energy efficiency while keeping the battery and cabin within the desired thermal limits.

To achieve this, two complementary modelling approaches are developed: a Physics-based model and a data-driven model.

The Physics-based model is based on fundamental thermodynamic laws and is implemented using simplified equations. Its main advantage lies in being usable immediately, in complete independence from a possible database. The model is validated through a comparison with a MathWorks Simscape reference model, demonstrating an optimal compromise between accuracy and computational efficiency, with ten times less simulation time.

The data-driven model, on the other hand, uses neural networks trained on EFFEREST experimental data to capture the system's complex nonlinear relationships under different operating conditions, including battery heating/cooling and cabin climate control.

The results of the study are analysed and discussed in the final chapter. The simplified Physics-based model offers generalizability and fast execution times (about 0.7 seconds), showing decent alignment with the Simscape reference model, which takes 71 seconds per simulation. The data-driven model provides a better estimation of the thermal management system and higher computational performance (0.2 seconds). However, this approach is highly dependent on the training dataset, thus requiring a large amount of data across different operating conditions.

Through detailed benchmarking, this work provides not only a robust modelling foundation for the future development of predictive control strategies, but also operational guidelines for selecting the most suitable approach based on specific design requirements, paving the way for electric vehicles with greater range and optimized thermal performance.

Index

1.	Intro	duction	1
	Therma	al Management in Electric Vehicles	1
	Current	Challenges: Range, Efficiency, and Consumer Perception	2
	Therma	al Management in BEVs: Challenges and Opportunities	3
	Objecti	ves and Structure of the Research	4
2.	Ther	mal energy management system	5
	Therma	al Management in Electric Vehicles	5
	System	setup	6
	Lithium	n-ion batteries	12
3.	Phys	ics-Based Modelling of Thermal Models	13
	3.1	Methodological Approach	13
	3.2	Vehicle & Powertrain Thermal Interactions	14
	3.3	Cabin thermal model	17
	3.4	Lithium-Ion Battery Model	19
	3.5	Refrigerant circuit	27
	3.6	Bench models	43
	3.6.1	Condenser	43
	3.6.2	Evaporator	49
	3.6.3	Expansion valve	54
	3.6.4	Compressor bench	59
4.	Neur	al Network-Based Modelling of Thermal Models	63
	4.1	Methodological Approach	63
	4.2	Battery Heating mode (BH)	64
	4.3	Battery Cooling mode (BC)	80
	4.4	Cabin Cooling mode (CC)	98
	4.5	Cabin Heating mode (CH)	104
	4.6	Integrated Model for Thermal Modes	111
5.	Com	parative Analysis of Physics-Based and Neural Network Modelling Approaches	115
6.	Conc	lusion	118
Ві	ibliogran	phv	121

Figure List

Figure 1 Projected global well-to-wheel CO2 emissions from road transport compared with an emissions pathway compatible with Paris Agreement goals of keeping warming under 2 $^{\circ}$ C (Mo	ultak,
2017)	
Figure 2 Global electric car stock trends 2010-2023 (International Energy Agency (IEA), 2024)	
Figure 3 Impact of extreme temperatures on electric vehicle battery range during summer and v	
conditions (Najman, 2022; Career, 2025)	
Figure 4 Operating Temperatures for Vehicle Components (Holcomb, 2022)	
Figure 5 ZTEM (Lokur, Murgovski, & Larsson, 2024)	
Figure 6 Pressure-Enthalpy chart of the refrigerant fluid (Lokur, Murgovski, & Larsson, 2024)	
Figure 7 Thermal management system without heat pump in cold weather condition	
Figure 8 Thermal management system with heat pump in cold weather condition	
Figure 9 Driving range in cold ambient temperatures- comparison of heating methods (UFI Filte	r,
2023)	
Figure 10 Cabin setup (Lokur, Murgovski, & Larsson, 2024)	
Figure 11 Equivalent circuit of lithium-ion battery (Gao, Liu, & Dougal, 2002)	
Figure 12 Rate factor (Gao, Liu, & Dougal, 2002)	
Figure 13 Temperature factor and temperature-dependent potential-correction term	
Figure 14 Electrical battery model	
Figure 15 Transient response of the battery	
Figure 16 Thermal battery model	
Figure 17 Battery model	
Figure 18 Battery simulation: Tamb = 23°C; Tbatt = 20°C	
Figure 19 Battery simulation: Tamb = 23°C; Tbatt = 0°C	
Figure 20 Battery simulation: Tamb = 0°C; Tbatt = 20°C	
Figure 21 Refrigerant circuit model	
Figure 22 Computational time in the refrigerant circuit model	
Figure 23 Electric vehicle thermal management (Electric Vehicle Thermal Management, s.d.)	
Figure 24 Computational time in the Electric vehicle thermal management	
Figure 25 Compressor block (Electric Vehicle Thermal Management, s.d.)	
Figure 26 Condenser block (Electric Vehicle Thermal Management, s.d.)	
Figure 27 Expansion valve block (Electric Vehicle Thermal Management, s.d.)	
Figure 28 Evaporator block (Electric Vehicle Thermal Management, s.d.)	
Figure 29 Energy balance - Simscape model	
Figure 30 Energy balance – Physics-based model	
Figure 31 Pressure response - Simscape model	
Figure 32 Temperature response - Simscape model	
Figure 33 Power response - Simscape model	
Figure 34 Power vs refrigerant mass flow rate – Simscape	
Figure 35 Power vs refrigerant mass flow rate – Physics-based model	
Figure 36 Power vs air mass flow rate – Simscape	
Figure 37 Power vs air mass flow rate – Physics-based model	
Figure 38 p-T diagram - Simscape	
Figure 39 p-T diagram – Physis-based model	
Figure 40 p-T diagram - Physics-based model	
FIRMLE 4. CONDENSE DENCH CONDENSE AND EVADORATOR S.O.T	43

Figure 42 Condenser heat transfer rate over refrigerant mass flow	<i>r</i> rate 45
Figure 43 Condenser heat transfer rate over fan speed	45
Figure 44 Condenser heat transfer rate over refrigerant pressure	46
Figure 45 Condenser heat transfer rate over refrigerant inlet tem	
Figure 46 Condenser heat transfer rate over refrigerant outlet ter	
Figure 47 Condenser LUT	
Figure 48 3D Map of Q _{condenser} (P,T _B) for different mr	48
Figure 49 Evaporator Bench (MathWorks, s.d.)	
Figure 50 Evaporator heat transfer rate over refrigerant mass flov	
Figure 51 Evaporator heat transfer rate over air mass flow rate	
Figure 52 Evaporator heat transfer rate over refrigerant pressure	
Figure 53 Evaporator heat transfer rate over refrigerant inlet tem	
Figure 54 Evaporator heat transfer rate over refrigerant outlet ter	
Figure 55 Evaporator LUT	
Figure 56 3D Map of Qevaporator(P, T_D) for different mr	
Figure 57 Expansion valve bench	
Figure 58 Expansion valve pressure drop over refrigerant mass flo	
Figure 59 Expansion valve pressure drop over refrigerant inlet pre	
Figure 60 Expansion valve pressure drop over refrigerant inlet ter	
Figure 61 Expansion valve LUT	
Figure 62 3D Map of Δ P(Pin,TC) for different mr	
Figure 63 Compressor Bench	
Figure 64 Compressor work over pressure ratio	
Figure 65 Compressor work over inlet temperature	
Figure 66 Compressor work over rotational speed	
Figure 67 LUT Compressor	
Figure 68 3D map of $Wcompressor$ for different $\omega/\omega max$	
Figure 69 EFFEREST circuit model	
Figure 70 Neural network architecture for Battery Heating mode:	
Figure 71 Training and validation loss over epochs for NN dTbatt/	
Figure 72 dTbatt/dt: Test output vs NN prediction	
Figure 73 dTbatt/dt - qualitative analysis: Test output vs NN prediction	
Figure 74 Simulink model for testing dTbatt/dt Neural Network	
Figure 75 Sensitivity analysis - computational time comparison	
Figure 76 Derivative of the battery temperature (dTbatt/dt) over	
network.	
Figure 77 Battery temperature (Tbatt) over time	
Figure 78 Neural network architecture for Battery Heating mode:	
Figure 79 Training and validation loss over epochs for NN Pel	
Figure 80 Pel: Test output vs NN prediction	
Figure 81 Pel- qualitative analysis: Test output vs NN prediction	
Figure 82 Simulink model for testing Pel and dTbatt/dt Neural Ne	
Figure 83 Electric power (Pel) over time	
Figure 84 Neural network architecture for Battery Heating mode:	
Figure 85 Training and validation loss over epochs for NN Pel	
Figure 86 Pel- qualitative analysis: Test output vs NN prediction	
Figure 87 Electric power (Pel) over time	
Figure 88 NN a	

Figure 89 NN b	84
Figure 90 NN c	84
Figure 91 Training and validation loss over epochs for NN dTbatt/dt	85
Figure 92 dTbatt/dt - qualitative analysis: Test output vs NN prediction	86
Figure 93 NN A	93
Figure 94 NN B	93
Figure 95 NN C	93
Figure 96 NN D	94
Figure 97 NN E	94
Figure 98 NN F	94
Figure 99 NN G	95
Figure 100 NN H	95
Figure 101 Training and validation loss over epochs for NN Pel	97
Figure 102 Pel- qualitative analysis: Test output vs NN prediction	97
Figure 103 NN L	101
Figure 104 NN M	102
Figure 105 NN N	102
Figure 106 Training and validation loss over epochs for NN Pel	103
Figure 107 Pel- qualitative analysis: Test output vs NN prediction	104
Figure 108 NN P	108
Figure 109 NN Q	108
Figure 110 NN R	109
Figure 111 Training and validation loss over epochs for NN Pel	110
Figure 112 Pel- qualitative analysis: Test output vs NN prediction	110
Figure 113 Unified Simulink model covering all four modes	111
Figure 114 Computational time across different modes	113
Figure 115 Neural network results and real data for the different modes (in order: BH, BC	. CC. CH) 114

Table List

Table 1 Condenser bench operating variables	44
Table 2 Evaporator bench operating variables	50
Table 3 Expansion valve bench operating variables	55
Table 4 Compressor bench operating variables	60
Table 5 Sensitivity analysis dTbatt/dt	70
Table 6 Sensitivity analysis dTbatt/dt and Pel	75
Table 7 RMSE values for different simulation of Pel	79
Table 8 Testing and simulation RMSE for each Battery Cooling dTbatt/dt neural network configura	ation
	83
Table 9 Testing and simulation RMSE for each Battery Cooling Pel neural network configuration .	92
Table 10 Testing and simulation RMSE for each Cabin Cooling neural network configuration	100
Table 11 Testing and simulation RMSE for each Cabin Heating neural network configuration	107
Table 12 Computation Time & RMSE Across Modes and Inputs	113

1. Introduction

Thermal Management in Electric Vehicles

The motor sector has been fundamentally reshaped over recent decades, driven by the dual necessity of reducing greenhouse gas emissions and phasing out fossil fuels. The internal combustion engine, that has powered mobility for the last few centuries, is now struggling to meet stringent new demands for sustainability and energy efficiency (International Energy Agency (IEA), 2024). Hence, the change to alternative propulsion systems, especially electric ones, is considered a global strategic move of the extreme importance (Moultak, 2017).

International environmental policies are strongly supporting the transition to more eco-friendly transportation. In line with the Green Deal objectives, the European Union has established that, from the year 2035 onwards, only zero-emission vehicles will be able to be registered.

(European Commission, Fit for 55, 2021). Furthermore, current regulations mandate a reduction in average CO_2 emissions for new vehicles by 15% by 2025 and 37.5% by 2030, compared to 2021 levels (Regulation (EU) 2019/631).

Globally, a similar regulatory trajectory is taking shape. Recent analyses of policies adopted up to 2024 suggest a potential peak in road transport CO₂ emissions around 2025, followed by a steady decline. Compared to previous projections, this shift could result in up to 23 billion tonnes of avoided cumulative emissions by 2050, with an additional 13 billion tonnes potentially avoided if current national targets are fully achieved. However, a substantial gap remains between these projections and the more ambitious pathway required to meet the Paris Agreement goals, highlighting an urgent need for more decisive and coordinated global action.

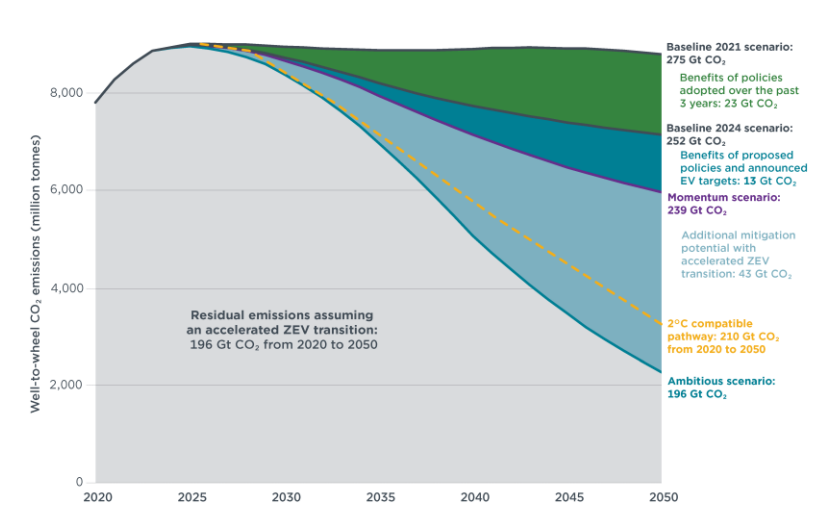


Figure 1 Projected global well-to-wheel CO2 emissions from road transport compared with an emissions pathway compatible with Paris Agreement goals of keeping warming under 2 °C (Moultak, 2017)

In the pursuit of deep decarbonization for transport, battery electric vehicles (BEVs) have emerged as a leading technological pathway. Their rapid market uptake is being driven not only by policy measures but also by continuous technological advancements in order to improve their performance and affordability. This momentum is reflected in the data: global new registrations for BEVs surged to around 14 million in 2023, a striking 35% year-on-year increase that pushed the total number on the world's roads to over 40 million (International Energy Agency (IEA), 2024). Looking ahead, Bloomberg NEF projects that this trend will continue to accelerate, with battery electric vehicles (BEVs) expected to account for approximately 34% of global passenger car sales by 2032 (BloombergNEF, 2024).

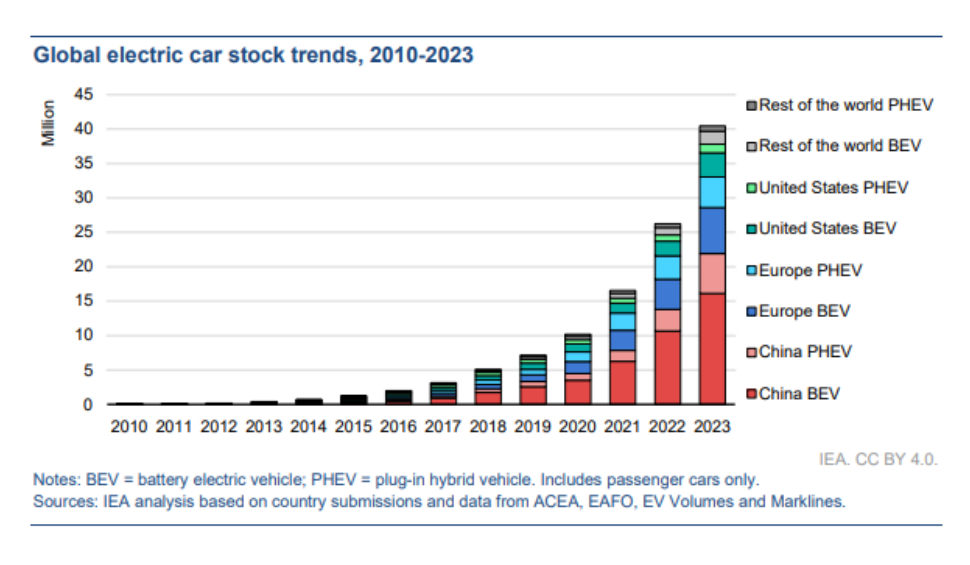


Figure 2 Global electric car stock trends 2010-2023 (International Energy Agency (IEA), 2024)

This growth has been enabled by multiple technological and infrastructural factors: increased energy density of lithium-ion batteries, improvements in power electronics efficiency, and the widespread deployment of public and private charging networks (Funke & al., 2019). However, the diffusion of BEVs does not simply represent a substitution of the thermal engine; rather, it signifies a systemic shift involving the entire value chain—from vehicle design and manufacturing to energy management, logistics, and strategic materials.

Current Challenges: Range, Efficiency, and Consumer Perception

Despite significant progress, the widespread adoption of electric vehicles continues to face technical and conceptual challenges. One of the main obstacles is so-called "range anxiety," which refers to the fear of limited residual driving range and the perceived lack of charging infrastructure (Nicholas, 2020). This psychological barrier is intensified by a general unfamiliarity

with EV technology and the practical challenges of planning long journeys within the constraints of a still-developing charging network. While equipping vehicles with larger batteries seems an obvious solution to alleviate range concerns, this approach introduces significant trade-offs. It negatively impacts manufacturing cost, overall vehicle weight, charging duration, and the total environmental footprint of the vehicle (Neubauer & Wood, 2014). Consequently, research efforts are increasingly focused on optimizing energy consumption, aiming to improve the overall vehicle system efficiency without increasing nominal energy capacity.

Thermal Management in BEVs: Challenges and Opportunities

One of the main factors influencing the operational efficiency of a BEV is the Thermal Energy Management system (TEM), which represents the second largest energy consumer after the propulsion system (Lokur & al., 2024). This system is responsible for regulating the thermal balance of three critical subsystems:

- The passenger cabin, to ensure occupant comfort in all climatic conditions;
- The battery pack, which must operate within an optimal temperature range (typically 20–40°C) to guarantee efficiency, safety, and longevity (Kim, Oh, & Lee, 2019);
- The electric propulsion unit, comprising the motor and inverter, which requires heat dissipation to prevent performance drops and damage (Kim, Oh, & Lee, 2019).

In extreme environments, thermal management can drastically impact vehicle range. According to several studies, the HVAC usage can alone reduce driving range by 30% and 35% (Luo & al., 2020). The impact can be even more severe, as demonstrated by testing on a Ford Focus Electric, which exhibited range reductions of 53.7% in extreme heat and 59.3% in severe cold under the UDDS driving cycle (Jeffers & al., 2015).

Beyond this immediate range penalty, inefficient thermal management accelerates battery degradation. The alternating thermal and mechanical load cycles accelerate cycle aging phenomena, causing mechanical stress, increased internal resistance, and capacity degradation (Ma, et al., 2018) (Dubarry & Liaw, 2009). Consequently, optimizing the thermal management system is not merely a performance enhancement but a critical engineering imperative for extending vehicle lifespan and improving its overall sustainability.

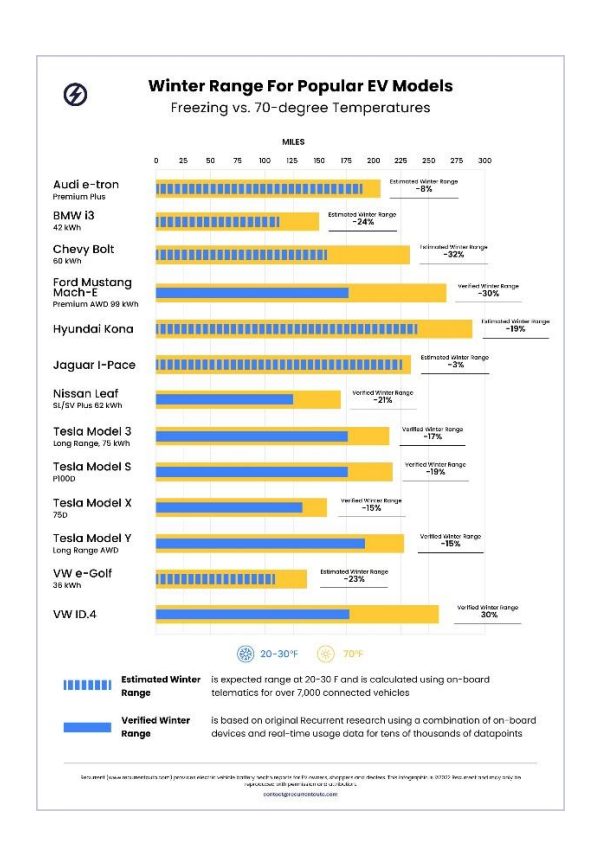


Figure 3 Impact of extreme temperatures on electric vehicle battery range during summer and winter conditions (Najman, 2022; Career, 2025)

Objectives and Structure of the Research

Motivated by the challenges associated with thermal management in electric vehicles, this thesis focuses on developing accurate predictive models capable of describing the thermal behaviour of key vehicle subsystems under real-world operating conditions.

The models target two main domains:

- The passenger cabin, where thermal management affects comfort and energy consumption;
- The battery pack, where maintaining optimal temperature conditions is essential for performance, safety, and lifespan.

The thermal management system is modelled using two complementary approaches: a **physics-based model**, which provides an accurate representation of energy dynamics, and a **data-driven model with neural networks**, which offers a computationally efficient alternative for real-time applications.

2. Thermal energy management system

Thermal Management in Electric Vehicles

The thermal management system is a fundamental component for ensuring vehicle performance, efficiency, and operational safety. Many powertrain components produce heat that must be dissipated through a refrigerant circuit to keep the components within their optimal operating temperature range, thereby optimizing their function and preventing damage.

In the electric vehicle, the primary waste heat transferred to the coolant comes from the motor, power electronics, and battery. As can be seen from the figure below, the ideal battery temperature range is between 20°C and 40°C, while the motor and power electronics can operate at higher temperatures in the range of 20°C to 150°C. Consequently, only the battery requires additional cooling, so there is a dedicated loop connected to the main one by means of a chiller. Cooling this smaller loop below ambient temperature rather than the full cooling loop would require less energy to run the compressor, which increases the vehicle's range. (Holcomb, 2022)

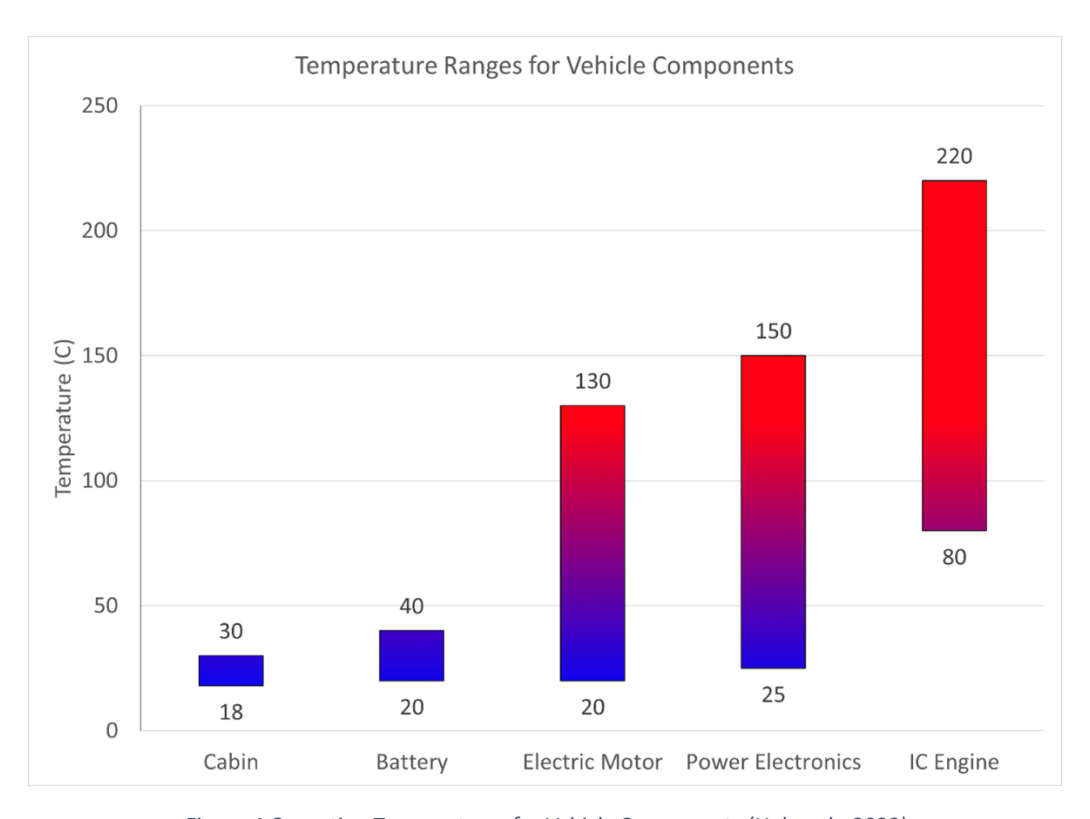


Figure 4 Operating Temperatures for Vehicle Components (Holcomb, 2022)

Additionally, the thermal management system serves a crucial purpose in maintaining cabin comfort. The waste heat extracted from the powertrain components can be used to heat the cabin, further enhancing energy efficiency. In cold environments, the battery can be heated using

an auxiliary heater, a heat pump, or by repurposing waste heat from the motor and power electronics.

System setup

This section introduces Zeekr Technology Europe's thermal energy management system (ZTEM) and cabin setup. The following picture illustrates the configuration where hot air from the condenser is expelled outside the cabin, while cold air from the evaporator is directed into the cabin. (Lokur, Murgovski, & Larsson, 2024)

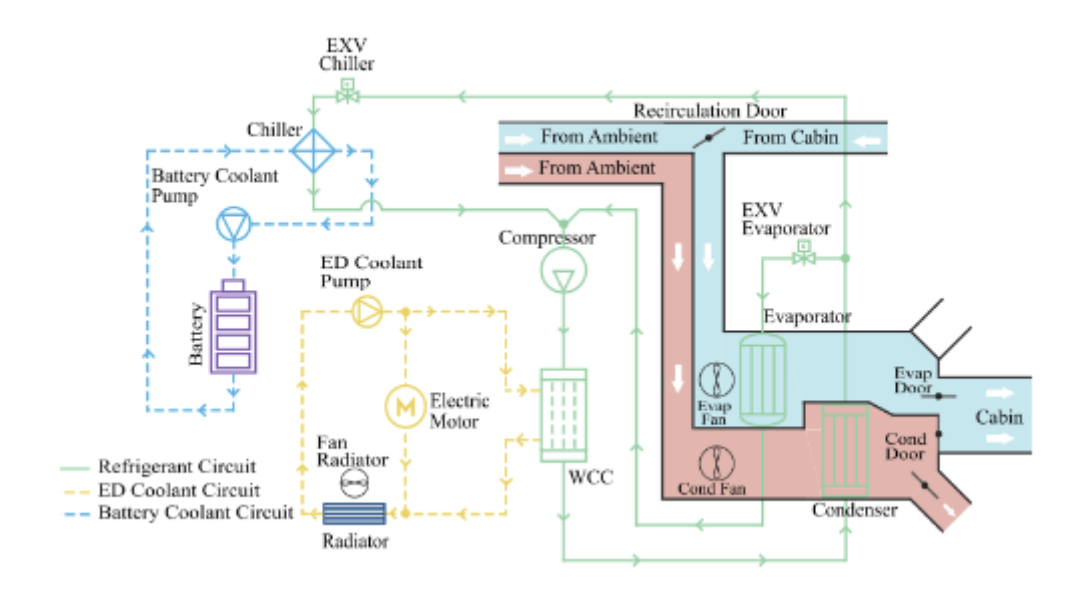


Figure 5 ZTEM (Lokur, Murgovski, & Larsson, 2024)

As it is possible to see from the picture, The ZTEM consists of:

- **Battery Coolant Circuit:** defined in blue, this circuit is responsible for maintaining the battery pack within the optimal temperature range. The main components are:
 - Chiller: connects to the main refrigerant circuit and helps regulate the temperature by absorbing excess heat from the battery pack.
 - Battery Cooling Plate: a flat heat exchanger located beneath the battery pack, in direct thermal contact with the cells. Heat generated within the cells is transferred to the coolant circulating through the plate.
 - Battery Coolant Pump: circulates the coolant within the battery loop, ensuring continuous flow through the cooling plate and the chiller.
- **ED** coolant circuit: in green, this circuit is dedicated to the thermal management of the electric motor and inverter, which generate heat due to electrical and magnetic losses.

The main components of this circuit are:

- E-Motor: Generates propulsion and produces heat during operation, requiring active cooling.
- E-Drive Coolant Pump: Generates coolant flow through the e-drive loop, enabling
 effective heat transfer from the motor, inverter, and DC-DC converter toward the
 radiator or the water-cooled condenser (WCC).
- Radiator: Dissipates thermal energy from the coolant to the ambient air. This is the primary point of heat rejection for the system.
- Radiator Fan: Forces airflow through the radiator, ensuring sufficient heat rejection, especially at low vehicle speeds or during idle conditions.
- *refrigerant circuit*: represented with the green loop, it is regulated through a vapor compressor refrigeration (VCR) cycle, which usually use as refrigerant the R134a. Constituting the base of the HVAC system, it presents the following components:
 - Compressor: generates the refrigerant mass flow rate, while simultaneously increasing the fluid pressure and temperature.
 - Water-Cooled Condenser (WCC): a condenser integrated with the e-drive coolant loop. It allows the refrigerant to transfer heat to the ED coolant, promoting thermal coupling between subsystems and improving system flexibility.
 - Condenser: enables heat rejection to the environment (air-cooled). Inside the condenser, the refrigerant undergoes a phase change from high-pressure vapor to liquid, releasing thermal energy.
 - Expansion valve (electronic EXV): reduces the refrigerant pressure downstream of the condenser and upstream of the evaporator (or chiller). This pressure drop results in a significant reduction of refrigerant temperature, enabling evaporation. Electronic valves allow fine control of refrigerant flow.
 - Evaporator: absorbs heat from the air allowing the refrigerant to evaporate, transitioning from liquid to vapor at low pressure.
 - Chiller: a heat exchanger between the refrigerant and the battery coolant. It allows
 the refrigerant to remove heat from the battery loop, providing active cooling of the
 battery pack.

The refrigerant cycle can be easily visualized with a pressure-enthalpy diagram. The saturation curve separates the regions of compressed liquid (to the left), superheated vapor (to the right), and the two-phase mixture (below the dome).

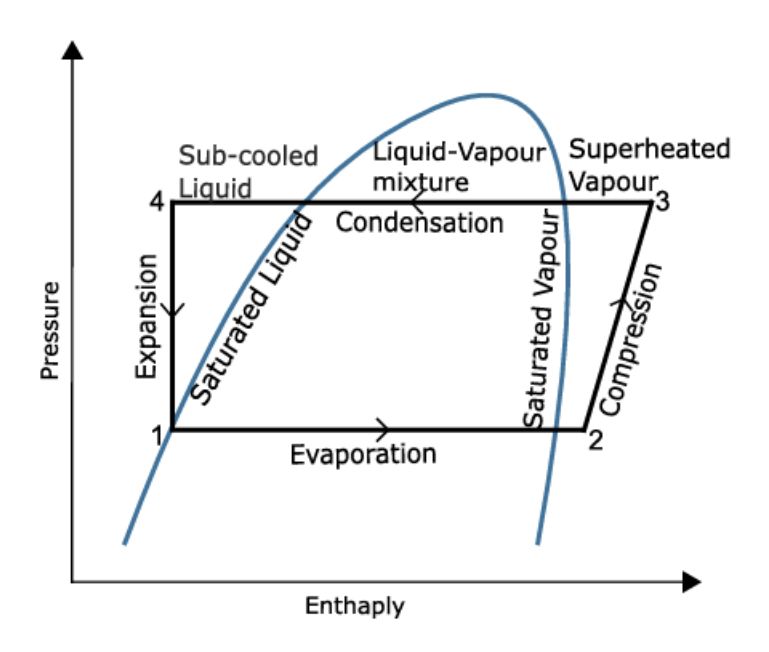


Figure 6 Pressure-Enthalpy chart of the refrigerant fluid (Lokur, Murgovski, & Larsson, 2024)

At point 2, the fluid is in a superheated vapor state. During isentropic compression, it reaches a high-pressure, high-temperature superheated vapor state at point 3. The work of the compressor (*Wcompressor*) is defined as the enthalpy difference (h3–h2).

Next, the fluid enters the condenser, where two phases occur. First, there is *desuperheating*, where the vapor is cooled at constant pressure until it reaches the saturated vapor line. This is followed by condensation at constant temperature and pressure, where the vapor condenses into a liquid. At point 4, the liquid reaches a subcooled condition, which is controlled by the expansion valve. During the 3-4 transition, the fluid rejects heat to the surroundings, which is defined as *Qcondenser* (h4-h3).

Afterward, the high-pressure liquid enters the expansion valve, where it undergoes an isenthalpic process. On the diagram, this is represented by a vertical line, as the pressure drop depends solely on the restriction of the valve, resulting in no work and no heat transfer. At point 1, the liquid-vapor mixture enters the evaporator, where it absorbs heat from the surroundings (*Qevaporator* = h2-h1) and boils at constant pressure and temperature, returning to point 2.

The integration of these subsystems, facilitated by two 4-way valves, creates a flexible thermal management system. This allows thermal energy to be redirected between the cabin, battery, and powertrain circuits, enabling the system to adapt efficiently to varying demands and prioritize between comfort and performance.

Working conditions

The operational strategy of the thermal management system shifts significantly based on external ambient conditions, dictated by divergent thermal needs.

- Under hot weather conditions, the priorities are cooling and heat dissipation. The Air Conditioning system is activated to cool the cabin for occupant comfort, while simultaneous and active cooling of the battery and the electric motor is required to prevent overheating and maintain performance and longevity. In this mode, represented in Figure 5 ZTEM, the chiller is active and guarantees heat rejection from the battery coolant circuit to the refrigerant cycle. The WCC's role is diminished, and it can be bypassed by adjusting the mass flow rate in the electric motor circuit, which is itself maintained within its optimal operating range by rejecting heat directly to the ambient air via the radiator. To provide cabin comfort, the A/C system is active, and the air handling dampers are set to open the path connected to the cold evaporator, as shown in the reference diagram. All heat extracted by the evaporator and the battery chiller is ultimately rejected to the external environment by the condenser.
- Under cold weather conditions, the system's primary objectives are heating and thermal
 maintenance. It must raise the cabin air temperature to ensure passenger comfort and,
 crucially, increase the temperature of the battery and the electric motor to bring them
 into their optimal, efficient operating range.

Configuration without heat pump

The first configuration presented is without the heat pump mode, therefore cabin heating during winter conditions is uniquely provided by a *PTC heater* (Positive Temperature Coefficient heater), which is an electrical resistance that directly converts electrical energy into heat. In this mode, the refrigerant circuit is not reversed, and the compressor is not employed for cabin heating, but it remains active to ensure battery or electric component thermal management through the chiller and the water-cooled condenser. Consequently, the air directed into the cabin is heated solely by the PTC element, which results in high energy consumption and a reduction in vehicle range.

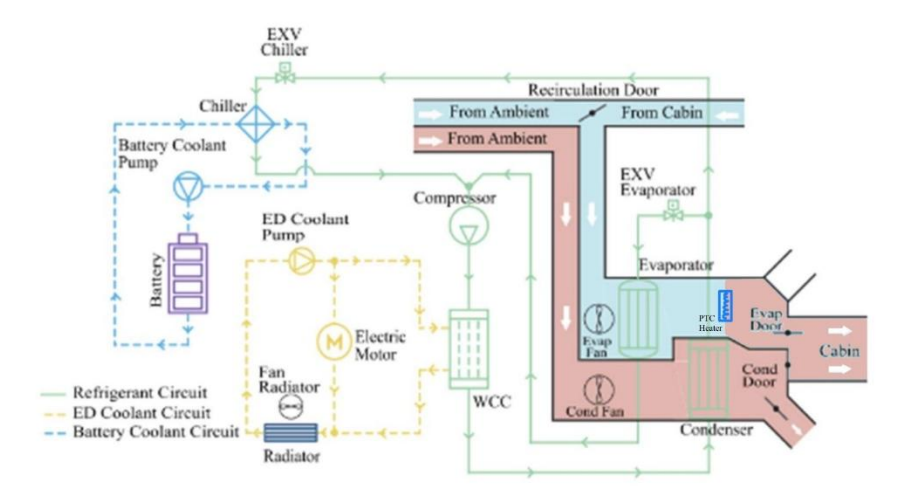


Figure 7 Thermal management system without heat pump in cold weather condition

Configuration with heat pump

In contrast, the **configuration with a heat pump** is specifically designed to operate with a **reversible refrigerant cycle**, made possible by the inclusion of a **four-way valve** that allows the inversion of the refrigerant flow. This strategic reversal allows *waste heat from the electric powertrain* to become the *primary thermal source*, significantly reducing the energy required for heating compared to reliance on PTC heaters alone (UFI Filter, 2023), though these electric heaters are retained for rapid initial warming or supplemental heat during extreme demand.

After the initial stage, the system reaches its efficient mode by operating in reverse: the four-way valves direct the high-pressure refrigerant leaving the compressor to the cabin *evaporator*, which, in this configuration function as a *condenser*, rejecting its latent heat into the passenger compartment. Then, the refrigerant passes through the expansion valve, which gives an isenthalpic expansion that drastically decrease its pressure and temperature. After that, the refrigerant passes through the *exchangers* that play the *role of evaporators*, such as the traditional *condenser* and the *water-cooled condenser (WCC)*. The WCC efficiently absorbs waste heat from the electric motor, which reduces the needs of the radiator fan that can remain off or operate at low speeds. This approach maximizes heat recovery and minimizes energy loss.

To maintain the battery within its optimal operating range during a cold start, a PTC heater may be used to quickly raise the battery temperature. However, once the initial warm-up is complete, thermal management is maintained through a connection with the chiller, which actively transfers heat to the battery's coolant during winter conditions.

This approach uses both the waste heat recovered from the powertrain and the heat pump's capacity, thereby increasing overall system efficiency.

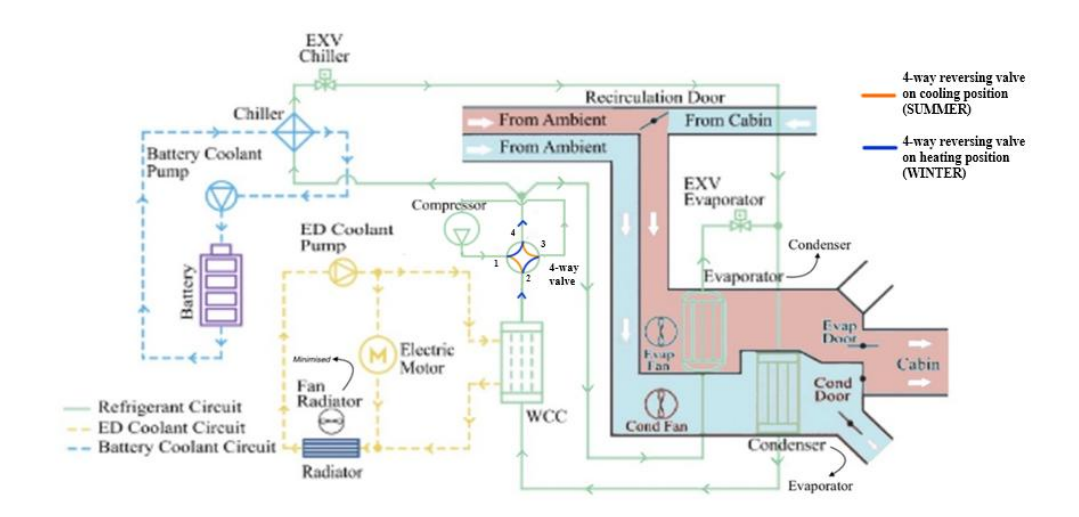


Figure 8 Thermal management system with heat pump in cold weather condition

In cold conditions, the heat pump system efficiently manages thermal needs by recovering waste heat from the powertrain and reducing reliance on high-consumption PTC heaters. This approach minimizes energy demand for heating, extends battery range by 10–25%, and helps overcome one of the key limitations of electric vehicles in winter operation.

The following chart reports findings from a Recurrent Auto study, showing the driving range in miles under different cabin heating conditions (no heat, heat pump, resistance heater) across different ambient temperatures, expressed in degrees Fahrenheit ($32^{\circ}F = 0^{\circ}C$, $14^{\circ}F = -10^{\circ}C$).

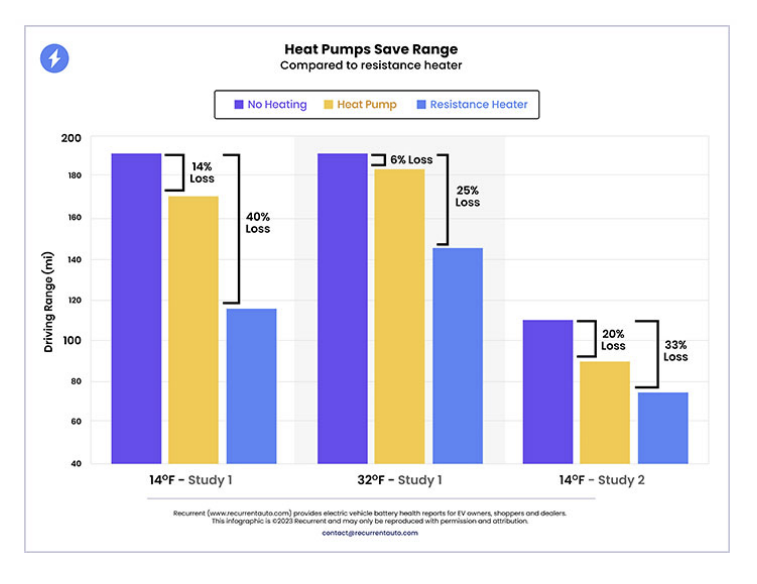


Figure 9 Driving range in cold ambient temperatures- comparison of heating methods (UFI Filter, 2023)

Lithium-ion batteries

Lithium-ion batteries are the predominant power source in battery electric vehicles (BEVs) due to their high energy density (up to 705 Wh/L) and exceptional power density (up to 10,000 W/L), which enable extended range and strong performance. However, their performance and safety are highly sensitive to temperature variations, with both low and high temperatures presenting significant challenges.

- At low temperatures, lithium-ion batteries suffer from increased electrolyte viscosity, leading to reduced ionic conductivity and elevated internal resistance. Charge-transfer resistance also rises significantly, impairing electrochemical kinetics, particularly during charging. Lithium-ion diffusion within electrodes slows down, further limiting performance. Additionally, low temperatures promote lithium plating on anodes, increasing the risk of dendrite formation and internal short circuits. These combined effects severely degrade battery capacity and safety under cold conditions. (Ma, et al., 2018)
- At high temperatures, lithium-ion batteries experience accelerated aging due to increased reaction kinetics, leading to degradation of electrodes, electrolyte decomposition, and structural damage. Heat generation from reversible and irreversible electrochemical processes raises internal temperatures further, intensifying these effects. Prolonged exposure also destabilizes the solid electrolyte interface (SEI) and promotes harmful phase transitions. Critically, excessive heat can trigger thermal runaway—an uncontrollable exothermic chain reaction—posing severe safety risks including fire or explosion. (Ma, et al., 2018)

The role of the BMS is crucial: through continuous monitoring and regulation of operational parameters, it helps mitigate thermal effects, optimize efficiency, and ensure the long-term safety of the battery system.

3. Physics-Based Modelling of Thermal Models

3.1 Methodological Approach

To accurately represent the thermal behaviour of an electric vehicle's key components under varying operating conditions, a physics-based modelling framework is implemented. This approach relies on fundamental thermodynamic principles and heat transfer equations, ensuring a high degree of Physical interpretability while maintaining computational efficiency suitable for system-level simulations and control-oriented applications.

A **dynamic battery model** is developed using Simulink, based on the structure presented in *Dynamic Lithium-Ion Battery Model* (Gao, Liu, & Dougal, 2002), in order to accurately reproduce the electro-thermal behaviour of the battery pack by accounting for the temperature dependence of electrical properties and heat generation during charge—discharge cycles.

For the **HVAC system**, the modelling follows the control-oriented approach proposed in *Control-oriented Model for Thermal Energy Management of Battery Electric Vehicles* (Lokur, Murgovski, & Larsson, 2024), which enables a simplified yet effective representation of energy flows across different operational modes.

As a reference, the Simscape Thermal Management Model provided by MathWorks (Electric Vehicle Thermal Management, s.d.) is used. This model is adapted to match the architecture and requirements of the studied system, ensuring full compatibility with the structure of the implemented physics models.

Furthermore, a series of **benchmark simulations** is conducted to test and validate each component of the HVAC cycle—such as the compressor, condenser, evaporator, and expansion valve. The results obtained from the developed physics-based models are compared against those of the Simscape reference model to ensure consistency and accuracy.

The overarching objective of this chapter is to develop a **simplified physics-based model** for simulating the dynamic behaviour of the refrigeration cycle in a Battery Electric Vehicle (BEV). The model draws inspiration from Lokur, Murgovski, & Larsson (2024), who proposed a control-oriented framework capable of capturing EV thermal dynamics efficiently.

The modelled system is constructed based on the following simplifying assumptions:

1. **Cooling Configuration**: The battery is air-cooled, while the powertrain group (e-motor and power electronics) is liquid-cooled.

- 2. **Radiator Dynamics**: The dynamics of the temperature difference (ΔT) across the radiator are considered negligible; the radiator is modelled assuming steady-state conditions.
- 3. **Battery Electrical Properties**: The battery's internal resistance is a function of its temperature; this dependency is explicitly considered in predicting the system's electrical behaviour.
- 4. **Flow Control**: An additional control variable, representing a deviation from the nominal speed profile, is associated with the cooling circuit pump flow rate.
- 5. **Passenger Cabin Thermal Model**: A lumped-parameter thermal model is used for the vehicle cabin under the following hypotheses:
 - The internal thermal mass is represented as a single entity with average thermal properties.
 - All internal components are assumed to be at the same temperature.
 - Internal surfaces possess uniform thermal properties and are therefore modelled with a single representative temperature.
- 6. **Refrigerant Circuit**: The refrigerant circuit is implemented in detail, with particular focus on the modelling of its fundamental components: the compressor, condenser, electronic expansion valve (EEXV), and evaporator.

3.2 Vehicle & Powertrain Thermal Interactions

Vehicle Dynamics and Powertrain Model

The prediction model of the vehicle dynamics calculates the total power required to follow a given speed profile. This is based on a force balance and considers different resistive and inertial components acting on the vehicle.

The reference speed is modified to allow a deviation from the nominal speed trajectory:

$$v_{\text{ref}_mod} = v_{\text{ref}} + delta_v_{\text{ref}}$$

The total traction power demand is composed of multiple contributions:

$$P_{\text{req}} = P_{\text{roll}} + P_{\text{aerodrag}} + P_{\alpha} + P_{\text{ax}} + P_{\text{sx}} + P_{\text{sy}}$$

• Rolling resistance power: $P_{\text{roll}} = \left(f_0 + f_1 \cdot v_{\text{ref_mod}} + f_2 \cdot v_{\text{ref_mod}}^2\right) \cdot m \cdot g \cdot v_{\text{ref_mod}}$

Where f_0, f_1, f_2 : rolling resistance coefficients, m: vehicle mass, g: gravitational acceleration

- Aerodynamic drag power: $P_{\text{aerodrag}} = 0.5 \cdot \rho_{\text{air}} \cdot S \cdot C_{\text{drag}} \cdot v_{\text{ref_mod}}^3$ Where ρ_{air} : air density, S: frontal area of the vehicle, C_{drag} : aerodynamic drag coefficient
- Power associated with the road gradient: $P_{\alpha}=m\cdot g\cdot\sin(\alpha_{\rm ref})\cdot v_{\rm ref_mod}$ Where $\alpha_{\rm ref}$: road slope angle
- Power associated with vehicle acceleration: $P_{\rm ax}=m\cdot a_x\cdot v_{\rm ref_mod}$ Where a_x : longitudinal acceleration
- Longitudinal tyres slip power loss: $P_{\text{s}x} = \left(\frac{P_{\text{req}}}{v_{\text{ref_mod}}}\right) \cdot v_{\text{s}x} = \left(\frac{P_{\text{req}}}{v_{\text{ref_mod}}}\right) \cdot \left[\frac{\left(\frac{P_{\text{req}}}{v_{\text{ref_mod}}}\right)}{C_{\text{long_slip_eq}}} \cdot v_{\text{ref_mod}}\right]$ Where $C_{\text{long_slip_eq}}$: longitudinal slip equivalent coefficient
- Lateral tyres slip power loss: $P_{sy} = C_f \cdot \alpha_f^2 \cdot v_{\text{ref_mod}} + C_r \cdot \alpha_r^2 \cdot v_{\text{ref_mod}}$ Where C_f , C_r : cornering stiffness of front and rear tires, α_f , α_r : front and rear tire slip angles, which are calculated as follows:

$$a_y = v_{\text{ref}_mod}^2 \cdot \rho_{\text{ref}}$$
 $F_{y_f} = m \cdot a_y \cdot \frac{b}{L} \qquad F_{y_r} = m \cdot a_y \cdot \frac{a}{L}$
 $\alpha_f = \frac{F_{y_f}}{C_f} \qquad \qquad \alpha_r = \frac{F_{y_r}}{C_r}$

Where a_y : lateral acceleration, L: wheelbase length, a,b: distances from the center of gravity to rear and front axles

Electric Motor and Drivetrain Loss Modelling

The electric motor provides the mechanical power required to drive the wheels, denoted as P_{req} . However, not all the electric power from the battery is converted into mechanical output due to drivetrain and motor losses.

To represent the smooth transition between motor traction and regenerative braking modes, a sigmoid-based expression is used (Dalboni, et al., 2021):

$$P_{\text{driv}} = P_{\text{em,min}} + \frac{P_{\text{req}} - P_{\text{em,min}}}{1 + e^{-w_{\text{ss}}(P_{\text{req}} - P_{\text{em,min}})}}$$

- P_{driv} : Smoothened driveline power
- P_{req}: Required driving power (previous section)
- $P_{\rm em,min}$: Minimum allowable electric motor power (for regen braking)
- $w_{\rm ss}>0$: Sigmoid slope coefficient defines the degree of smoothness between traction and braking regimes.

The friction brake power is described with the difference: $P_{\text{req}} - P_{\text{em,min}}$.

The total mechanical power the electric motor must provide includes drivetrain losses:

$$P_{\text{mech,em}} = P_{\text{driv}} + P_{\text{loss,drivetrain}}$$

The torque required from the electric motor is calculated as:

$$T_{\rm em} = \frac{R_w \cdot P_{\rm mech,em}}{v_{\rm ref\ mod}}$$

Where R_w : Effective wheel radius and $v_{\rm ref\ mod}$: reference vehicle speed

The power losses are modelled using a 2D polynomial as a function of motor torque and speed (Dalboni, et al., 2021):

$$P_{\text{loss,drivetrain}} = \sum_{m=0}^{5} \left(\sum_{n=0}^{5} p_{\text{dr,m,n}} T_{\text{em}}^{n} \right) \left(\frac{\tau v_{\text{ref_mod}}}{R_{w}} \right)^{m}$$

$$P_{\text{loss,powertrain}} = \sum_{m=0}^{5} \left(\sum_{n=0}^{5} p_{\text{em,m,n}} T_{\text{em}}^{n} \right) \left(\frac{\tau v_{\text{ref_mod}}}{R_{w}} \right)^{m}$$

The coefficients of the previous polynomial expressions ($p_{dr,m,n}$, $p_{em,m,n}$) vary as a function of the powertrain temperature, τ : gear ratio

The total power drawn from the battery is:

$$P_{\text{batt}} = P_{\text{mech,em}} + P_{\text{loss,powertrain}} + P_{aux}$$

Where P_{aux} : auxiliary systems power demand (e.g., lighting, electronics)

The motor's temperature is modelled using the energy balance:

$$C_{\text{mot}} \frac{dT_{\text{em}}}{dt} = P_{\text{loss,powertrain}} + K_1(T_{\text{amb}} - T_{\text{em}}) - Q_{\text{coolant}}$$

Where C_{mot} is the thermal capacity of the motor, T_{em} is the motor's temperature, T_{amb} is the ambient temperature and K_1 is the heat transfer coefficient

$$Q_{\text{coolant}} = c_{\text{coolant}} \cdot \dot{m}_{coolant} \cdot \Delta T$$

 $\mathsf{C}_{\mathsf{coolant}}$ is the specific heat capacity of the coolant, and $\dot{m_{\mathsf{coolant}}}$ is the coolant mass flow rate.

 ΔT is the temperature difference between the inlet and outlet of a body cooled, considered constant.

$$P_{\text{cooling pump}} = \sum_{n=0}^{N} c_n \cdot (\dot{m}_{coolant})^n$$

Where c_n are the coefficients for each polynomial terms.

3.3 Cabin thermal model

Assuming that passenger thermal comfort is achieved when the cabin air temperature reaches a reference value, this section aims to define the relationship between the cabin air temperature (Tca) and the heat exchanged among the passengers, the environment, and the interior surfaces. (Lokur, Murgovski, & Larsson, 2024)

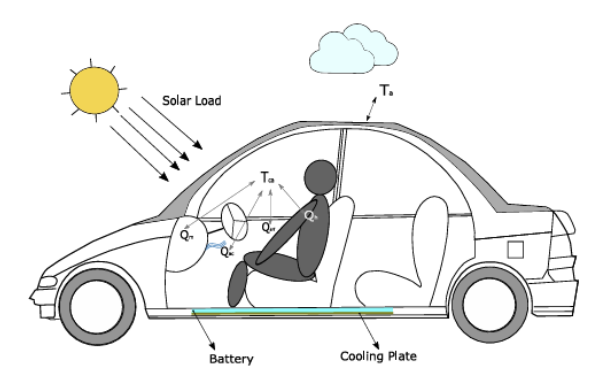


Figure 10 Cabin setup (Lokur, Murgovski, & Larsson, 2024)

The cabin air temperature dynamics are computed as follow:

$$\frac{dT_{ca}(t)}{dt} = \frac{Q_h + Q_{srf} + Q_m - Q_{ac}}{\alpha_1 \rho_a c_{na} V_c}$$

Where T_{ca} : cabin air temperature, α_1 : fitted coefficient, ρ_a : air density, c_{pa} : specific heat capacity of air, V_c : cabin volume

Heat contributions:

• Q_h : heat rejection by the passengers:

$$Q_h = \sum_{i=0}^n a_i T_{ca}^i$$

Where a_i : coefficients characterizing heat output dependent on cabin air temperature.

Q_{srf}: heat from the interior surfaces:

$$Q_{srf}(T_{ca}, T_{srf}) = h_{srf} A_{srf} \left(T_{ca}(t) - T_{srf}(t) \right)$$

Where h_{srf} : heat transfer coefficient between cabin air and interior surfaces, A_{srf} heat transfer area, T_{srf} : interior surface temperature

• Q_m : heat transfer from interior parts:

$$Q_m(T_{ca}, T_m) = h_m A_m (T_{ca}(t) - T_m(t))$$

Where h_m : heat transfer coefficient, A_m : effective heat transfer area, T_m : temperature of interior mass components

Q_{ac}: the refrigeration capacity of the air conditioning system

$$Q_{ac} = W_{ev,a}(t) \cdot c_{pa} \cdot \left(T_{ev,ain}(T_{ca}) - T_{ev,aout}\right)$$

Where $W_{ev,a}$: mass flow rate of air through the evaporator, $T_{ev,ain}$: inlet air temperature to the evaporator, a mix of cabin and ambient air, $T_{ev,aout}$: outlet air temperature from the evaporator

The air entering the evaporator is a combination of cabin air and ambient air (Figure 5). Consequently, the inlet temperature $T_{ev,ain}$ depends on the recirculation door position $G_{re} \in [0,1]$:

$$T_{ev\,ain}(T_{ca}) = G_{re}T_{ca}(t) + (1 - G_{re})T_{a}$$

The rate of change in interior surface temperature is expressed as:

$$\frac{dT_{\rm srf}(t)}{dt} = \frac{-Q_{\rm srf} + (T_{\rm esrf} - T_{\rm srf}(t))/R_T}{\alpha_2 m_{\rm srf} c_{p_{\rm crf}}}$$

Where $m_{\rm srf}$: mass of the interior surfaces, $c_{p_{\rm srf}}$: specific heat capacity of the interior surface, $T_{\rm esrf}$: exterior surface temperature, R_T : thermal resistance between the interior and exterior surface of the cabin, α_2 : fitted coefficient.

The rate of change of the interior mass temperature is expressed as:

$$\frac{dT_m(t)}{dt} = \frac{1}{\alpha_3 m_m c_{p_m}} (Q_m + \tau_{\text{win}} A_{\text{win}} G_{\text{sol}})$$

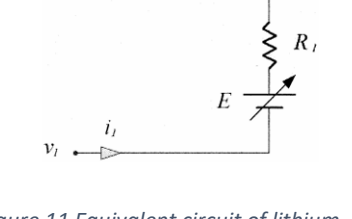
Where m_m : interior mass of the car, including seats, dashboard, steering wheel and floor carpet; c_{p_m} : specific heat capacity of interior mass, τ_{win} : transmittance factor of windows, A_{win} : heat transfer area of the windows, G_{sol} : solar radiation power density, α_3 : fitted coefficient.

3.4 Lithium-Ion Battery Model

The model aims to replicate both the electrical and thermal behaviour of the battery by incorporating nonlinear equilibrium potentials, as well as rate- and temperature-dependent effects. It simplifies the system by assuming uniform electrochemical and thermal processes throughout the battery, neglecting spatial variations in concentration, phase distribution, and potential. (Gao, Liu, & Dougal, 2002).

The battery can be schematized using an equivalent circuit model composed of the following elements:

- Equilibrium potential (E): Represents the open-circuit voltage.
- Internal resistance: Modelled with two components:
 - Ohmic resistance (R1): Accounts for ionic and electronic conduction losses.
 - o *Polarization resistance (R2)*: Captures kinetic and concentration overpotentials.



• Effective capacitance (C): Represents the transient response due to charge accumulation in the double layers at the electrode—electrolyte interface, typical of porous electrodes.

Figure 11 Equivalent circuit of lithiumion battery (Gao, Liu, & Dougal, 2002)

Electrical Battery Model

Considering the electrical battery model, the equilibrium potential is modelled using a four-step procedure:

1. To accurately model the *equilibrium potential*, a reference voltage curve is selected from a typical discharge cycle and fitted with an n-th order polynomial, representing the open-circuit voltage as a function of SOD, while excluding internal losses. The *open-circuit voltage* of a lithium-ion battery depends on its *temperature* and *state of*

discharge (SOD), while the discharge capacity varies with both the discharge rate and temperature.

The model defines the equilibrium potential E[i(t), T(t), t] as:

$$E[i(t), T(t), t] = v[i(t), T(t), t] - R_{int}i(t)$$

where v[i(t), T(t), t] is the measured terminal voltage, and R_{int} is the internal resistance. The voltage function is expressed as:

$$v[i(t), T(t), t] = \sum_{k=0}^{n} c_k SOD^k[i(t), T(t), t] + \Delta E(T)$$

 c_k are the polynomial coefficients, and $\Delta E(T)$ is a temperature correction term. The state of discharge itself is computed dynamically as:

$$SOD[i(t), T(t), t] = \frac{1}{Q_r} \int_0^t \propto [i(t)] \cdot \beta[T(t)] \cdot i(t) dt$$

where Q_r is the reference capacity, and $\propto [i(t)]$ and $\beta[T(t)]$ are the current and temperature correction factors, respectively.

To model the open-circuit voltage as a function of the state of discharge (SOD), a reference discharge curve is selected at a known discharge current (in this case, 0.7 A). Starting from the experimental data represented with squared marks in the following chart (Figure 12), the battery voltage is fitted using a polynomial function. The coefficients c_k are obtained through this polynomial fitting process.

2. a *rate factor* is introduced to account for how different discharge currents affect the capacity, normalized to one at the reference rate.

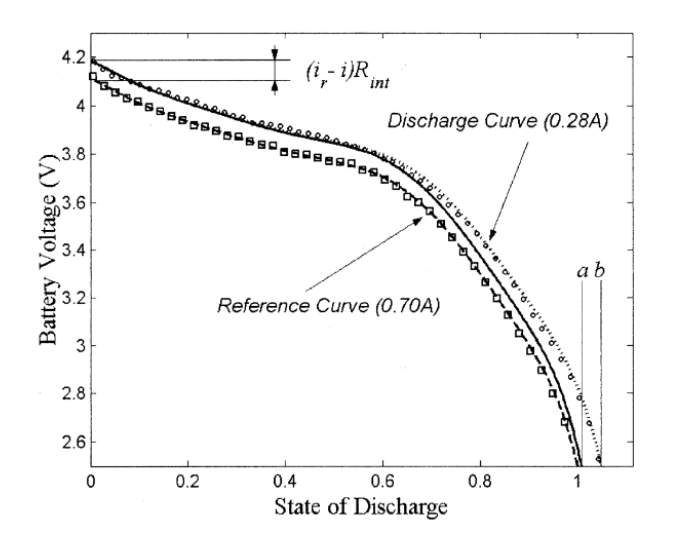


Figure 12 Rate factor (Gao, Liu, & Dougal, 2002)

With respect to the previously defined reference curve, a new experimental discharge curve is introduced, acquired at a lower discharge current (0.28 A). This curve, represented by circles in Figure 12, displays a higher discharge capacity, denoted as *b*, due to reduced internal losses at lower current.

To accurately capture the rate-dependent behaviour, the internal losses (R_{int} (i_r-i)) are also subtracted from the reference curve. This process yields a corrected version of the reference discharge profile (solid line) with a lower effective capacity, denoted as a. This correction allows for a direct comparison of usable capacities under different current conditions and enables the calculation of the **rate factor** \propto (i) = $\frac{a}{b}$, which is used in the state-of-discharge computation.

3. a *temperature factor* captures the influence of temperature variations on discharge behaviour, also set to one at the reference temperature.

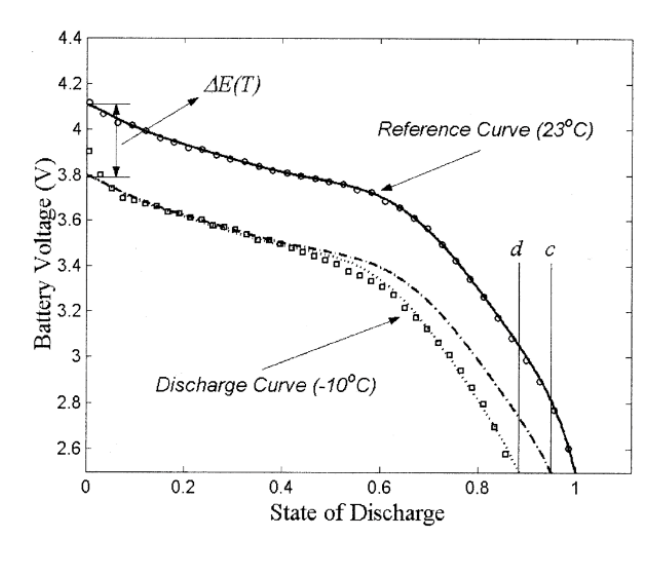


Figure 13 Temperature factor and temperature-dependent potential-correction term

(Gao, Liu, & Dougal, 2002)

The temperature factor is determined by analysing discharge curves at a constant reference current of 0.7 A but at different constant temperatures. The reference temperature is set at 23°C, represented by circles, and normalized to have a unit discharge capacity. A second discharge curve, corresponding to a lower temperature of -10°C and depicted with squares, exhibits a reduced discharge capacity, denoted as *d*.

To account for temperature effects, the reference curve is shifted to best fit the flat portion of the low-temperature discharge curve. To quantify this effect, the reference curve is shifted to best fit the flat portion of the low-temperature discharge curve,

resulting in an adjusted discharge capacity c. The *temperature factor* β is then calculated as the ratio between these capacities: $\beta(T) = \frac{c}{d}$

4. a *potential correction term* adjusts the equilibrium potential for temperature-induced changes, ensuring accuracy across varying operating conditions.

This term is derived from the shifted reference curve, which best fits the flat portion of the low-temperature discharge curve, ensuring that the model accurately captures the effect of temperature on the battery's equilibrium potential across different operating conditions.

The Simulink model developed to replicate the equilibrium potential behaviour of the battery is based on the previously described set of equations. It implements the dynamic relationships among current, temperature, and state of discharge to compute the open-circuit voltage under varying conditions.

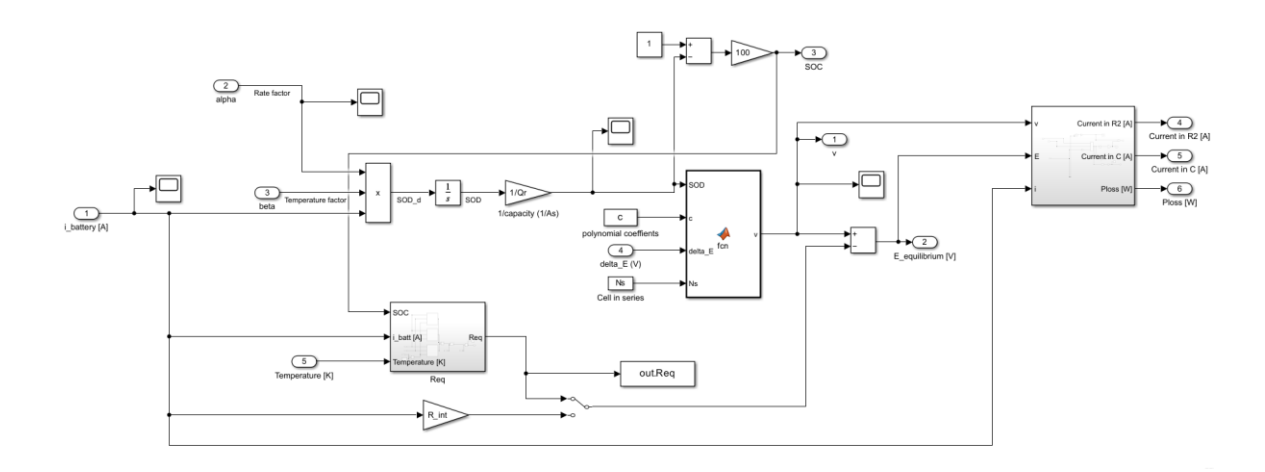


Figure 14 Electrical battery model

To capture the *battery's transient behaviour* under dynamic loading conditions, capacitive effects must be considered. These arise primarily from double-layer formation at the electrode/solution interface and capacitance from diffusion processes (also known as pseudo-capacitance). These phenomena become particularly relevant when the rate of electrochemical reactions increases, as in high-power applications or hybrid configurations with supercapacitors. In the proposed model, these effects are represented by a single lumped capacitance placed in parallel with one branch of the internal resistance, denoted as R₂.

By combining the electrochemical characteristics of the battery with the equivalent-circuit representation, the terminal voltage and current are related by:

$$i(t) = \frac{1}{R_2} \left[v(t) - E[i(t), T(t), t] - R_1 i(t) \right] + C \frac{d}{dt} \left[v(t) - E[i(t), T(t), t] - R_1 i(t) \right]$$

This formulation enables the decomposition of the total current into two parallel components: one flowing through the resistor R_2 and the other through the capacitor \mathcal{C}

$$i(t) = i_{R_2}(t) + i_C(t)$$

$$i_{R_2}(t) = \frac{1}{R_2} [v(t) - E[i(t), T(t), t] - R_1 i(t)]$$

$$i_C(t) = C \frac{d}{dt} [v(t) - E[i(t), T(t), t] - R_1 i(t)]$$

In addition, the total power loss in the battery is computed as:

$$P_{loss}(t) = i^{2}(t)R_{1} + \frac{1}{R_{2}}[v(t) - E[i(t), T(t), t] - R_{1}i(t)]^{2}$$

accounting for the ohmic dissipation in both R_1 and R_2 .

The transient behaviour of the battery, including the effects of the parallel resistance R₂ and the lumped capacitance, is implemented in Simulink as shown in the Figure 15Figure 15.

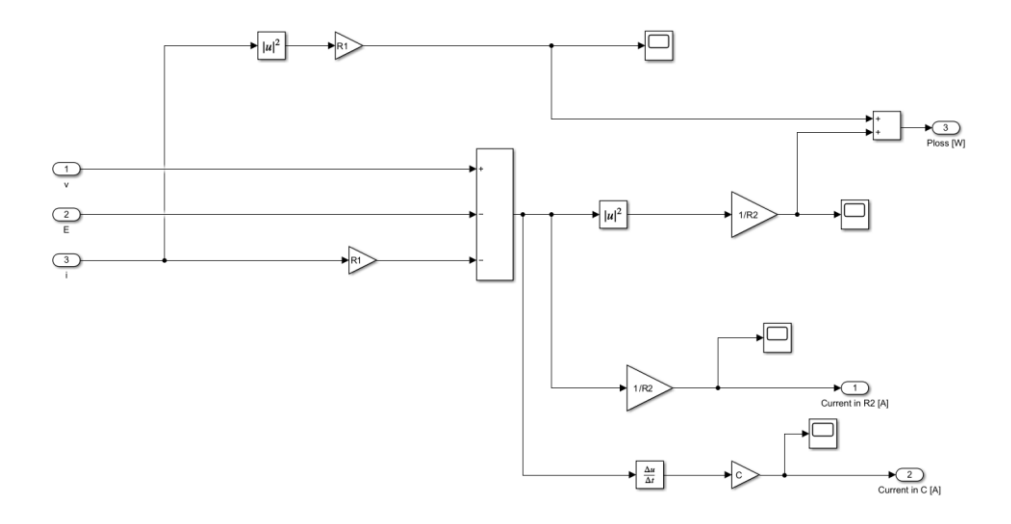


Figure 15 Transient response of the battery

Thermal Battery Model

To accurately compute the temperature-dependent equilibrium potential at each simulation step, the battery temperature is dynamically calculated through a thermal energy balance. This model primarily accounts for heat generated by internal resistive losses and heat exchanged with the surrounding environment.

$$m \cdot c_p \cdot \frac{dT(t)}{dt} = i(t)^2 \cdot R_1 + \frac{1}{R_2} [v(t) - E[i(t), T(t), t] - R_1 i(t)]^2 - h_c A[T(t) - T_a]$$

The thermal model is implemented in Simulink as follows:

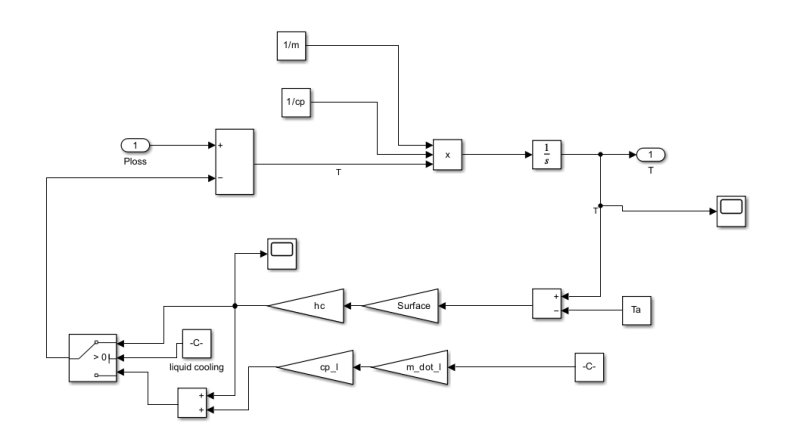


Figure 16 Thermal battery model

Battery Model

The comprehensive battery model integrates both the electrical and thermal sub-models within a Simulink environment. This combined approach enables simultaneous simulation of the battery's voltage response and temperature dynamics under varying load conditions.

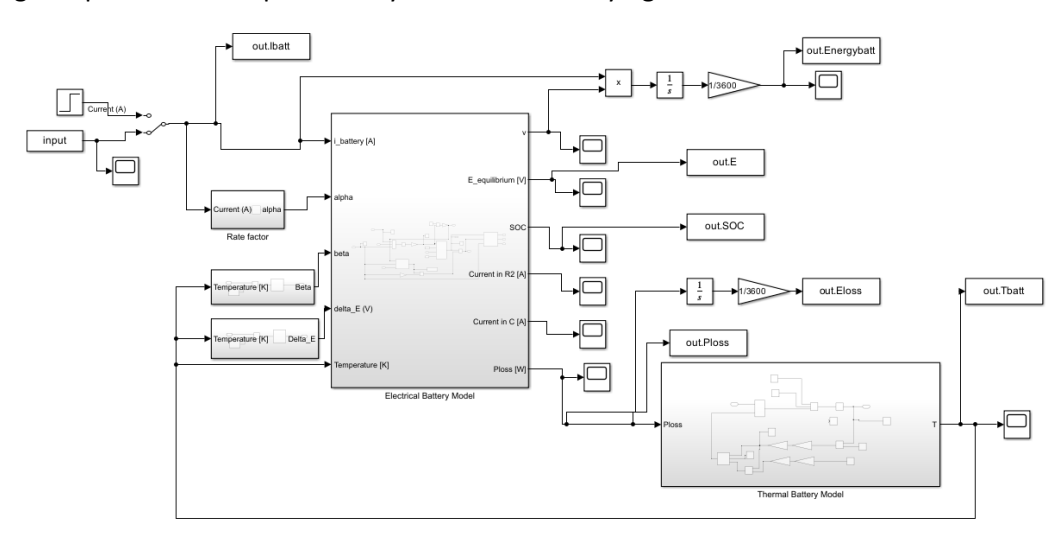


Figure 17 Battery model

The simulations are performed using discharge current as input, which is obtained from experimental data recorded during a WLTP test at 85°C, with a cooling flow rate of 12 liters per minute (12 lpm) and a DC voltage of 700 V.

In <u>Case 1</u>, with an ambient temperature of 23 °C and an initial battery temperature of 20 °C, the State of Charge (SOC) starts at 100% and gradually decreases to about 94% after 1800 seconds.

The battery temperature slightly rises from 293 K (20 °C) to nearly 296 K (23 °C) during the test. The internal resistance remains low and stable, oscillating between 4.5 and 5.5 \times 10^-4 Ohm, allowing for moderate power losses with occasional peaks reaching up to 6000 W.

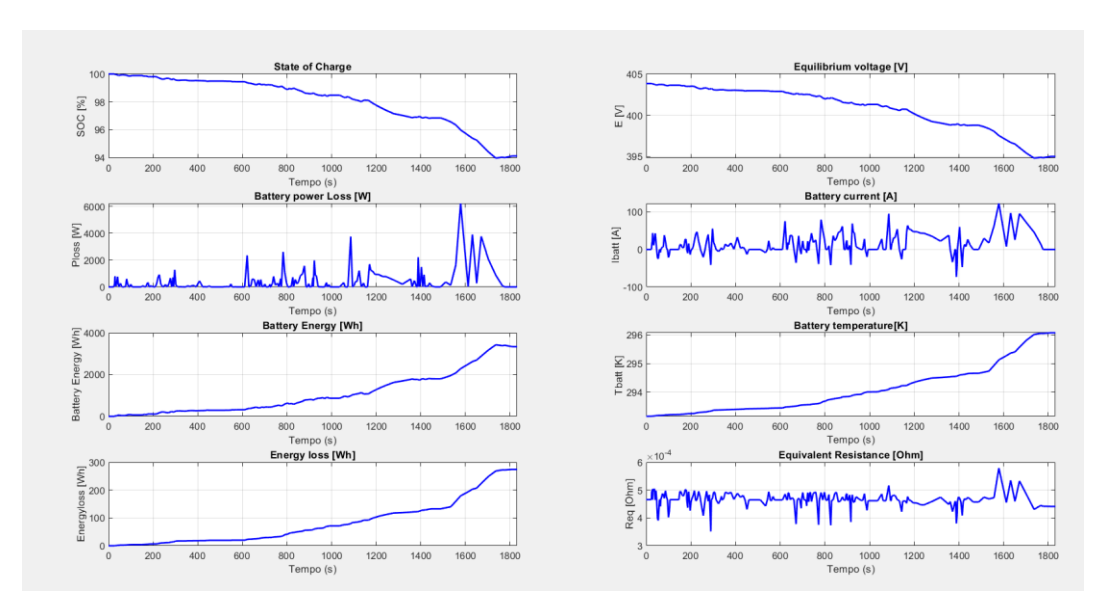


Figure 18 Battery simulation: Tamb = 23°C; Tbatt = 20°C

In <u>Case 2</u>, where the ambient temperature is still 23 °C but the battery starts cold at 0 °C, the SOC decreases more slowly, reaching about 96.5% after 1447 seconds. However, the internal resistance is significantly higher, varying between 0.5 and 2 x10⁻³ Ohm, almost four times greater than in Case 1. The resistance starts high but gradually drops as the battery temperature rises. This higher resistance causes greater variability in power losses and a reduced overall efficiency. The battery temperature increases slowly from 273 K (0 °C) to around 278 K (5 °C). The initial large temperature difference between the battery and the ambient environment causes increased energy dissipation due to the low starting temperature.

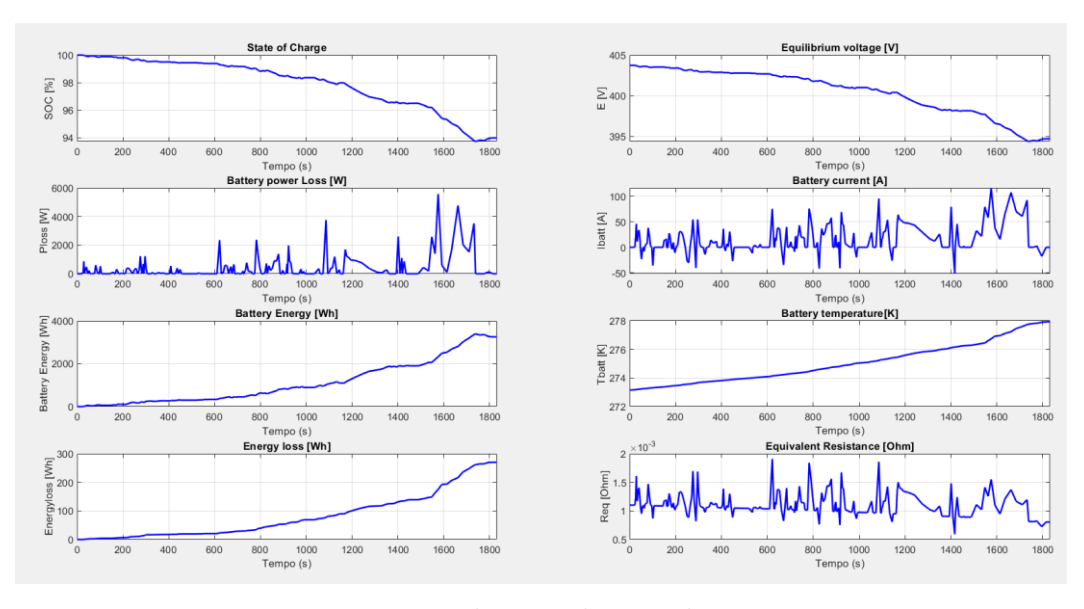


Figure 19 Battery simulation: Tamb = 23°C; Tbatt = 0°C

In <u>Case 3</u>, with an ambient temperature of 0 °C and battery temperature at 20 °C, the SOC behaves similarly to Case 1, decreasing to about 94% after 1800 seconds. The internal resistance remains low and stable around 4.5-5 x10^-4 Ohm, with contained and regular power losses. The battery temperature stays nearly constant around 293 K (20 °C) throughout the test but shows oscillatory behaviour between 292.5 K and 294 K. This non-monotonic trend is influenced by the interaction between thermal dispersion to the colder environment and internal heating from energy losses. Initially, the battery cools due to the colder ambient temperature, then slightly warms toward the end of the cycle.

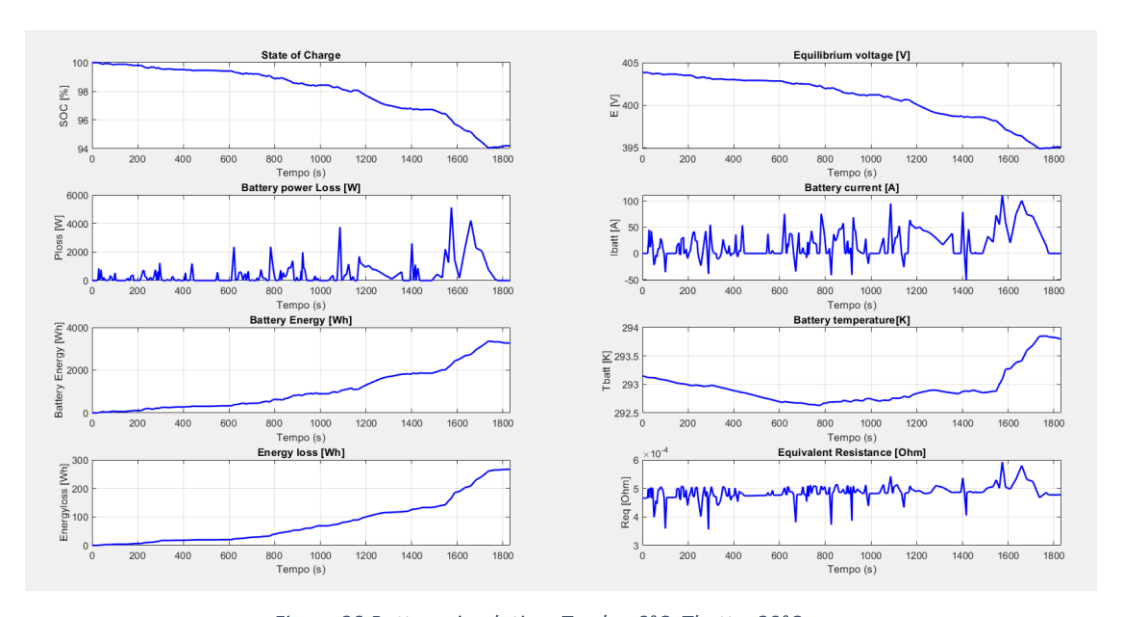


Figure 20 Battery simulation: Tamb = 0°C; Tbatt = 20°C

3.5 Refrigerant circuit

In a closed-loop refrigerant cycle operating under steady-state conditions, the principle of mass conservation applies. This means that the mass flow rate of the refrigerant remains constant throughout the entire system :

$$\dot{m}_{\text{comp}} = \dot{m}_{\text{cond}} = \dot{m}_{\text{exp}} = \dot{m}_{\text{evap}} = \dot{m}$$

The dynamic behaviour of the refrigeration system is described using a set of differential equations based on thermodynamic principles, including mass and energy conservation, and empirical relations derived from system identification and manufacturer data.

Under steady-state conditions, the pressure at the compressor inlet depends on the pressure drop at the expansion valves (stationary conditions), therefore its rate of change is:

$$\frac{dp_{c_{in}}(t)}{dt} = \alpha_{pc_{in}} p_{c_{in}}(t) + \beta_{Pc_{in}} \Delta p_{\text{exv}}(t)$$

Where $lpha_{pc_{in}}$, $eta_{Pc_{in}}$:fitted coefficients, $\Delta p_{ ext{exv}}$:pressure drop across the expansion valves.

The refrigerant temperature at the inlet of the compressor depends on the energy conservation along the cycle:

$$\frac{dT_{c_{in}}(t)}{dt} = \alpha_{Tc_{in}} T_{c_{in}}(t) + \frac{\beta_{Tc_{in}}}{\dot{m}_{compressor}(t)c_{p_{rh}}} \left(\dot{Q}_{ev} - \dot{Q}_{cond}\right)$$

Where $\alpha_{Tc_{in}}$, $\beta_{Tc_{in}}$: fitted coefficients, \dot{Q}_{ev} , \dot{Q}_{cond} : heat transfer rates from the evaporator and to the condenser, $c_{p_{rh}}$: specific heat capacity of the refrigerant at constant pressure.

The rate of heat transfer, both in the evaporator and in the condenser, are modulated using the number of transfer units (NTU) method:

• The heat rate from the evaporator:

$$\dot{Q}_{\rm ev} = (1 - \exp(-k_{ev})) \alpha_{ev} C_{\rm ev,min}(t) (T_{\rm ev,rin} - T_{\rm ev,ain})$$

The NTU describes heat transfer across a surface, and it's denoted as

$$k_{ev} = \frac{U_{ev} A_{ev}}{C_{ev,min}(t)}$$

 U_{ev} is the heat transfer coefficient, A_{ev} the transfer area, $T_{\rm ev,rin}$ is the refrigerant temperature at the inlet of the evaporator and $T_{ev,ain}$ is the air temperature and α_{ev} is a fitted coefficient (characteristic of the evaporator and operating conditions)

To determine the maximum possible heat transfer rate in the heat exchanger, the minimum heat capacity rate must be used:

$$C_{\text{ev},min}(t) = min[\dot{m}_{ev,a} c_{p_a}; \dot{m}_{ev,r} c_{p_r};]$$

 $\dot{m}_{ev,a}$ is the air mass flow rate at the evaporator fan (control action), c_{p_a} is the specific air heat transfer; $\dot{m}_{ev,r}$ is the refrigerant mass flow rate in the evaporator (control action), c_{p_r} is the specific heat transfer of refrigerant

Since the limiting heat capacity rate is typically determined by the air that imposes the main restriction on heat transfer, the expression can be simplified as follow:

$$C_{\text{ev.}min}(t) = \dot{m}_{ev.a} c_{p_a}$$

The heat rate from the condenser:

$$\dot{Q}_{co} = (1 - \exp(-k_{co})) \alpha_{co} C_{co,min}(t) (T_{co,rin} - T_{co,ain})$$

The NTU describes heat transfer across a surface, and it's denoted as

$$k_{co} = \frac{U_{co} A_{co}}{C_{co,min}(t)}$$

 U_{co} is the heat transfer coefficient, A_{co} the transfer area, $T_{\rm co,rin}$ is the refrigerant temperature at the inlet of the condenser and $T_{co,ain}$ is the air temperature and $T_{co,ain}$ is the air temperature and $T_{co,ain}$ is a fitted coefficient (characteristic of the condenser and operating conditions)

To determine the maximum possible heat transfer rate in the heat exchanger, the minimum heat capacity rate must be used:

$$C_{co,min}(t) = min[\dot{m}_{co,a} c_{p_a}; \dot{m}_{co,r} c_{p_r}]$$

 $\dot{m}_{xo,a}$ is the air mass flow rate at the condenser fan (control action), c_{p_a} is the specific air heat transfer; $\dot{m}_{ev,r}$ is the refrigerant mass flow rate in the condenser (control action), c_{p_r} is the specific heat transfer of refrigerant

Since the limiting heat capacity rate is typically determined by the air that imposes the main restriction on heat transfer, the expression can be simplified as follow:

$$C_{co,min}(t) = \dot{m}_{co,a} c_{p_a}$$

The electric power consumed by the compressor is expressed as a polynomial function of the refrigerant mass flow rate and pressure differential, based on manufacturer data:

$$P_c(\dot{m}_{compressor}, \Delta p_c) = \sum_{i=0}^{2} \sum_{j=0}^{3} \sigma_{ij} \dot{m}_{compressor}^{i}(t) \Delta p_c^{j}(t)$$

 σ_{ij} are fitted coefficients (manufacturing data)

Thermodynamic states

The interconnecting tubes between the refrigeration system components are assumed to be well-insulated, minimizing both heat losses and pressure drops. The following relations describe the thermodynamic states at various key points of the cycle:

Compressor outlet:

$$T_{c_{\text{out}}}(t) = T_{c_{\text{in}}}(t) + \sum_{i=0}^{4} \sum_{j=0}^{3} \kappa_{ij} \dot{m}_{compressor}^{i}(t) \Delta p_{c}^{j}(t)$$

Where κ_{ij} are fitted coefficients for manufactures data.

$$p_{c_{\text{out}}}(t) = p_{c_{\text{in}}}(t) + \iota \Delta p_{\text{exv}}(t)$$

where ι is the correction factor for pressure drop in the tube.

Condenser input:

Since the tube is insulated and short, thermodynamic properties are assumed unchanged between compressor outlet and condenser inlet:

$$T_{co_{in}}(t) = T_{c_{out}}(t)$$

$$p_{co_{in}}(t) = p_{c_{out}}(t)$$

Condenser output:

The condensation process is assumed to be isobaric (constant pressure):

$$p_{co_{out}}(t) = p_{co_{in}}(t)$$

The outlet temperature is decreased based on the condenser heat rejection rate:

$$T_{co_{out}}(t) = T_{co_{in}}(t) - \frac{\alpha_{Tco_{out}}}{\dot{m}_{compressor}(t)c_{p_{rh}}} \dot{Q}_{co}$$

Where $\alpha_{Tco_{out}}$ is a fitted coefficient

Expansion valve input:

$$T_{ex_{in}}(t) = T_{co_{out}}(t)$$

$$p_{ex_{in}}(t) = p_{co_{out}}(t)$$

Expansion valve output:

The expansion process is considered **adiabatic** and **isenthalpic**, meaning the enthalpy of the refrigerant remains constant:

$$p_{ex_{out}}(t) = p_{c_{out}}(t) - \Delta p_{\text{exv}}$$

The pressure drop in the expansion valve Δp_{exv} is a control action.

The refrigerant temperature after expansion is calculated from its enthalpy and pressure:

$$T_{ex_{out}}(\cdot) = T_{\mathsf{sat,lp}}(p_{ex_{out}}) - \frac{H_{\mathsf{lp}}(\cdot) - H_{\mathsf{sat,lp}}(p_{ex_{out}})}{c_{\mathsf{pr,lp}}}$$

where $T_{\rm sat,lp}$ and $H_{\rm sat,lp}$ are saturation temperature and saturation enthalpy of the refrigerant at low pressure, respectively, $c_{\rm pr,lp}$ is the specific heat capacity of the refrigerant at low pressure, $p_{ex_{out}}$ is the outlet refrigerant pressure at the expansion valve and $H_{\rm lp}$ is refrigerant enthalpy at the EEXV exit.

The enthalpy H_{lp} is calculated based on high-pressure conditions before expansion:

$$H_{\mathsf{lp}}(\cdot) = H_{\mathsf{sat},\mathsf{hp}}(p_{ex_{in}}) + c_{\mathsf{pr},\mathsf{lp}}(T_{ex_{in}}(t) - T_{\mathsf{sat},\mathsf{hp}}(p_{\mathsf{cout}}))$$

where $H_{\rm sat,hp}$ is saturation enthalpy and $T_{\rm sat,hp}$ is saturation temperature of the refrigerant at high pressure.

Evaporator input:

$$p_{ev,r_{in}} = p_{ex_{out}}$$

$$T_{ev,r_{in}} = T_{ex_{out}}$$

Evaporator output:

$$p_{ev,r_{out}} = p_{c_{in}}(t)$$

$$T_{ev,r_{out}} = T_{c_{in}}(t)$$

Simulink model

Based on the analytical framework established in the preceding section, a numerical model has been implemented within the Simulink environment to simulate the dynamic behaviour of a thermodynamic refrigeration cycle. The primary objective of this model is to compute the key thermodynamic states of the refrigerant, specifically its temperature and pressure, at each defined point throughout the system. This computational approach facilitates a realistic representation of the cycle's performance under a diverse set of operational conditions.

The model's core inputs are the refrigerant mass flow rate, which governs the working fluid in circulation; the air mass flow rate across the evaporator, which determines its heat absorption capacity; and the pressure drop between the evaporator and compressor, which defines the compressor's inlet conditions and the low-pressure side of the cycle.

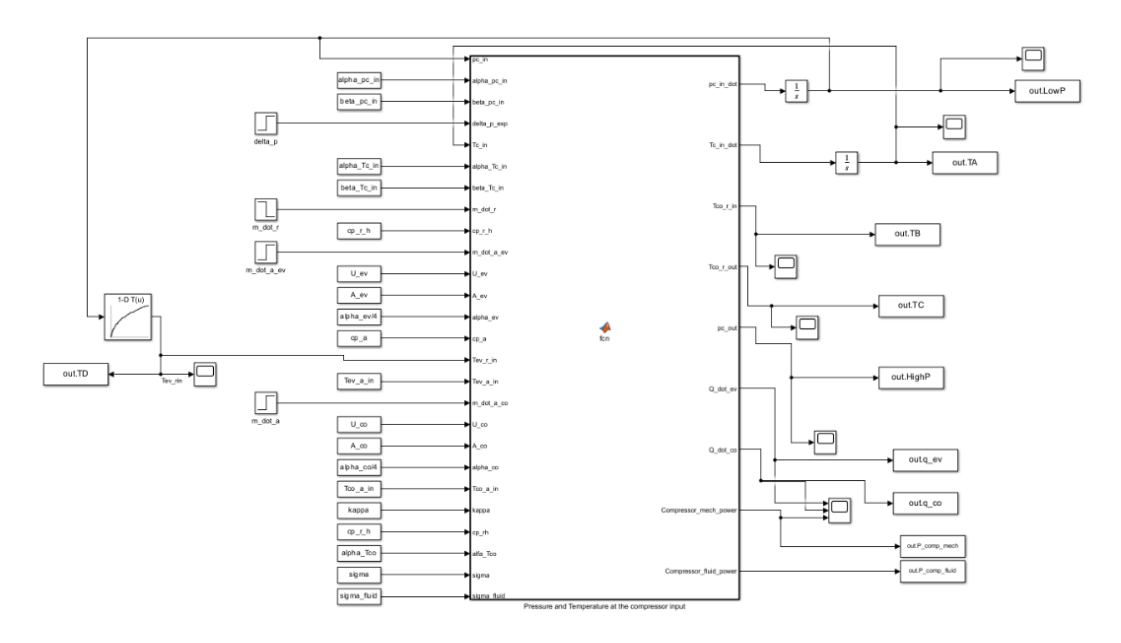


Figure 21 Refrigerant circuit model

The simulation time is reported in the graph below, showing that it takes approximately 0.7 seconds to run the model.

To ensure a fair comparison between the Simscape model, the simplified Simulink model, and the neural network-based approach, all simulations were performed on the same hardware: an $11th\ Gen\ Intel^{\odot}\ Core^{\tau M}\ i7-1165G7\ CPU\ @\ 2.80\ GHz$, with 4 cores and 8 logical processors.

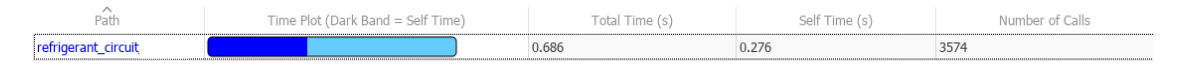


Figure 22 Computational time in the refrigerant circuit model

Electric vehicle thermal management - MathWorks

The reference model for this work is the *Electric Vehicle Thermal Management* system developed by MathWorks (Electric Vehicle Thermal Management, s.d.) As illustrated in the accompanying figure, this model represents a comprehensive thermal management system. However, for the sake of simplicity and to maintain a focused scope, the present study will utilize only the section highlighted in blue, which corresponds to the base refrigerant circuit, excluding the chiller. This subsystem accurately models the vapor-compression cycle, including its key components—the compressor, condenser, expansion valve, and evaporator—enabling a detailed analysis of the thermodynamic behaviour aligned with the physics-based Simulink model.

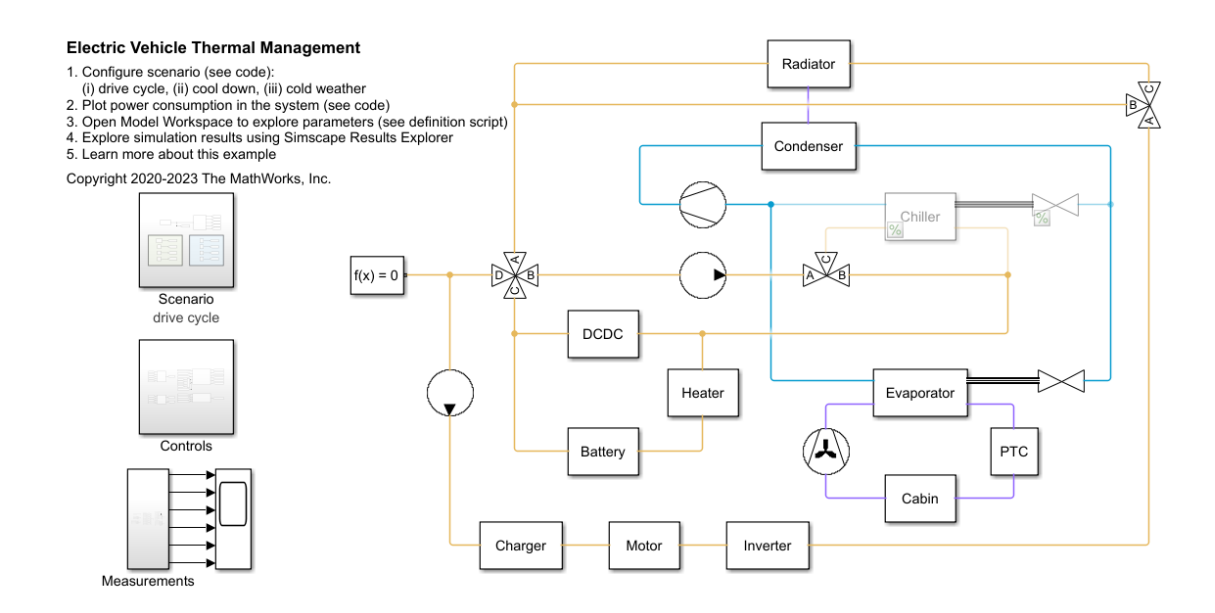


Figure 23 Electric vehicle thermal management (Electric Vehicle Thermal Management, s.d.)

A detailed analysis of the modelling approach for each element of the refrigeration cycle is presented in the following section.

The following report shows the simulation time of the Simscape model, which is approximately 10 times longer than that of the simplified Simulink model. This significantly impacts its suitability for real-time applications.



Figure 24 Computational time in the Electric vehicle thermal management

(Electric Vehicle Thermal Management, s.d.)

<u>Compressor</u>

The compressor regulates the cooling power within the refrigeration cycle and is controlled by the input signal Cmd_comp, which sets the compressor's angular velocity. In the Simscape model, the compressor is implemented as a positive displacement two-phase compressor with a displacement volume of $80 \text{ cm}^3\text{/rev}$, a nominal compression ratio of $\beta_{\text{nom}} = 4.6$, a nominal inlet pressure of $p_{\text{in,nom}} = 0.3 \text{ MPa}$, an isentropic efficiency of $\eta_{\text{isen}} = 0.65$, and a volumetric efficiency of $\eta_{\text{vol}} = 0.9$. These parameters define the compressor's thermodynamic and operational characteristics in the system.

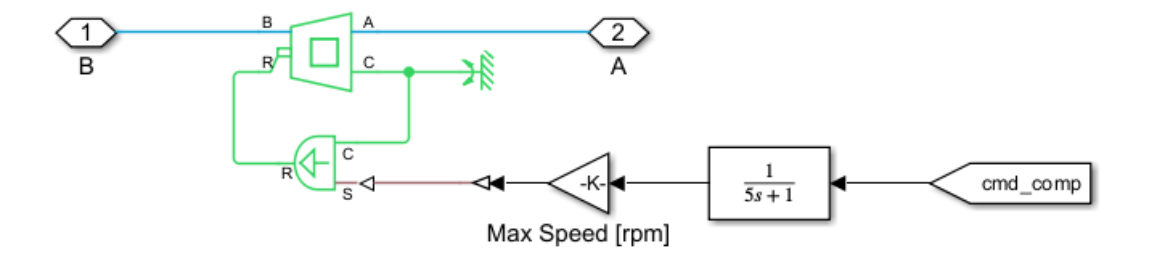


Figure 25 Compressor block (Electric Vehicle Thermal Management, s.d.)

Condenser

The subsystem comprises a tube-and-fin condenser integrated with a liquid receiver, designed to ensure efficient heat rejection and refrigerant management. The condenser fan is regulated by the control input Cmd_fan, which modulates its rotational speed as a percentage of the maximum capacity. Ambient conditions including temperature (T), pressure (P), relative humidity (RH), and CO₂ concentration are integral inputs to the model as they directly govern the convective heat transfer characteristics. The liquid receiver serves a critical role in separating vapour and ensuring only subcooled liquid refrigerant is delivered to the expansion valve, thereby enhancing system stability and efficiency. To facilitate performance analysis, sensors SR1 and SR2 are strategically placed upstream and downstream of the condenser to monitor key thermodynamic properties of the refrigerant.

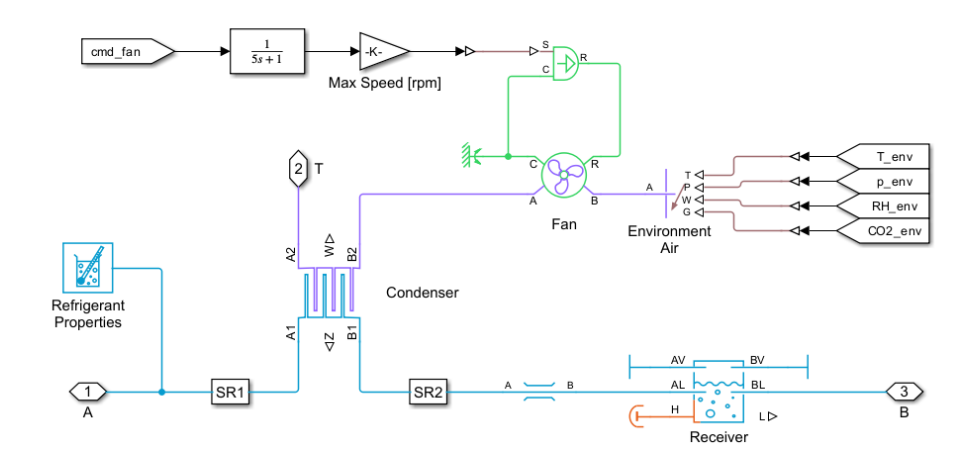


Figure 26 Condenser block (Electric Vehicle Thermal Management, s.d.)

Expansion valve

The expansion valve model regulates refrigerant mass flow into the evaporator and is designed for a nominal heat transfer capacity of 2000 W. A thermostatic sensing bulb controls valve actuation by monitoring the evaporator outlet temperature. The valve opening adjusts proportionally to the superheat, which represents the temperature difference between the bulb reading and the saturation temperature at evaporator pressure. This proportional adjustment enables dynamic modulation of refrigerant flow to maintain optimal thermodynamic conditions and ensure efficient evaporator performance.

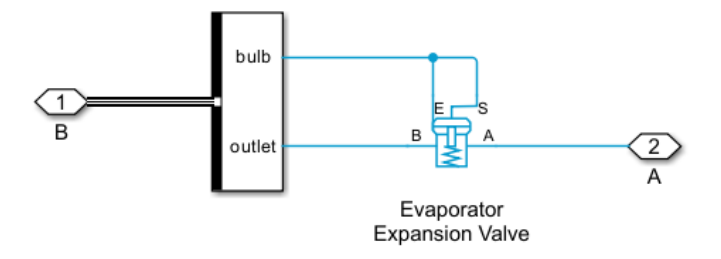


Figure 27 Expansion valve block (Electric Vehicle Thermal Management, s.d.)

Evaporator

The evaporator is a rectangular tube-and-fin heat exchanger where the refrigerant absorbs heat from the air. It includes two sensors (at inlet and outlet) to monitor key refrigerant properties, and a thermostatic bulb at the outlet that controls the opening of the expansion valve.

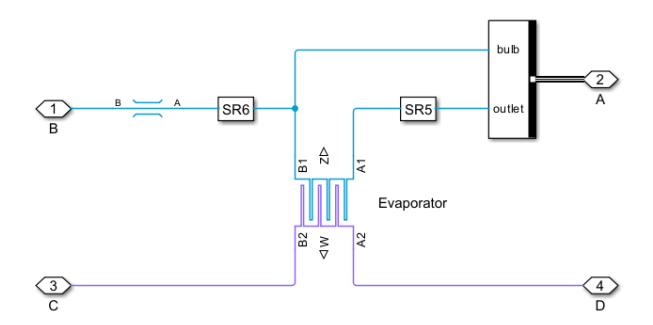


Figure 28 Evaporator block (Electric Vehicle Thermal Management, s.d.)

Comparison of the refrigerant circuits' models

Energy balance

The presented graphs show a comparison between two models used for the thermodynamic analysis of a refrigeration system, with a fluid mass flow rate of approximately 0.0045 kg/s.

The first graph is generated using the reference model developed in Simscape. It can be observed that after an initial transient phase characterized by oscillations, the system reaches a stable steady state. In this condition, the net heat transfer—defined as the difference between the heat exchanged at the condenser and the heat absorbed by the evaporator—matches perfectly the fluid power. This result confirms the energy balance compliance as dictated by the laws of thermodynamics.

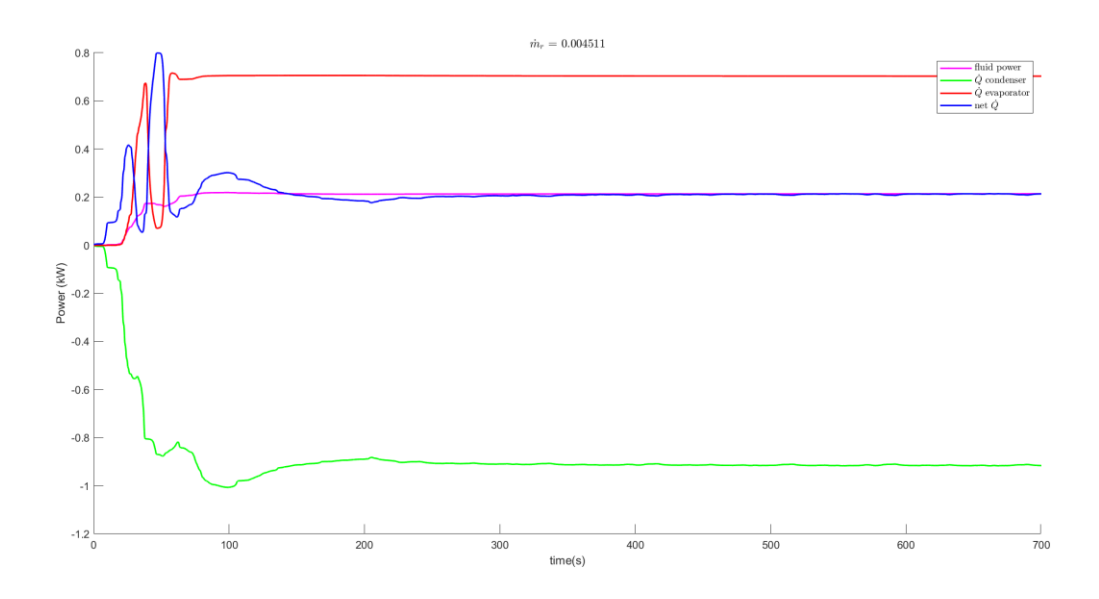


Figure 29 Energy balance - Simscape model

The second graph shows results from the approximate physics-based model, founded on analytical formulations with calibrated coefficients to ensure energy consistency. In this case, the system reaches steady state rapidly without displaying transient oscillations. The net heat transfer again corresponds to the fluid power, confirming the correct application of the energy balance.

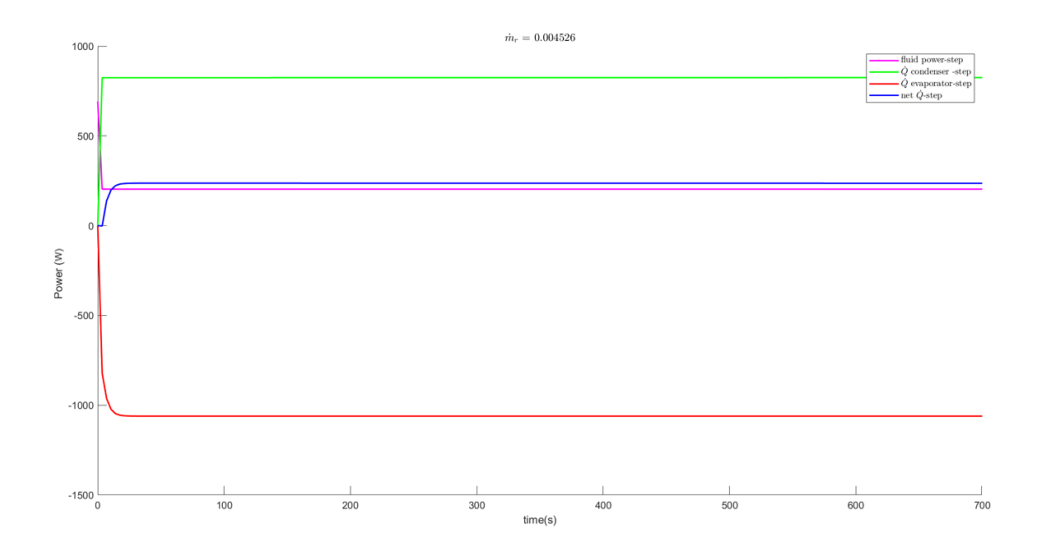


Figure 30 Energy balance – Physics-based model

The comparison between the two models highlights that the Simscape model is capable of accurately representing the real system dynamics, including initial transient phenomena, whereas the approximate physics-based model provides a simplified and steady-state description. The latter is useful for quick analyses and energy balance verification but does not capture the time-dependent dynamics that may influence system behaviour.

Step input

Considering the Simscape model, two simulations are performed for comparison: one with a constant mass flow rate and one with a step input. This approach allows for the analysis of both the steady-state behaviour and the transient response of the refrigeration system.

The results show that, under the step input, pressure, temperature, and thermal power experience a brief delay and some oscillations before stabilizing, highlighting the system's real dynamics such as fluid inertia and thermal capacitance. Conversely, the constant flow simulation represents the steady-state condition without transients. The analysis thus demonstrates how the Simscape model is effective both in describing equilibrium conditions and in capturing the system's dynamic behaviour following sudden input changes.

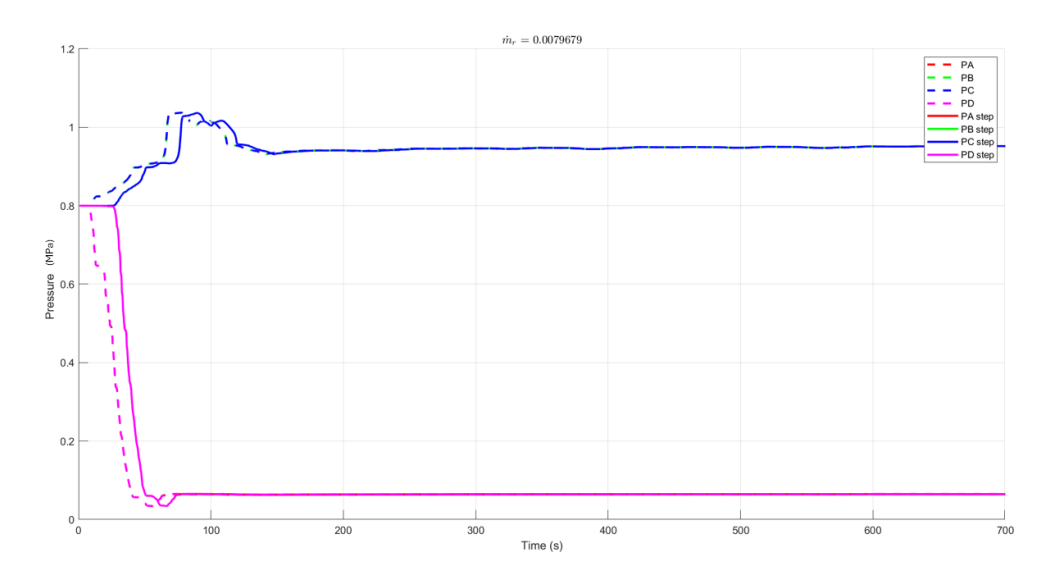


Figure 31 Pressure response - Simscape model

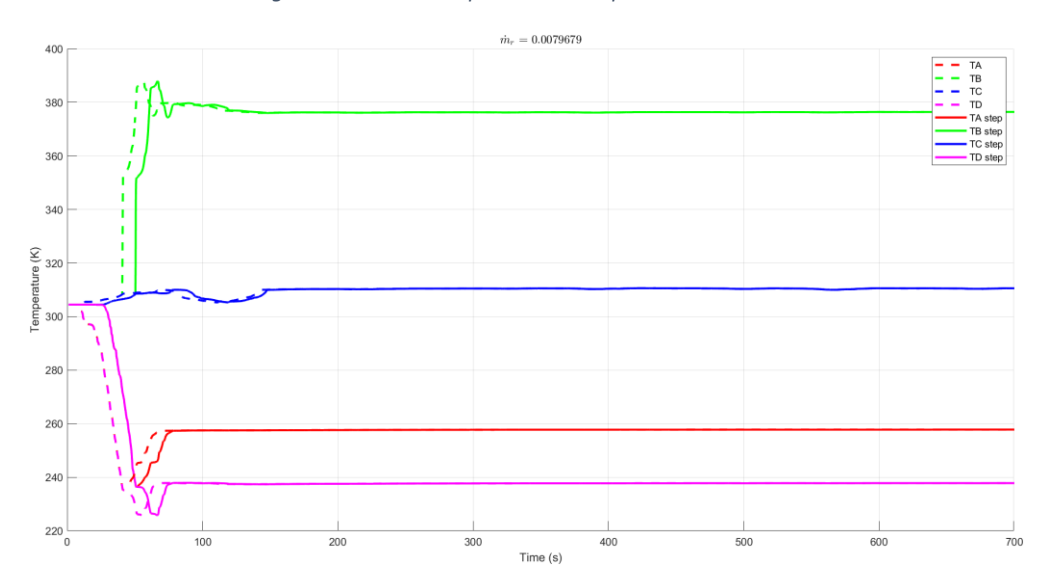


Figure 32 Temperature response - Simscape model

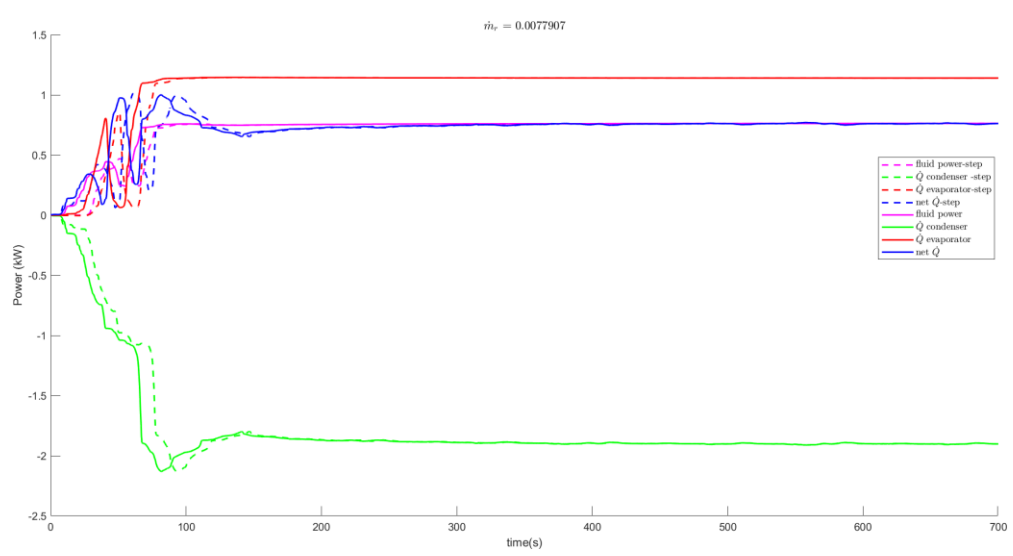


Figure 33 Power response - Simscape model

Refrigerant Mass Flow Rate and Power Balance

The two plots present a comparison of the thermal power within the refrigeration cycle as a function of refrigerant mass flow rate. It can be observed that in both instances, the magnitude of the heat transfer occurring in the evaporator and the condenser increases with higher mass flow rates. This behaviour aligns with established thermodynamic principles.

Nevertheless, an inconsistency becomes apparent in the physics-based model when examining the net power (Figure 35). Specifically, the net heat transfer does not correspond to the fluid power supplied by the compressor. This discrepancy signifies a violation of the first law of thermodynamics, indicating that the physics-based model does not accurately represent the energy balance under the given conditions. Conversely, the Simscape model produces thermodynamically consistent results, wherein the net heat transfer matches the compressor power, thereby validating its adherence to fundamental energy conservation principles (Figure 34Figure 34).

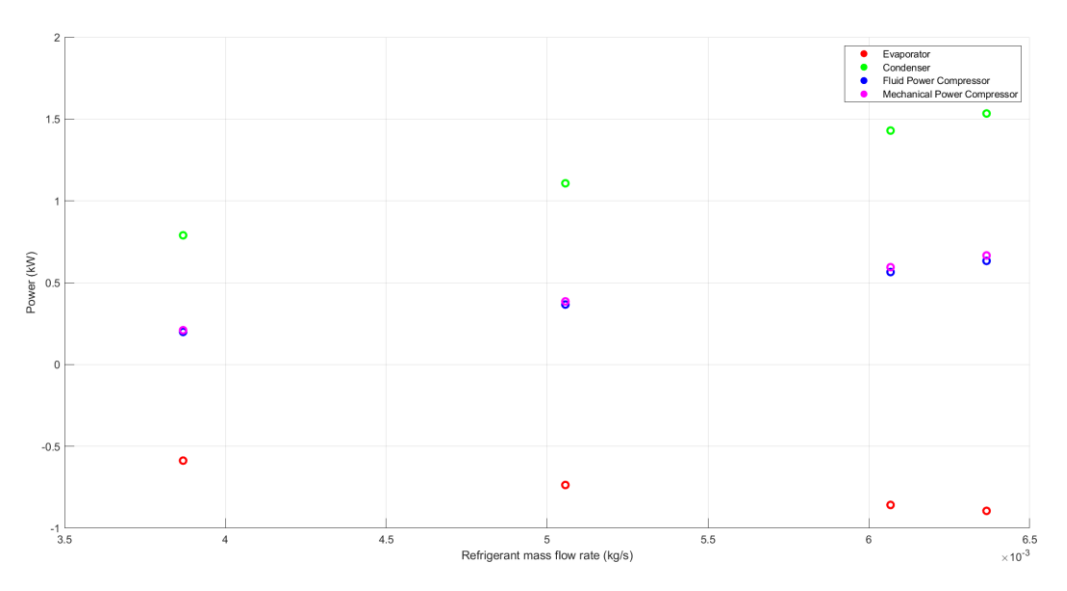


Figure 34 Power vs refrigerant mass flow rate – Simscape

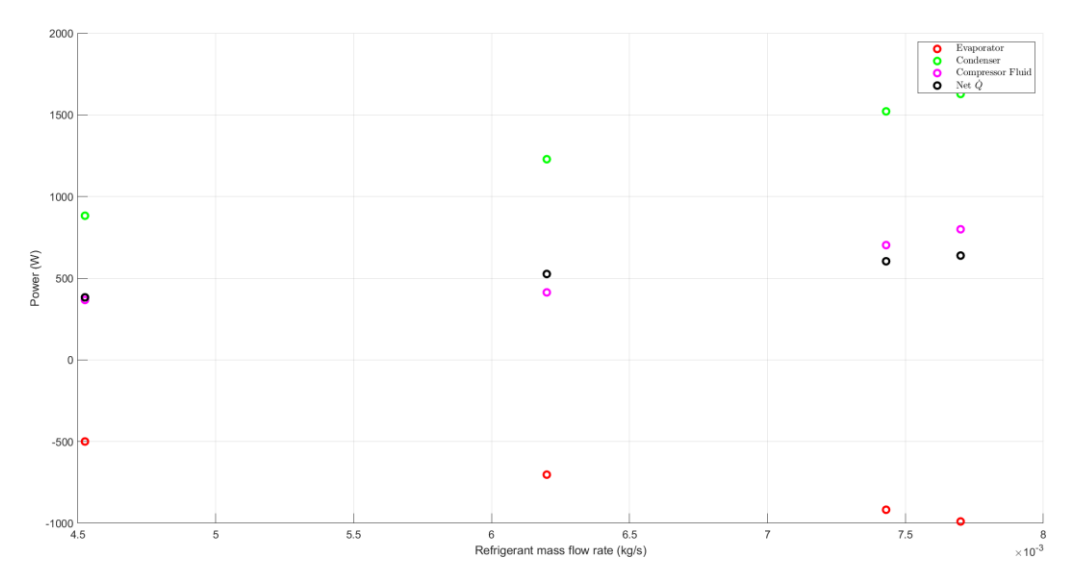


Figure 35 Power vs refrigerant mass flow rate – Physics-based model

Air Mass Flow Rate and Power Balance

This chapter analyses the relationship between heat transfer and the air mass flow rate through the condenser (m_air_condenser), comparing the performance of the reference Simscape model with the developed physics-based model.

In the Simscape model, the heat transfer demonstrates limited sensitivity to variations in air mass flow rate. A modest increase is observed as the flow rate rises from 0.1 kg/s to 0.27 kg/s, with condenser heat transfer increasing from approximately 1.2 kW to 1.4 kW. Beyond this threshold, the heat transfer remains almost stable. The model exhibits strong thermodynamic consistency, as the fluid power delivered by the compressor aligns closely with the net system heat transfer, thereby adhering to energy conservation principles. Additionally, the mechanical power supplied to the compressor marginally exceeds the fluid power, which appropriately accounts for mechanical losses.

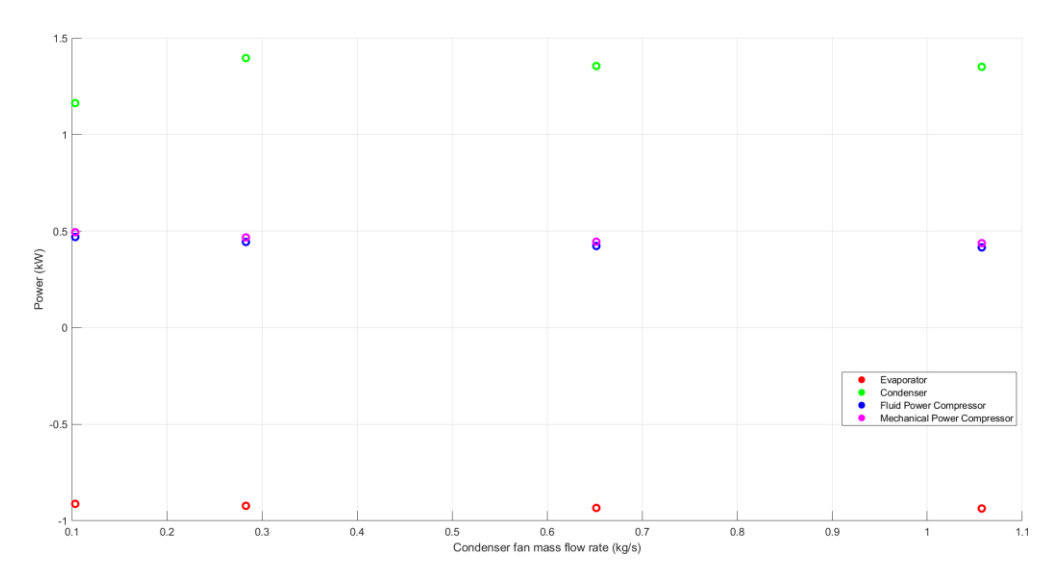


Figure 36 Power vs air mass flow rate – Simscape

The physics-based model exhibits distinct behavioural characteristics. The evaporator heat transfer remains largely consistent across variations in condenser air flow, showing minimal sensitivity to changes in \dot{m} _air. Meanwhile, the condenser demonstrates significantly greater dependence on air mass flow rate, with heat rejection showing a pronounced positive correlation with increasing \dot{m} _air. This enhanced sensitivity aligns closely with fundamental heat transfer principles governing forced convection processes.

Moreover, this model exhibits occasional discrepancies between net heat transfer and compressor fluid power. This deviation stems from the model's simplified structure, which relies on empirical correlations and parameterized approximations rather than enforcing strict thermodynamic conservation laws. While this approach successfully captures general system behaviour across operational conditions, it does not guarantee precise energy balance in all scenarios.

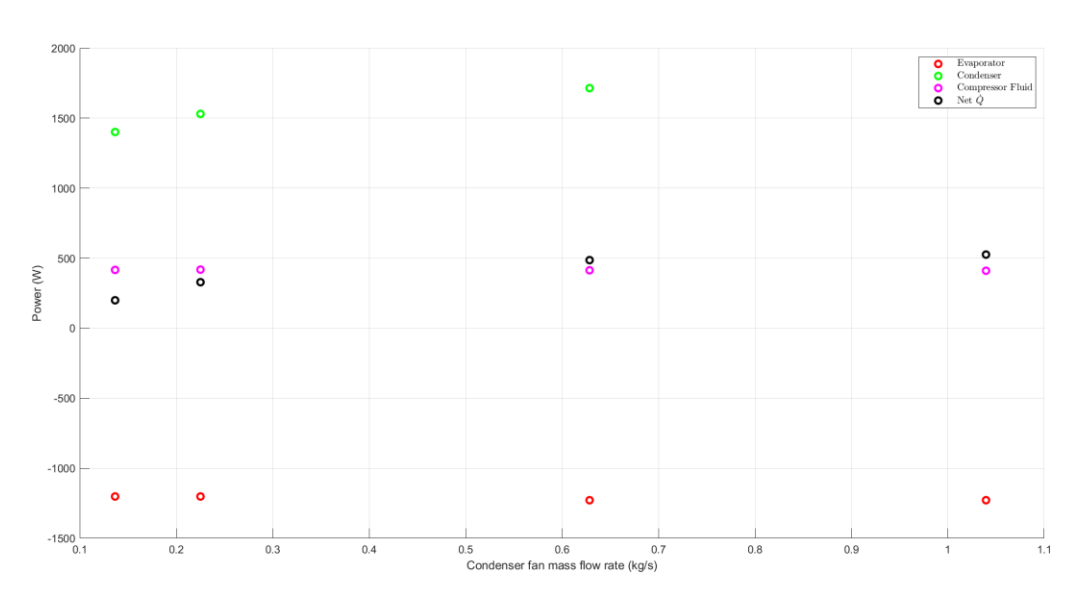


Figure 37 Power vs air mass flow rate – Physics-based model

Pressure-Temperature diagram

The figures present the reference pressure-temperature (p-T) diagram, highlighting all characteristic thermodynamic states of the refrigeration cycle. Points A, B, C, and D represent the refrigerant conditions at key system sections: evaporator, compressor, condenser, and expansion valve, respectively.

The Simscape model, illustrated in Figure 38Figure 38, serves as the reference for validating the proposed physics-based modelling approach.

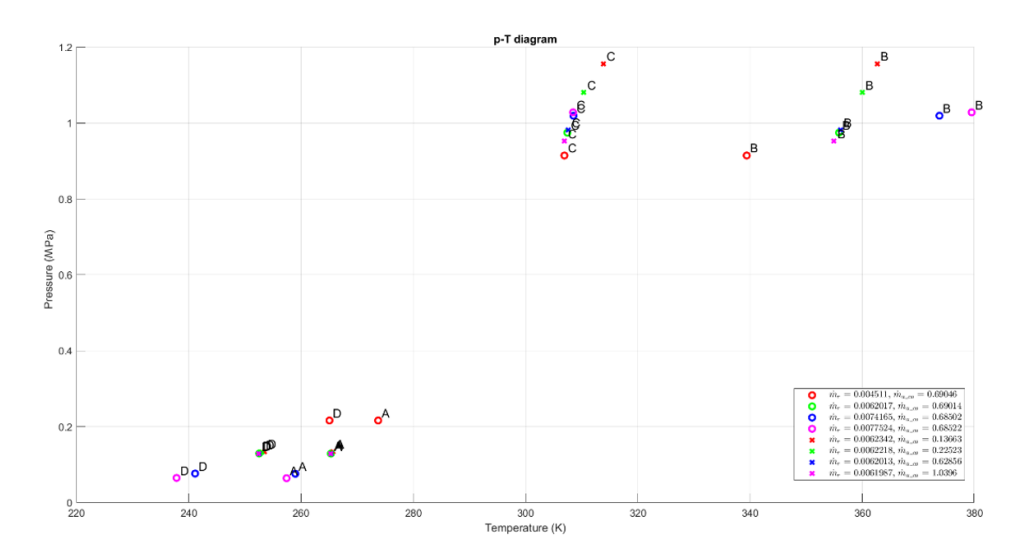


Figure 38 p-T diagram - Simscape

In the physic-based model, the thermodynamic states represented in the pressure-temperature (p-T) diagram reveal significant inaccuracies in the predicted values of TB when compared to expected thermodynamic behaviour. This deviation is originated from the compressor model, where the outlet temperature Tout(t) is calculated using a polynomial expression based on mass flow rate and pressure rise:

$$T_{c_{\text{out}}}(t) = T_{c_{\text{in}}}(t) + \sum_{i=0}^{4} \sum_{j=0}^{3} \kappa_{ij} \dot{m}_{compressor}^{i}(t) \Delta p_{c}^{j}(t)$$

The root cause of this deviation lies in the insufficiently accurate estimation of the polynomial coefficients kij, which are determined using linear interpolation from a restricted dataset. This methodological limitation propagates through the model, also compromising the accuracy of TC.

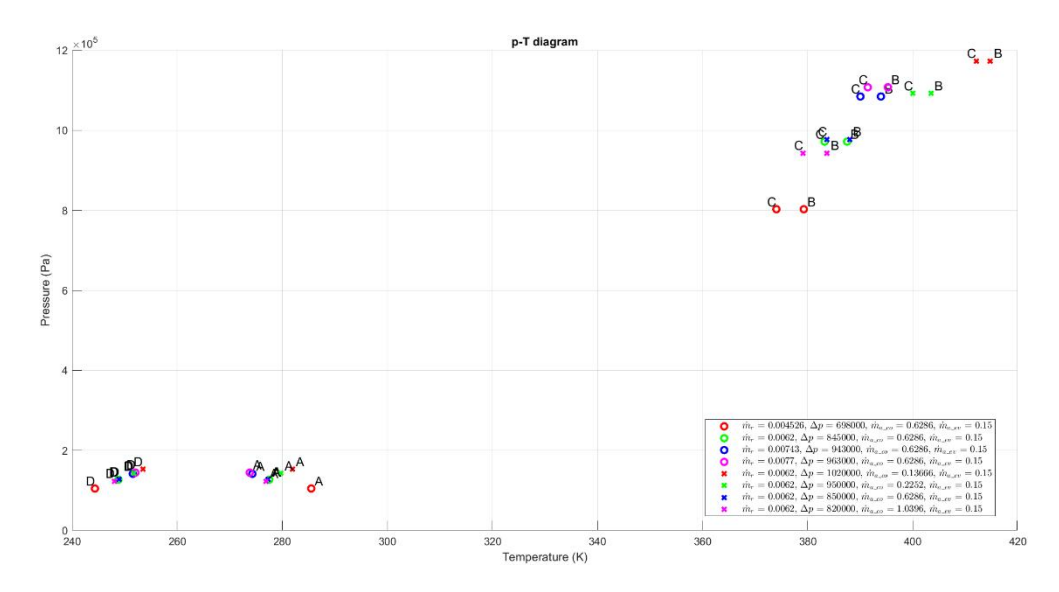


Figure 39 p-T diagram – Physis-based model

For this reason, a better version of the diagram, in which the TB values are directly imposed, is also presented. This allows for a clearer visualization of the expected cycle behaviour.

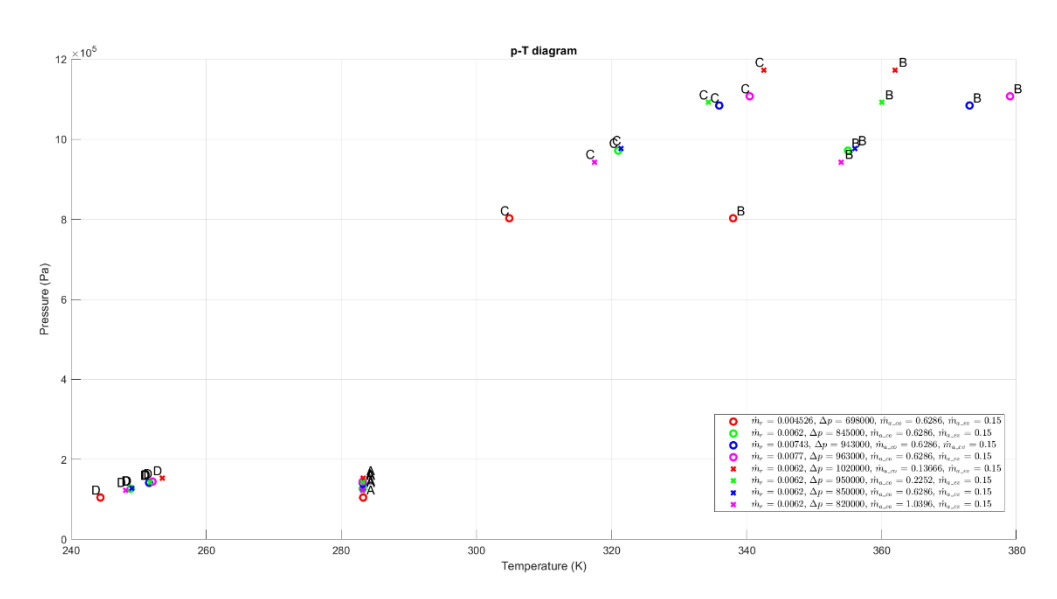


Figure 40 p-T diagram - Physics-based model

3.6 Bench models

The goal of this work is to test each block of an HVAC system individually on a simulation bench, in order to collect data under various operating conditions. The collected data will be used to generate plots and build look-up tables. By combining multiple parameters, the study aims to better understand the system behaviour and performance across different working ranges.

3.6.1 Condenser

The condenser in a vehicle HVAC system is analysed using a Condenser Bench modelled in Simulink/Simscape (Condenser and Evaporator, s.d.) to evaluate its thermal performance. It functions by transferring heat from the refrigerant to the surrounding air, causing the refrigerant to condense from a superheated vapor into a two-phase mixture and eventually into a subcooled liquid. The condenser is a critical component, as variations in its efficiency impact refrigerant phase transitions, pressure levels, and the overall energy performance of the refrigeration cycle

The bench integrates four main components:

- A *fan*, which controls airflow through the system based on input speed;
- An *environment block*, which simulates external ambient conditions such as pressure, temperature, relative humidity, and CO₂ concentration;
- A *condenser model*, where heat transfer between the refrigerant and moist air occurs, transitioning the refrigerant from superheated vapor to subcooled liquid;
- A *mass flow source*, which injects refrigerant into the condenser loop.

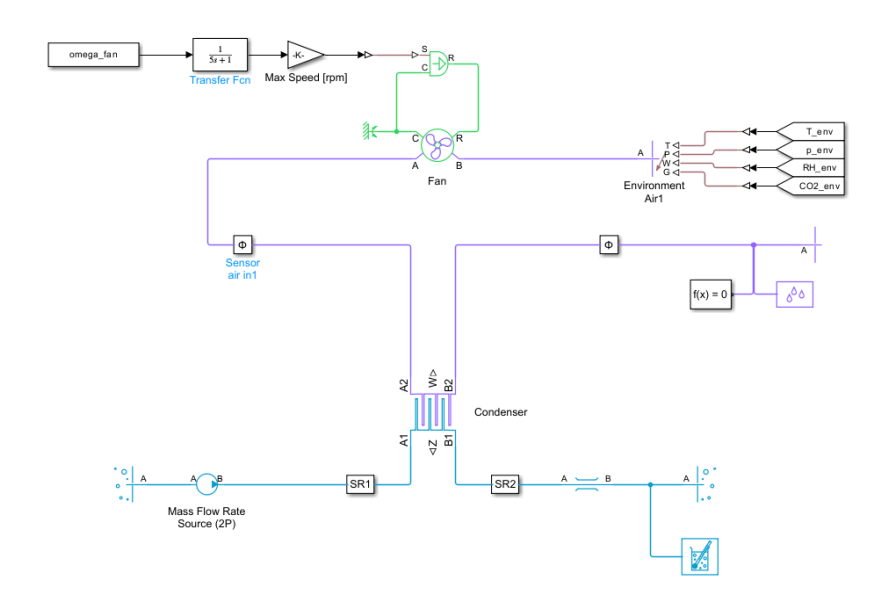


Figure 41 Condenser Bench (Condenser and Evaporator, s.d.)

The analysis doesn't aim to merely reproduce the expected phase change process, but rather to quantify how the condenser responds when subjected to variations in its control parameters. For this reason, the refrigerant mass flow rate and the fan speed are systematically modified, while ambient conditions are kept constant in order to isolate the influence of the operating variables.

Control action			
Refrigerant mass flow rate (kg/s) mdot_r [0.004526, 0.0062, 0.00743, 0.00743]			
Condenser fan speed control (%)	omega_fan	[0.05, 0.1, 0.33, 0.5]	

Operating conditions			
Refrigerant Pressure (MPa)	Р	[0.9, 1.0, 1.1, 1.2]	
Refrigerant Temperature Reservoir Input (K)	ТВ	[330, 345, 360, 375]	
Refrigerant Temperature Reservoir Output (K)	TC	[300, 315, 330]	

Environment		
Pressure (MPa)	P_env	0.101325
Temperature (°C)	T_env	30
Relative Humidity (%)	RH_env	0.4
CO2 Fraction	CO2_env	4e-4

Table 1 Condenser bench operating variables

Effect of refrigerant mass flow rate

The plot displays a strong linear increase in the heat transfer rate \dot{Q} as the refrigerant mass flow rate increases from 0.0045 kg/s to 0.0077 kg/s. The thermal power output grows from approximately 960 W to over 1650 W across this range. This trend aligns with thermodynamic expectations, as the transferred heat is directly proportional to the mass flow rate times the enthalpy change of the refrigerant ($\dot{Q} = \dot{m}_r \Delta h$).

At a higher flow rate, more refrigerant mass carries thermal energy into the condenser, increasing the overall heat transfer. This result indicates that mass flow rate is a dominant control variable for regulating condenser performance, making it a powerful tool for thermal load management in HVAC systems.

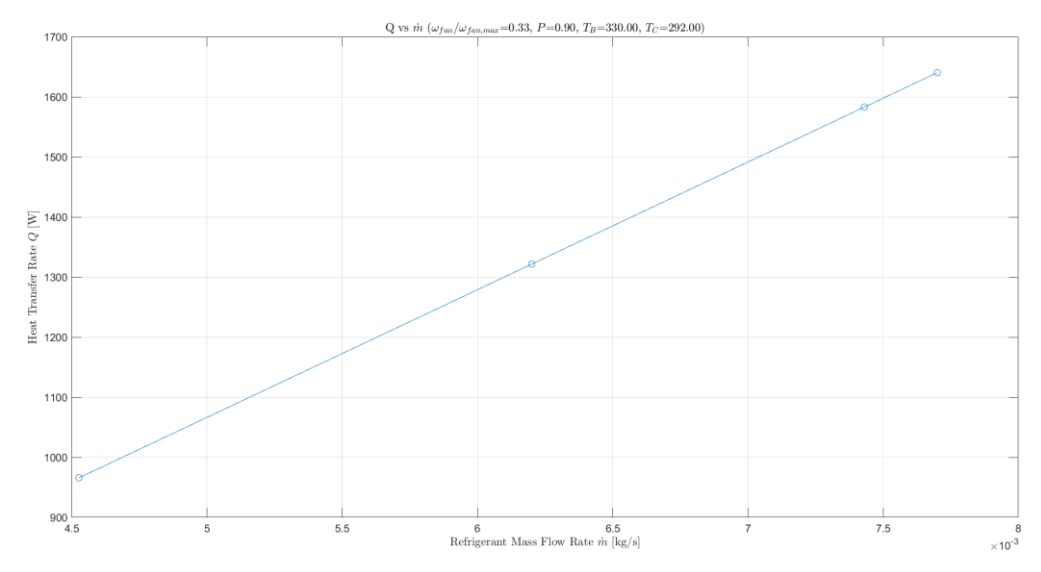


Figure 42 Condenser heat transfer rate over refrigerant mass flow rate

Effect of fan speed

Contrary to the mass flow rate, the influence of fan speed on \dot{Q} appears to be negligible within the tested range (5% to 50% of maximum speed). The heat transfer rate remains virtually constant around 965–966 W, showing a variation of less than 1%.

This behaviour suggests that, under the given operating conditions (low refrigerant mass flow and moderate ambient temperature), the air-side convective heat transfer is not a limiting factor. The airflow provided by the fan, even at lower speeds, is sufficient to maintain the condenser's effectiveness. Additional increases in fan speed do not result in improved thermal performance, highlighting that the system might already be operating in a thermally efficient convective regime.

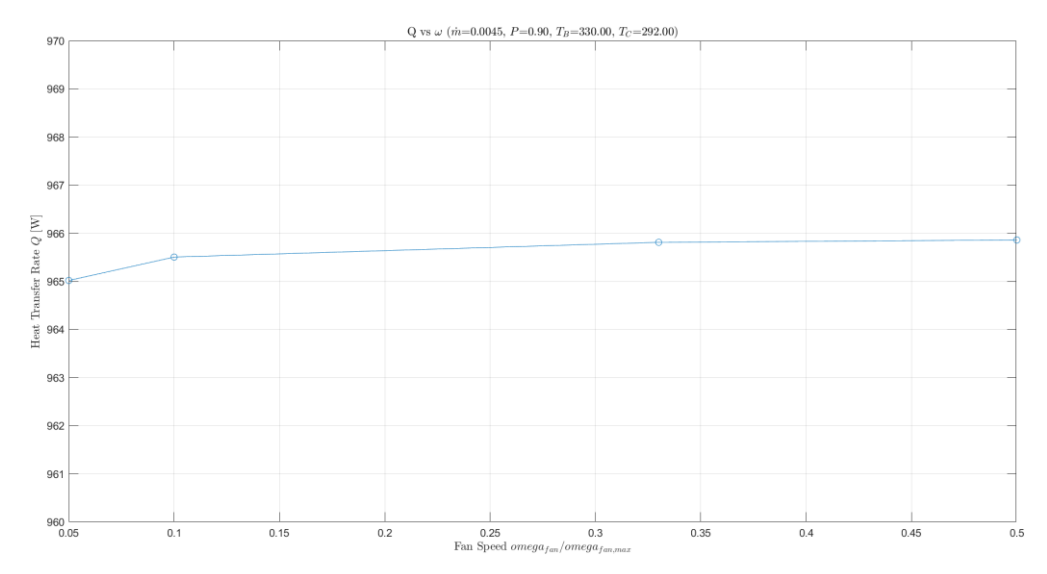


Figure 43 Condenser heat transfer rate over fan speed

Effect of refrigeration pressure

The following graph shows an inverse relationship between refrigerant pressure and heat transfer rate. As the pressure increases from 0.9 MPa to 1.2 MPa, the thermal output decreases from approximately 966 W to 943 W.

This trend is explained by the fundamental thermodynamics of the refrigerant. An increased pressure raises saturation temperature of the refrigerant, as a consequence the temperature gradient between the refrigerant and the surrounding air, which is the driving force for heat transfer, is reduced. Moreover, at higher pressures, the latent heat released during phase change may decrease and the total enthalpy change (Δh) is reduced.

Since this experiment is conducted on a bench model where the mass flow rate is held constant, the reduction in enthalpy change (Δh) directly results in a lower thermal output (\dot{Q}). Therefore, under these fixed conditions of mass flow, temperature, and air flow, a higher operating pressure diminishes the condenser's heat rejection capacity.

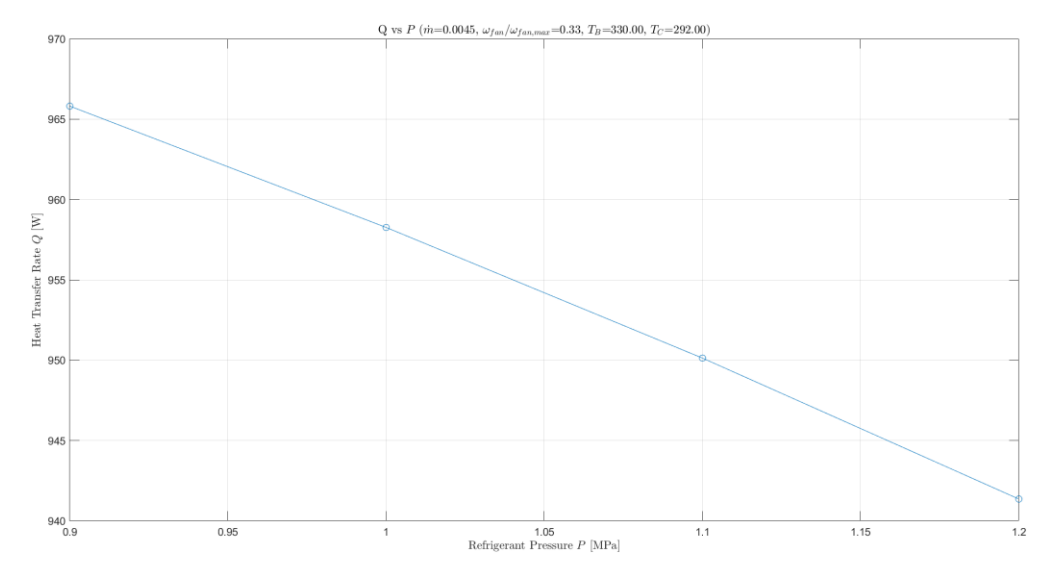


Figure 44 Condenser heat transfer rate over refrigerant pressure

Effect of refrigeration temperature reservoir input

The correlation between inlet refrigerant temperature and condenser heat transfer rate results linear, because increasing TB from 330 K to 375 K results in a rise in \dot{Q} from around 965 W to more than 1180 W.

This trend is expected for two key reasons. First, a higher inlet temperature means the refrigerant enters the condenser with a greater initial thermal energy content. This directly increases the enthalpy difference available for rejection. Second, the higher refrigerant

temperature creates a larger mean temperature difference against the ambient air, which is the primary driving force for convective heat transfer.

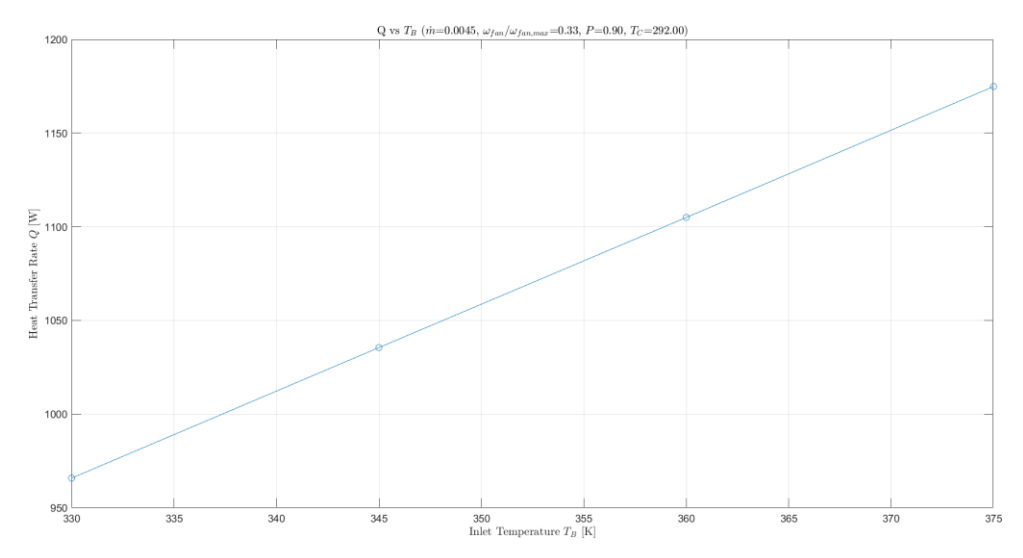


Figure 45 Condenser heat transfer rate over refrigerant inlet temperature TB

Effect of refrigeration temperature reservoir output

The plot demonstrates that adjusting the outlet refrigerant temperature, TC, within a range of 292 K to 294 K, has a negligible effect on the system's heat transfer rate. The thermal output remains stable at approximately 965 W despite these variations.

This suggests that the outlet refrigerant temperature is a dependent variable determined by the system's energy balance, not an independent control parameter. Consequently, its variation (TC) has a negligible effect on the total heat rejection capacity. This is because the predominant latent heat is rejected during the phase change process, with only a minor additional contribution from sensible cooling in the subsequent subcooling region.

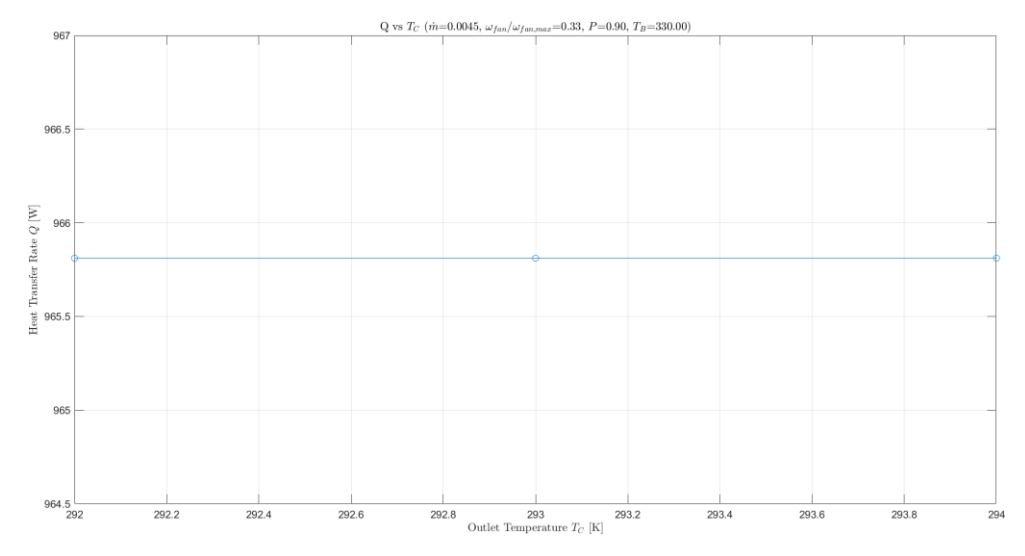


Figure 46 Condenser heat transfer rate over refrigerant outlet temperature TC

A structured lookup table (LUT) is generated from the simulation data to comprehensively map the condenser's thermal behaviour across a wide range of operating conditions. This LUT enables the identification of critical performance trends and input-output dependencies, forming an essential resource for component-level analysis and a verifiable model for integration into broader system simulations.

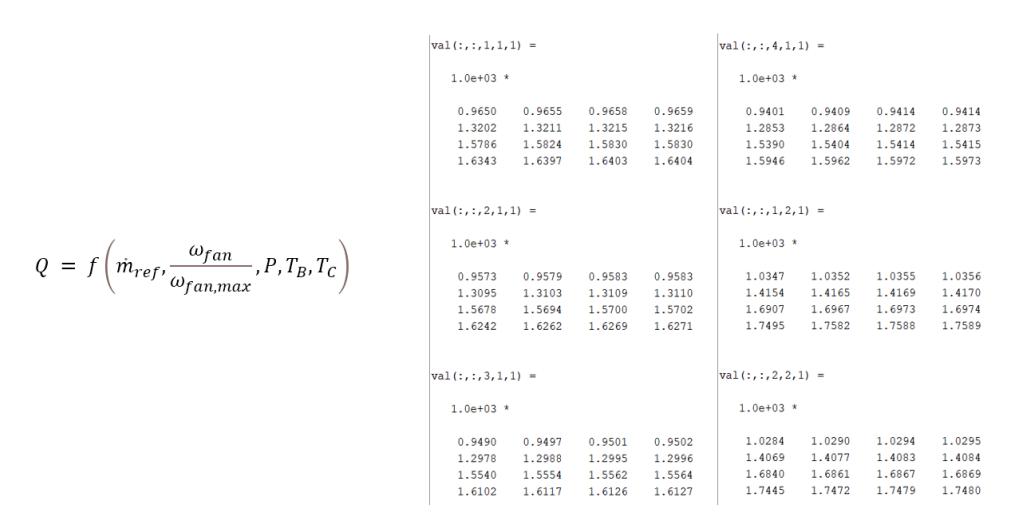


Figure 47 Condenser LUT

To gain a more comprehensive understanding of the system's behaviour, the heat transfer rate is visualized within a multi-variable operational space. A three-dimensional surface plot is constructed, mapping \dot{Q} against the primary controlling variables: refrigerant pressure (P) and inlet temperature (TB). This mapping is further elaborated by generating a family of surfaces, each corresponding to a distinct refrigerant mass flow rate (\dot{m}_r) .

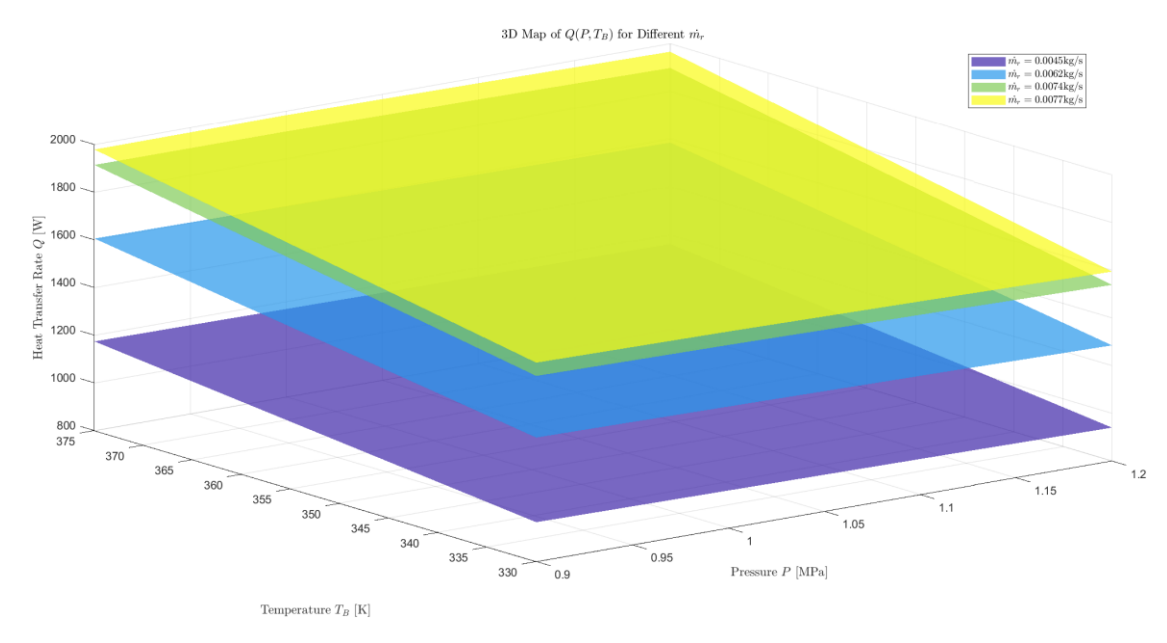


Figure 48 3D Map of $Q_{condenser}(P,T_B)$ for different \dot{m}_r

3.6.2 Evaporator

Following the condenser analysis, the focus shifts to the evaporator, the component responsible for cooling and dehumidifying the cabin air. While its thermodynamic role in the refrigeration cycle has been established, this section examines how its performance varies under different operating conditions. The evaporator's ability to maintain a stable cooling capacity is the fundamental link to passenger comfort; therefore, a thorough understanding of its component-level behaviour is crucial for optimizing the design and control of the entire HVAC system.

To conduct this investigation, a dedicated simulation test bench was developed in Simulink/Simscape. The bench integrates the following key components:

- a **blower**, which regulates the airflow across the heat exchanger;
- an *environment block*, reproducing the climatic conditions of the passenger cabin;
- the *evaporator model*, where the refrigerant absorbs heat from the incoming air and undergoes phase change from liquid to vapor;
- a *mass flow source*, ensuring refrigerant supply to the circuit.

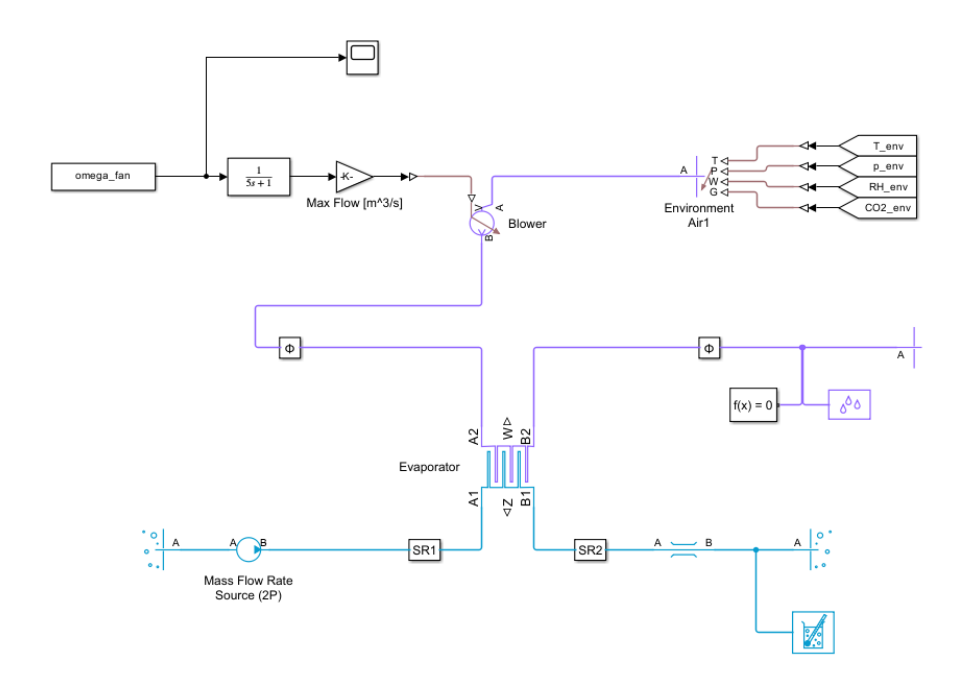


Figure 49 Evaporator Bench (MathWorks, s.d.)

The simulation campaign is designed to evaluate evaporator performance under controlled conditions. Refrigerant mass flow rate and blower speed are systematically varied as independent control variables, with all environmental boundaries maintained at fixed values. This strategy enabled a precise analysis of their individual effects on both system-level cooling capacity and local refrigerant thermodynamic properties.

Control action		
Refrigerant mass flow rate (kg/s)	mdot_r	[0.004526, 0.0062, 0.00743, 0.0077]
Evaporator fan mass flow rate control (%)	mdot_a/mdot_a,max	[0.2, 0.3, 0.4, 0.5]

Operating conditions			
Refrigerant Pressure (MPa) P [0.05, 0.1, 0.2, 0.25]			
Refrigerant Temperature Reservoir Input (K)	TD	[235, 250, 265, 275]	
Refrigerant Temperature Reservoir Output (K)	TA	[250, 265, 280];	

Environment		
Pressure (MPa)	P_env	0.101325
Temperature (°C)	T_env	30
Relative Humidity (%)	RH_env	0.4
CO2 Fraction	CO2_env	4e-4

Table 2 Evaporator bench operating variables

Effect of refrigerant mass flow rate

A linearly proportional relationship is evident between the refrigerant mass flow rate (\dot{m}) and the evaporator's heat transfer rate (\dot{Q}) . According to thermodynamic principles, a higher mass flow rate increases the enthalpy flow rate, thus enhancing the refrigerant's capacity to absorb thermal energy from the air and intensifying the heat exchange process.

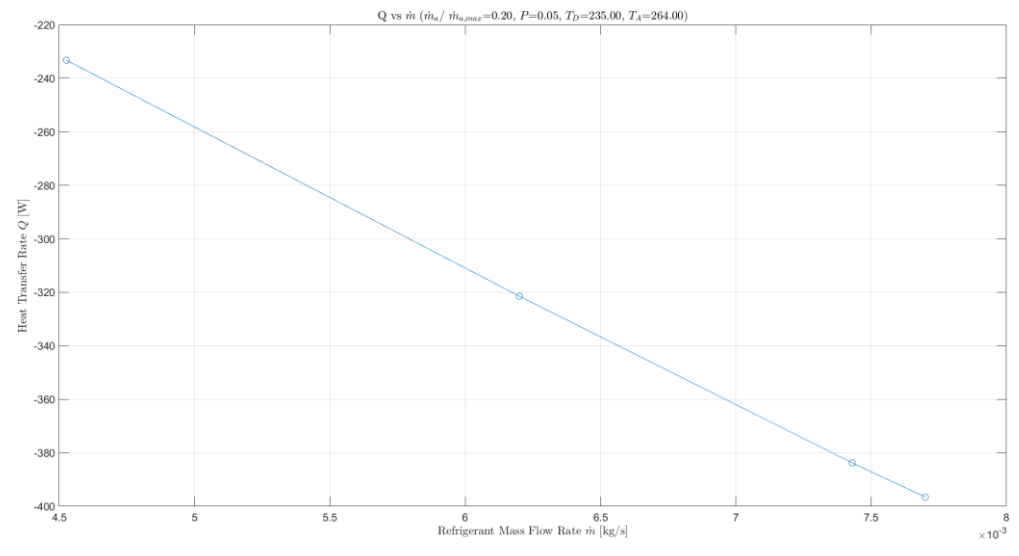


Figure 50 Evaporator heat transfer rate over refrigerant mass flow rate

Effect of ait mass flow rate

The plot demonstrates that the influence of air flow rate on heat transfer is secondary to that of the refrigerant mass flow rate. The effect of air flow exhibits a non-linear behaviour with diminishing returns: while an initial increase in air flow enhances heat transfer by improving convection, the marginal gain decreases significantly beyond a normalized air flow rate of approximately 0.35. At this point, the dominant thermal resistance is no longer on the air side, making further increases in air flow energetically unjustifiable relative to the limited performance improvement achieved.

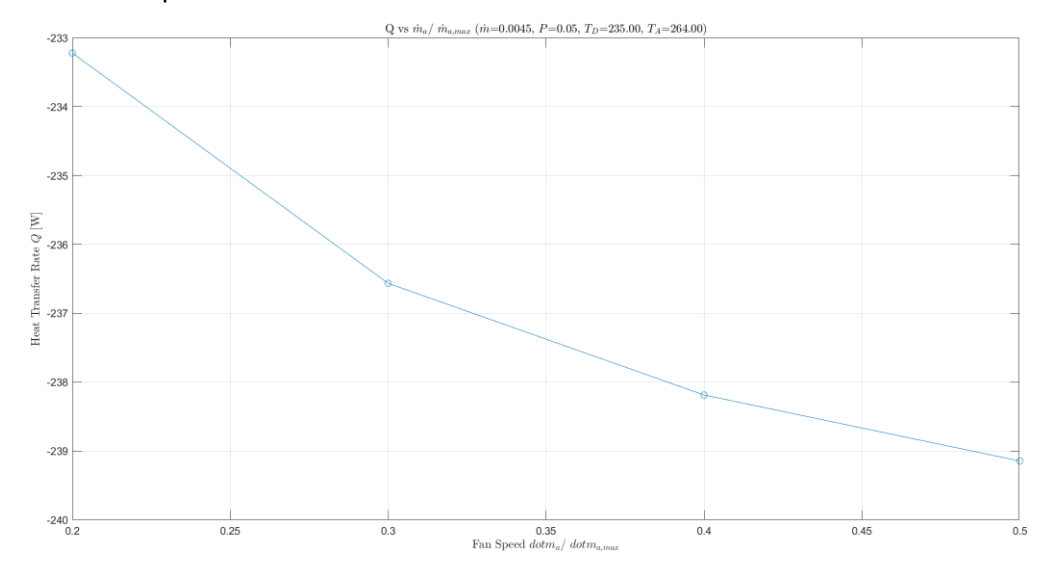


Figure 51 Evaporator heat transfer rate over air mass flow rate

Effect of refrigerant pressure

The data reveals a steep increase in the heat transfer rate, \dot{Q} , as pressure rises from 0.05 MPa to an optimum of 0.10 MPa, an enhancement attributed to highly efficient two-phase boiling. Beyond this peak, further pressure increases elevate the saturation temperature, shifting the refrigerant away from its ideal state for latent heat absorption and consequently degrading evaporator performance.

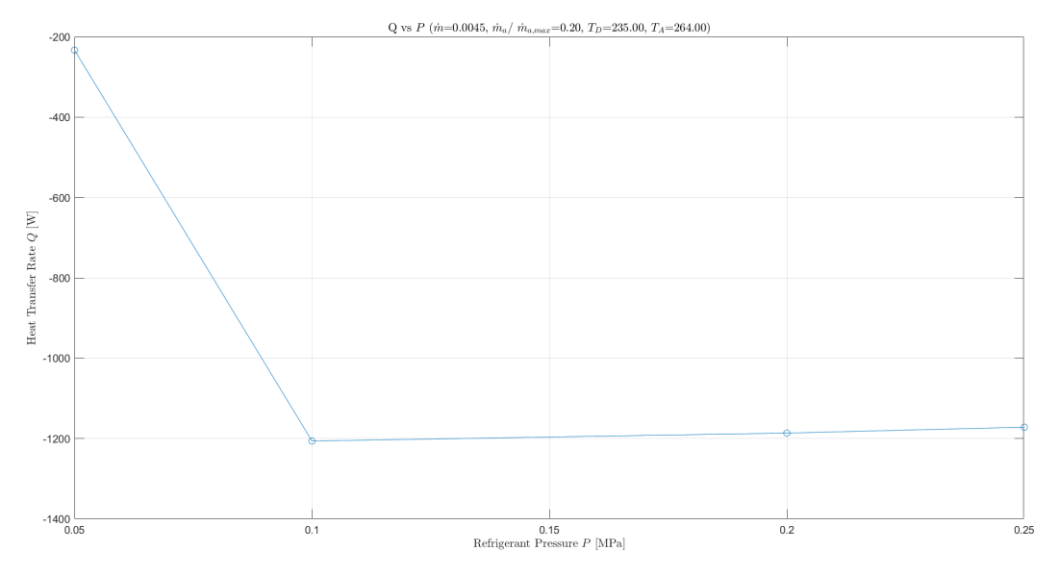


Figure 52 Evaporator heat transfer rate over refrigerant pressure

Effect of refrigerant inlet temperature

The plot indicates that an increase in the refrigerant inlet temperature TD leads to a consistent decrease in the absolute heat transfer rate $|\dot{Q}|$, signifying a reduction in the evaporator's heat absorption capacity. This behaviour is governed by thermodynamic principles, as a higher TD reduces the temperature difference between the refrigerant and the air, thus diminishing the driving potential for heat exchange. Consequently, the bench models shows that system performance is maximized by minimizing the refrigerant inlet temperature.

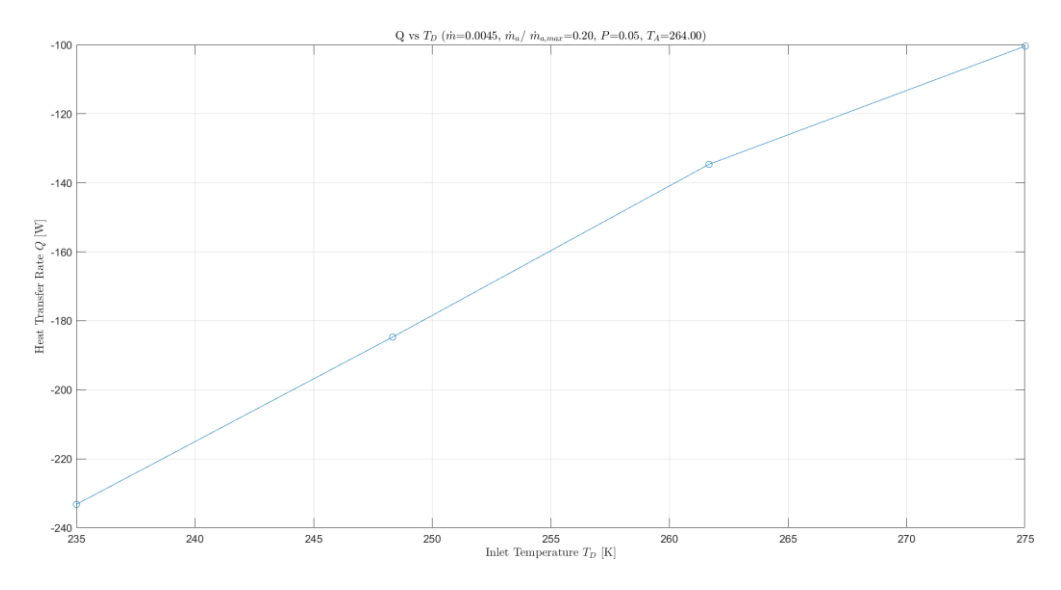


Figure 53 Evaporator heat transfer rate over refrigerant inlet temperature

Effect of refrigerant outlet temperature

The experimental results demonstrate that the air outlet temperature (TA) has a negligible influence on the heat transfer rate (\dot{Q}) across the tested operational range. This indicates that the evaporator's thermal performance is predominantly governed by the inlet conditions and refrigerant-side properties.

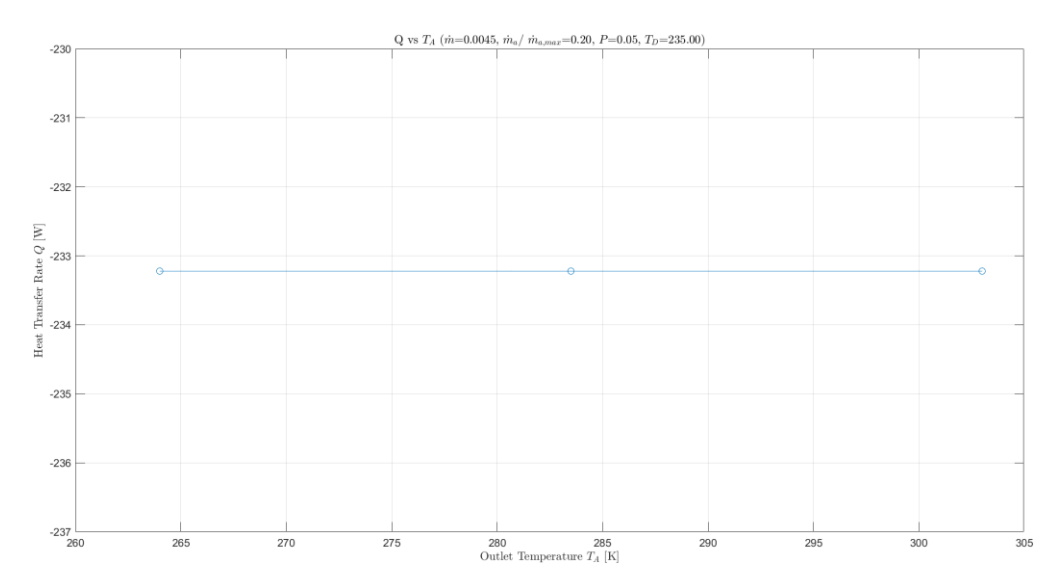


Figure 54 Evaporator heat transfer rate over refrigerant outlet temperature

The simulation results are subsequently post-processed and compiled into a lookup table (LUT). This LUT provides a compact yet comprehensive representation of the evaporator's performance, defining the heat transfer rate as a function of the following key parameters: refrigerant mass flow rate, air mass flow rate, refrigerant pressure, and refrigerant inlet and outlet temperatures.

$$Q = f\left(\dot{m}_{ref}, \frac{\dot{m}_a}{\dot{m}_{a,max}}, P, T_D, T_A\right) \\ \begin{bmatrix} val(:,:,1,1,1) = \\ -233.2212 - 236.5656 - 238.1871 - 239.1461 \\ -321.4659 - 326.7142 - 329.0670 - 330.3825 \\ -383.7591 - 391.2103 - 394.3889 - 396.0965 \\ -396.5536 - 404.7118 - 408.1880 - 410.0510 \\ -1.5028 - 1.6166 - 1.6366 - 1.6432 \\ -1.5028 - 1.6166 - 1.6366 - 1.6432 \\ -1.5028 - 1.6166 - 1.6366 - 1.6432 \\ -1.5069 - 1.8913 - 1.9496 - 1.9653 \\ -1.5076 - 1.9413 - 2.0146 - 2.0341 \\ -1.2063 - 1.2138 - 1.2162 - 1.2174 \\ -1.6443 - 1.6638 - 1.6686 - 1.6705 \\ -1.9333 - 1.9893 - 1.9893 - 2.0020 \\ -1.9976 - 2.0596 - 2.0706 - 2.0742 \\ -1.9976 - 2.0596 - 2.0706 - 2.0742 \\ -1.865 - 1.2003 - 1.2043 - 1.2041 \\ -1.5824 - 1.6374 - 1.6490 - 1.6531 \\ -1.5824 - 1.6374 - 1.6490 - 1.6531 \\ -1.7585 - 1.9424 - 1.9716 - 1.9799 \\ -1.7575 - 2.0039 - 2.00403 - 2.0055 \\ -2.00704 - 2.0059 - 311.7849 - 317.4408 - 318.6862 \\ -383.5719 - 257.9428 - 262.4142 - 264.4340 - 265.5687 \\ -308.5690 - 314.7849 - 317.4408 - 318.6862 \\ -318.9018 - 325.7074 - 328.6124 - 330.1699 \\ -318.9018 - 325.7074 - 328.6124 - 330.1$$

Figure 55 Evaporator LUT

To better visualize the evaporator's behaviour, a three-dimensional performance map is constructed using the evaporator pressure and the refrigerant inlet temperature as the primary independent variables. The heat transfer rate (\dot{Q}) is represented on the vertical axis. This mapping is further elaborated by generating a family of surfaces, each corresponding to a distinct refrigerant mass flow rate.

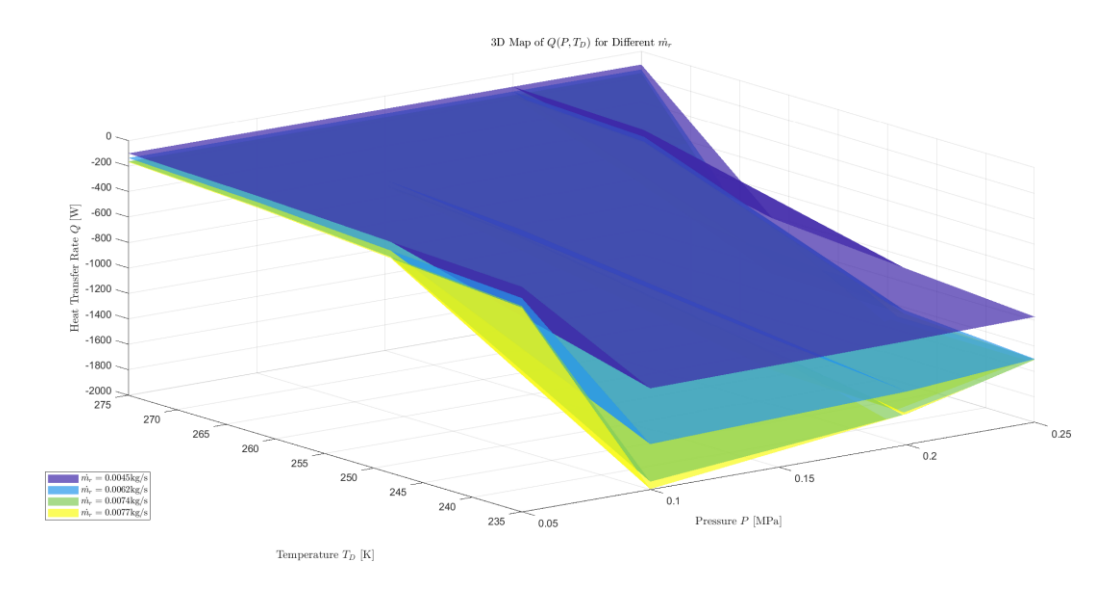


Figure 56 3D Map of Qevaporator(P,T_D) for different \dot{m}_r

3.6.3 Expansion valve

The expansion valve's performance is evaluated using a specialized test bench that replicates automotive HVAC conditions. Its primary function is to create a precise pressure drop, resulting in an isenthalpic (constant enthalpy) process that reduces refrigerant temperature. This phase change is essential for effective evaporation and heat absorption. The valve also critically regulates superheat to ensure system efficiency and protect the refrigerant loop.

The bench setup is composed of the following key components:

- Controlled Reservoir: Simulates the thermodynamic state of the refrigerant by allowing
 control over pressure, enthalpy, and vapor quality. This ensures the desired input
 conditions are maintained for testing.
- An Expansion Valve: enforces the pressure reduction and initiates the cooling process by enabling the expansion of the refrigerant into a lower-pressure region.
- A Mass Flow Source: Regulates and injects the refrigerant mass flow into the test loop, allowing simulation of different operating loads and conditions typical of condenser output.

 An Accumulator: Acts as a passive volume that collects and separates liquid and vapor refrigerant after expansion. It allows the outlet pressure to evolve naturally without being imposed, enabling accurate simulation of pressure drop across the expansion valve.

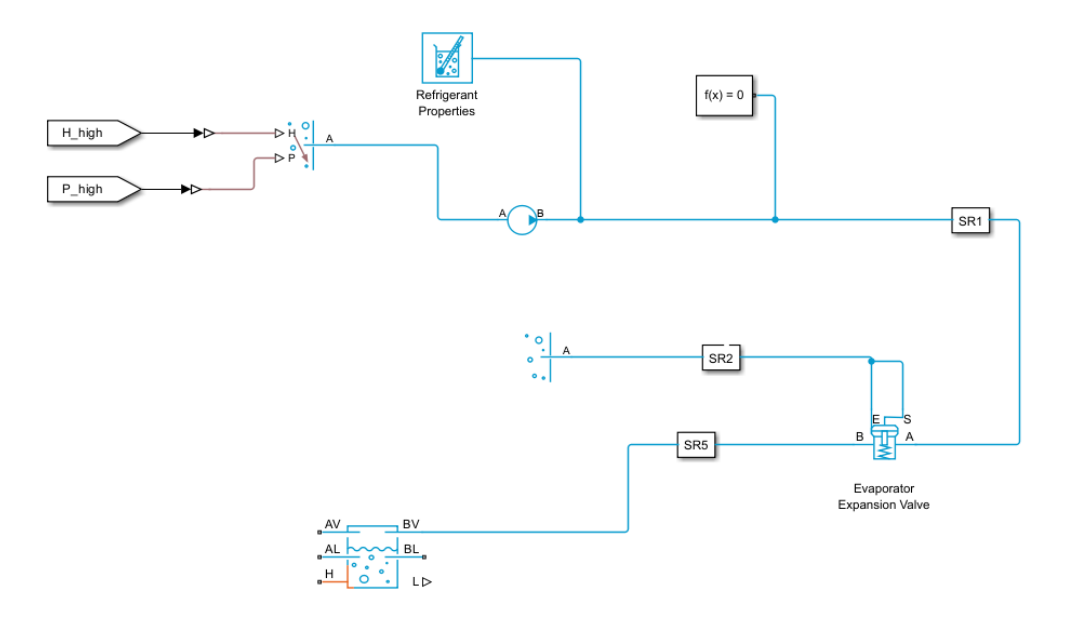


Figure 57 Expansion valve bench

An experimental simulation is conducted to investigate the pressure drop characteristics of an expansion valve. A parametric study is performed by systematically varying the three key independent variables: refrigerant mass flow rate, inlet pressure, and inlet temperature. All other boundary conditions are maintained at constant values to isolate the individual effect of each parameter on the resultant pressure drop.

Control action		
Refrigerant mass flow rate (kg/s)	mdot_r	[0.004526, 0.0062, 0.0077]

Operating conditions			
Refrigerant Pressure (MPa) P [0.9, 1.0, 1.1, 1.2]			
Refrigerant Temperature Reservoir Input (K)	тс	[300, 315, 330]	

Environment		
Pressure (MPa)	P_env	0.101325
Temperature (°C)	T_env	30
Relative Humidity (%)	RH_env	0.4
CO2 Fraction	CO2_env	4e-4

Table 3 Expansion valve bench operating variables

Effect of refrigerant mass flow rate

The following plot characterizes the relationship between the pressure drop (ΔP) and the refrigerant mass flow rate (\dot{m}_r) under constant inlet conditions of 300 K and 1.1 MPa. The data shows a strong positive correlation, with ΔP increasing from approximately 1.035 MPa to 1.065 MPa as \dot{m}_r was raised from 4.5 x 10⁻³ kg/s to 8 x 10⁻³kg/s.

This trend is consistent with fundamental fluid dynamics, because the pressure drop across a restrictive valve orifice can be approximated to be proportional to the square of the flow rate $(\Delta P \propto \dot{m}_r^2)$ for turbulent flow conditions. The observed relationship confirms that the valve's performance aligns with expected behaviour, where increasing flow rates result in higher frictional and dynamic pressure losses.

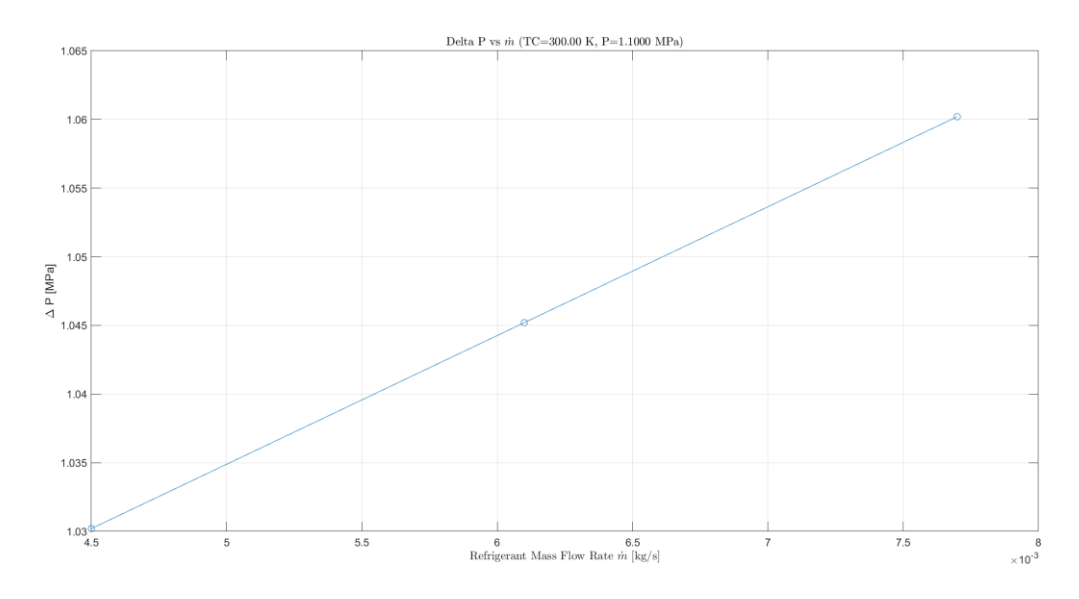


Figure 58 Expansion valve pressure drop over refrigerant mass flow rate

Effect of refrigerant inlet pressure

To isolate the effect of inlet pressure on valve performance, simulations are conducted at a constant mass flow rate of 0.0061 kg/s and a constant inlet temperature of 300 K. The data indicates that ΔP increases with higher inlet pressure due to increased fluid density at constant flow rate and temperature. An increase in inlet pressure leads to a higher fluid density at constant flow rate and temperature. As a result, a denser refrigerant flowing through a fixed valve orifice experiences increased frictional and momentum losses, causing a larger pressure drop (ΔP). This highlights that the valve's pressure drop is influenced not only by the flow rate but also by the operating pressure conditions.

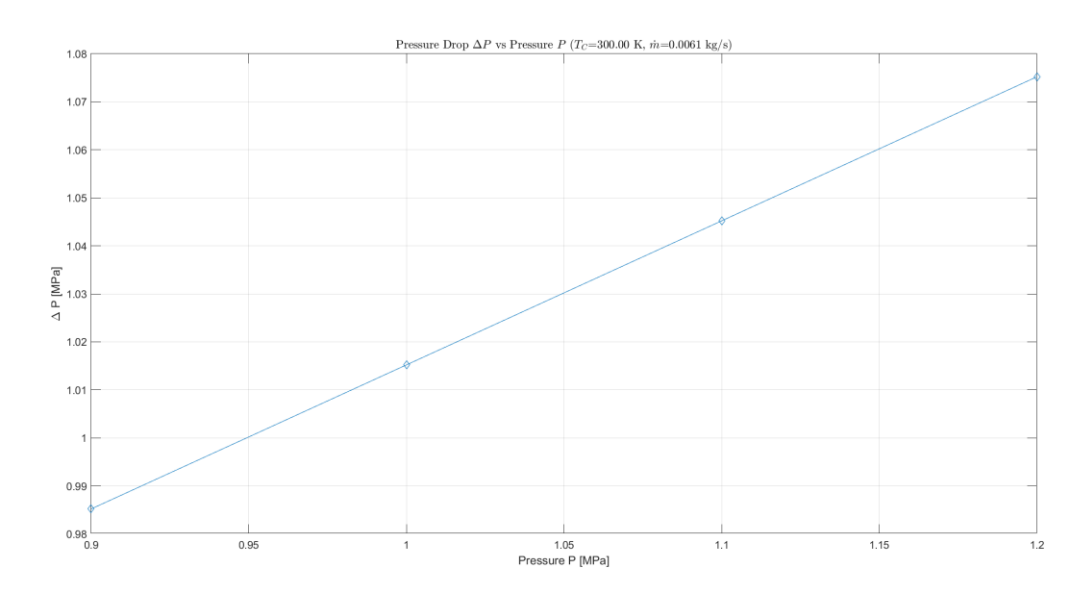


Figure 59 Expansion valve pressure drop over refrigerant inlet pressure

Effect of refrigerant inlet temperature

The results demonstrate that inlet temperature has a negligible effect on the pressure drop across the valve. Over a 30 K operational range, the pressure drop varied by less than 0.001 MPa, which is insignificant. Therefore, inlet temperature is not a critical variable for predicting pressure drop, with mass flow rate and inlet pressure being the primary influencing factors.

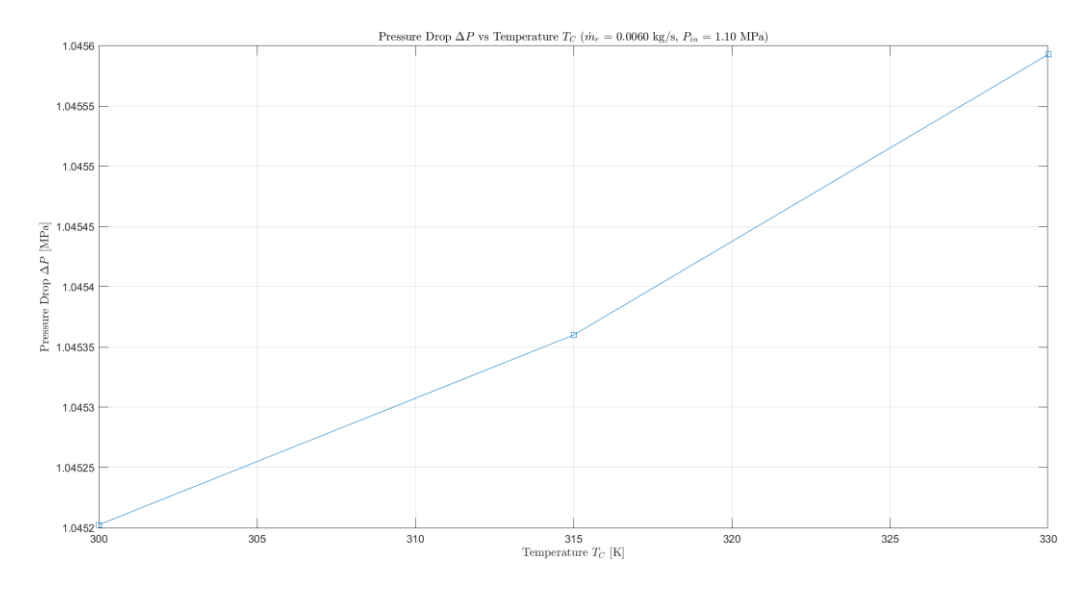


Figure 60 Expansion valve pressure drop over refrigerant inlet temperature

Then, the data are organized into a Look-Up Table (LUT) that characterizes the pressure drop (ΔP) across the expansion valve as a function of key operating parameters: refrigerant inlet temperature, inlet pressure, and mass flow rate. The LUT is structured as a three-dimensional matrix, enabling efficient interpolation between data points.

	val(:,:,1) =			
	0.9702	1.0002	1.0302	1.0602
	0.9704	1.0004	1.0304	1.0604
	0.9706	1.0006	1.0306	1.0606
	val(:,:,2) =			
$\Delta P = f(T_C, P_{in}, \dot{m}_{ref})$, , , , ,			
	0.9852	1.0152	1.0452	1.0752
	0.9854	1.0154	1.0454	1.0754
	0.9856	1.0156	1.0456	1.0756
	val(:,:,3) =			
	1.0002	1.0302	1.0602	1.0902
	1.0004	1.0304	1.0604	1.0904
	1.0006	1.0306	1.0606	1.0906

Figure 61 Expansion valve LUT

To illustrate the expansion valve's behaviour, a 3D map is created with inlet pressure and refrigerant temperature as independent variables, and the pressure drop (ΔP) on the vertical axis. Multiple surfaces represent different refrigerant mass flow rates.

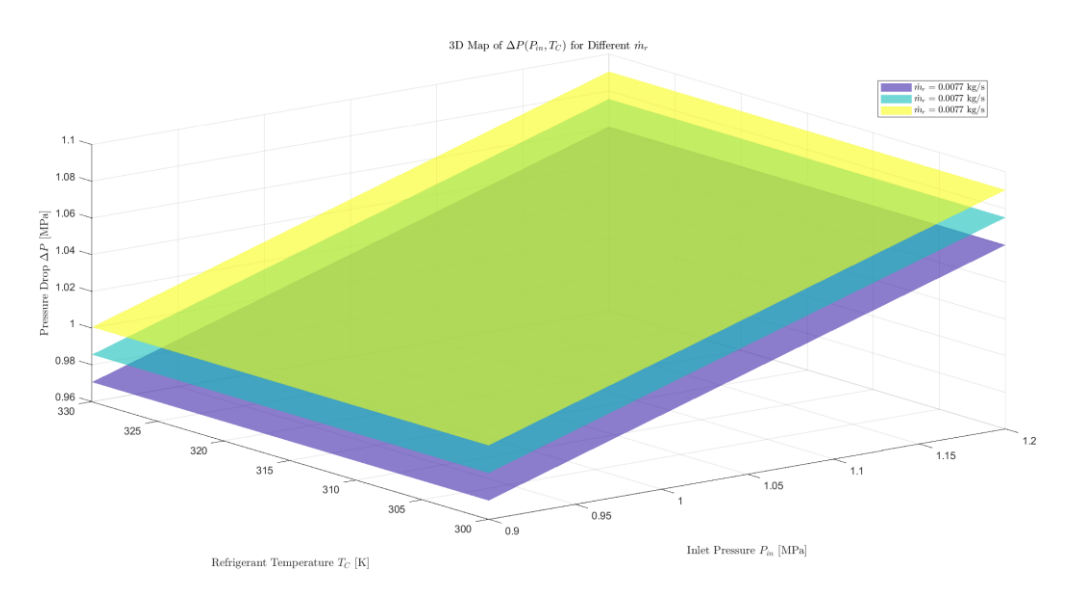


Figure 62 3D Map of $\Delta P(\textit{Pin,TC})$ for different \dot{m}_r

3.6.4 Compressor bench

The compressor's primary role is to compress the refrigerant coming from the evaporator, increasing its pressure and temperature to enable condensation and heat rejection to the vehicle's surroundings. Its performance directly affects energy efficiency, cooling capacity, and the overall reliability of the HVAC system.

A dedicated test bench is used for experimental characterization, designed to replicate realistic operating conditions and accurately evaluate key performance parameters. The setup consists of:

- An Inlet Reservoir: Defines the refrigerant suction conditions by imposing pressure and temperature at the compressor inlet. It acts as an infinite volume, ensuring stable and reproducible boundary conditions for mass flow and performance evaluation.
- A Positive Displacement Compressor: With a fixed displacement of 80 cm³/rev, it compresses the refrigerant vapor from the evaporator to higher pressure and temperature. Its performance is characterized by an isentropic efficiency of 65% and a volumetric efficiency of 90%, key parameters for determining mass flow, work, and discharge conditions based on operating speed and suction state.
- An Accumulator: Serves as a buffer volume at the compressor outlet, stabilizing pressure fluctuations and dampening pulsations generated by the compression process. It ensures smoother flow delivery to the downstream circuit, protects system components from sudden transients, and provides a more realistic representation of discharge conditions

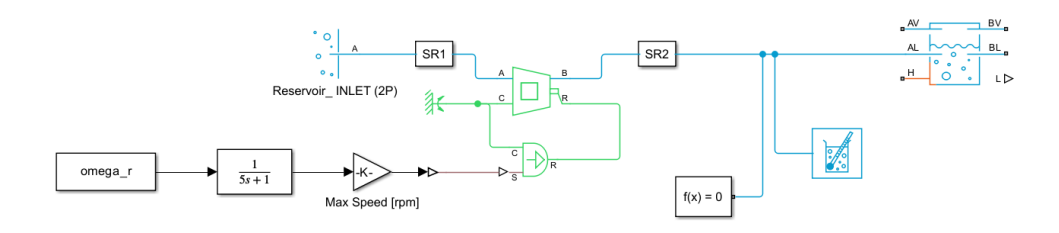


Figure 63 Compressor Bench

A parametric study is performed by systematically varying the three key independent variables: compressor speed, inlet pressure, and inlet temperature. The objective of this study is to investigate the effect of these variables on the compressor work.

Control action		
Compressor speed control (%)	omega_r	[0.3,0.6,0.8]

Operating conditions		
Refrigerant Pressure Ratio	P _{out} / P _{in}	[4.5, 5.25, 6, 8]
Refrigerant Temperature Reservoir Input (K)	TA	[250, 265, 280]

Table 4 Compressor bench operating variables

Effect of pressure ratio Pout / Pin

The following plot shows that compressor power increases monotonically with the pressure ratio P_{out}/P_{in} , displaying a slightly convex upward trend. This trend can be explained through thermodynamics, as the energy required for compression increases nonlinearly due to the combined effects of real-gas behaviour and growing system irreversibility, such as increased mechanical friction and internal leakage. Consequently, operating at elevated compression ratios result in significantly greater power consumption, highlighting the importance of optimizing the compression level for energy efficiency.

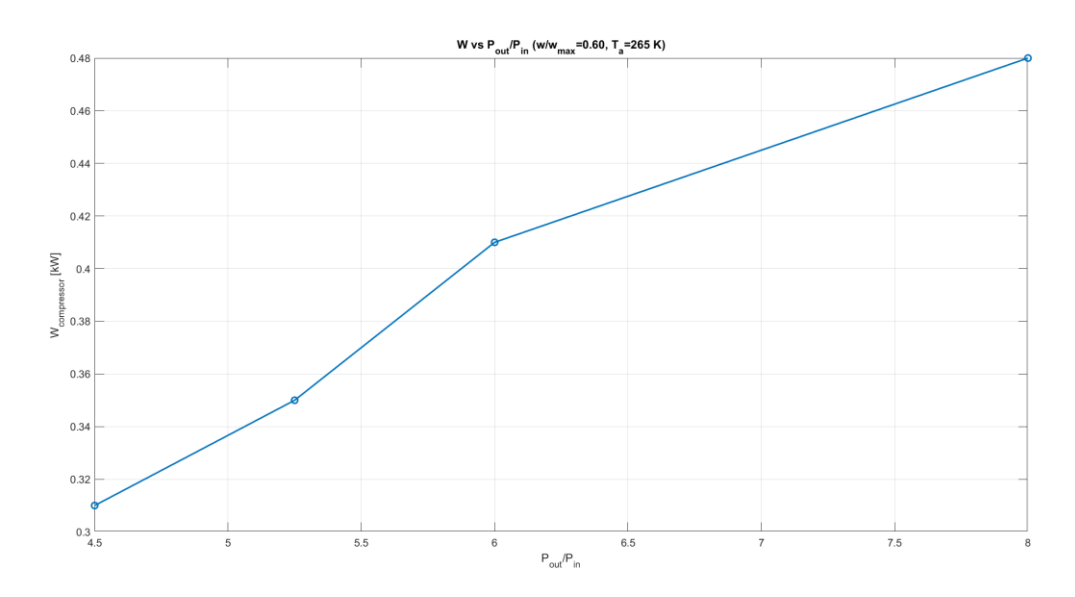


Figure 64 Compressor work over pressure ratio

Effect of Inlet Temperature

The plot shows a slight increasing trend in compressor power as the inlet temperature increases from 250 K to 280 K. This behaviour is coherent with the fundamental thermodynamic expectation that, for a fixed mass flow rate and pressure ratio, the specific compression work increases linearly with inlet temperature.

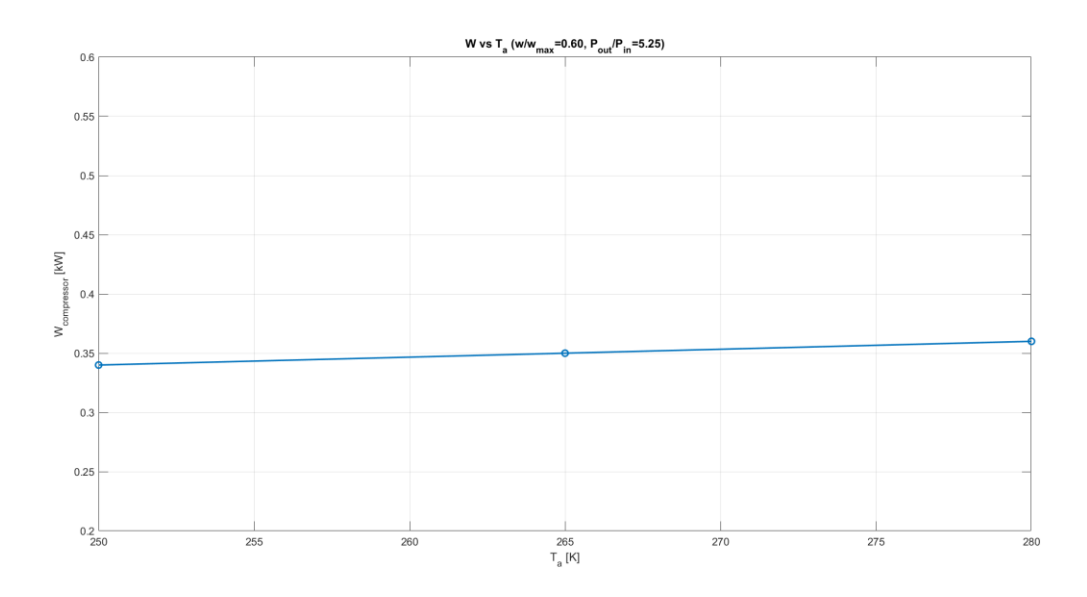


Figure 65 Compressor work over inlet temperature

Effect of Compressor speed

The graph demonstrates a strong linear correlation between compressor work and rotational speed. When speed increases from 30% to 80% of its maximum value, the compressor work rises proportionally from 0.18 kW to 0.53 kW. This linear relationship occurs because the compressor work is directly proportional to the refrigerant mass flow rate, which is controlled by the compressor speed.

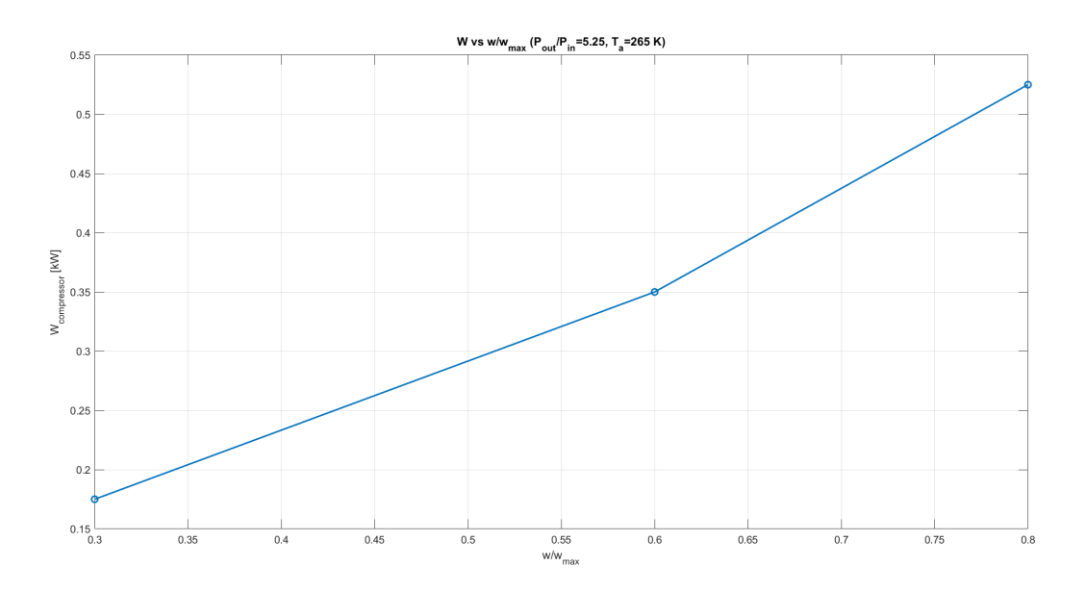


Figure 66 Compressor work over rotational speed

The experimental data are used to generate a look up table in function of compressor speed percentage, refrigerant temperature at the compressor inlet and the pressure ratio Pout/Pin.

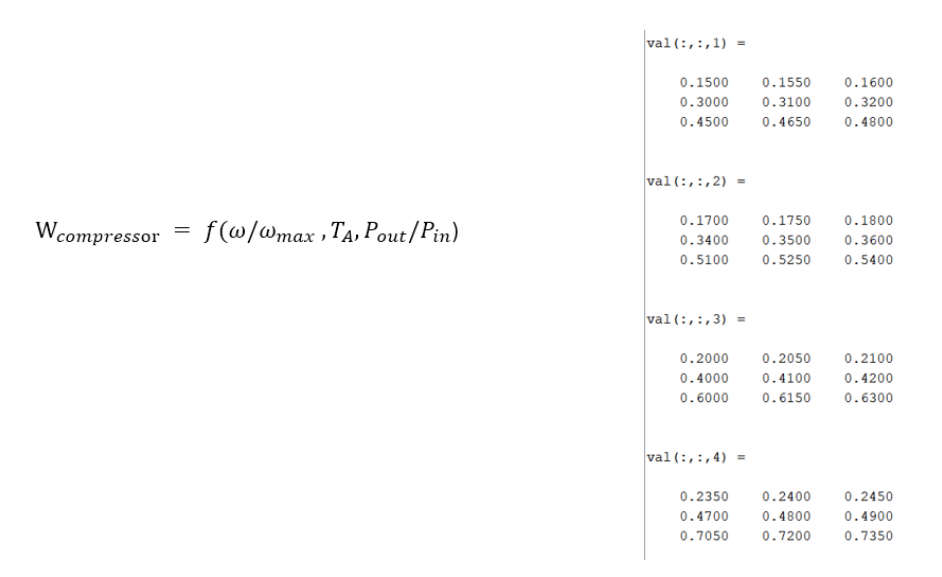


Figure 67 LUT Compressor

To better highlight the relationships among the variables, a 3D surface plot is generated.

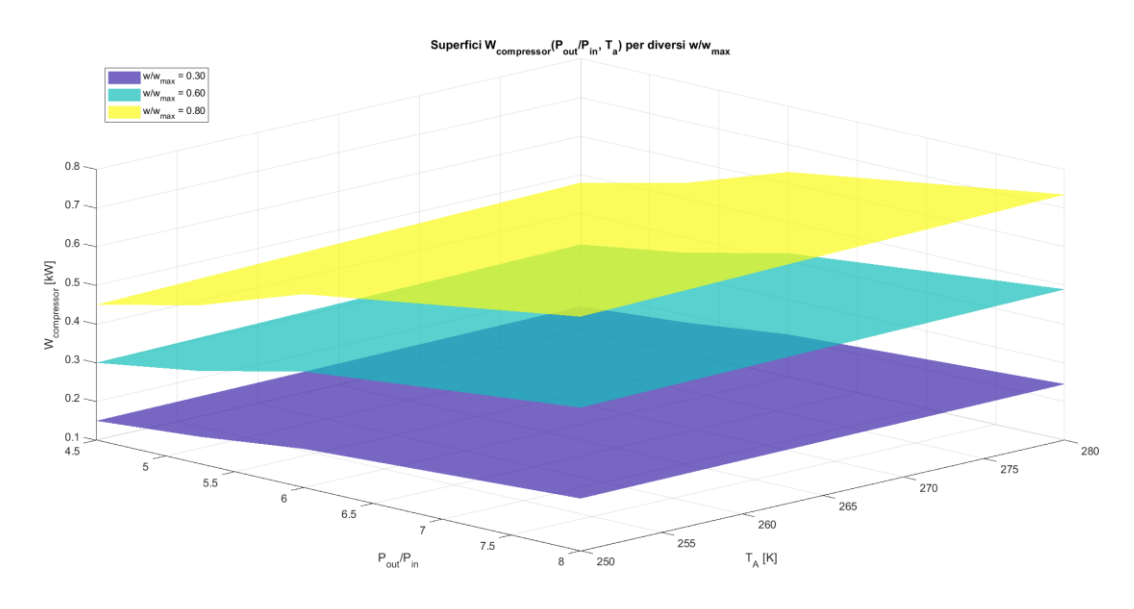


Figure 68 3D map of $W_{compressor}$ for different ω/ω_{max}

4. Neural Network-Based Modelling of Thermal Models

4.1 Methodological Approach

To accurately and efficiently predict the thermal system performance of an electric vehicle under real-world driving conditions, a data-driven approach utilizing neural networks (NNs) is implemented. This methodology provides an optimal balance between predictive accuracy and computational efficiency. Due to the complex, nonlinear behaviour of the vehicle's thermal system, which is influenced by numerous variables, the primary objective is to develop a predictive model capable of learning the intricate correlations between operational conditions, environmental factors, and the vehicle's thermal response.

The thermal system's behaviour varies significantly depending on the active operational mode. Consequently, the problem is decomposed into four distinct sub-problems, each modelled by a dedicated neural network. These four modes, and their corresponding functions, are:

- **Battery Heating**: Actively increases the temperature of the battery pack.
- Battery Cooling: Actively decreases the temperature of the battery pack.
- Cabin Heating: Modulates the temperature of the passenger compartment.
- <u>Cabin Cooling</u>: Reduces the temperature of the passenger compartment.

For each of these modes, a specific neural network is developed and trained on a dedicated subset of the complete dataset to ensure optimal performance for its specific function.

EFFEREST circuit

In the Efferest model, three main thermal circuits can be distinguished:

- the cooling circuit (in green),
- the ED cooling circuit positioned on the left (in blue),
- the battery circuit on the right (also in blue).

The overall operating principle is similar to that of the system previously analysed; however, the heating function is also explicitly represented in this configuration. During winter conditions, Pump 2 plays a particularly important role, as it allows the battery temperature to be quickly increased by means of the PTC heater.

In the event that heating of the passenger compartment is required, there is a dedicated branch that includes the heater core, which exchanges heat with the evaporator. In heat pump mode,

the latter acts as a condenser, allowing heat to be transferred to the coolant circuit and, consequently, to the passenger compartment.

The PTC heater can also be used for rapid heating of the cabin, making it particularly useful during start-up or thermal transient. Once steady state conditions are reached, its use is progressively reduced, in order to improve the overall efficiency of the system.

During summer operation, on the other hand, Pump 3 is more important, which allows the battery circuit to be reconfigured, excluding unnecessary branches and keeping only the cooling function active.

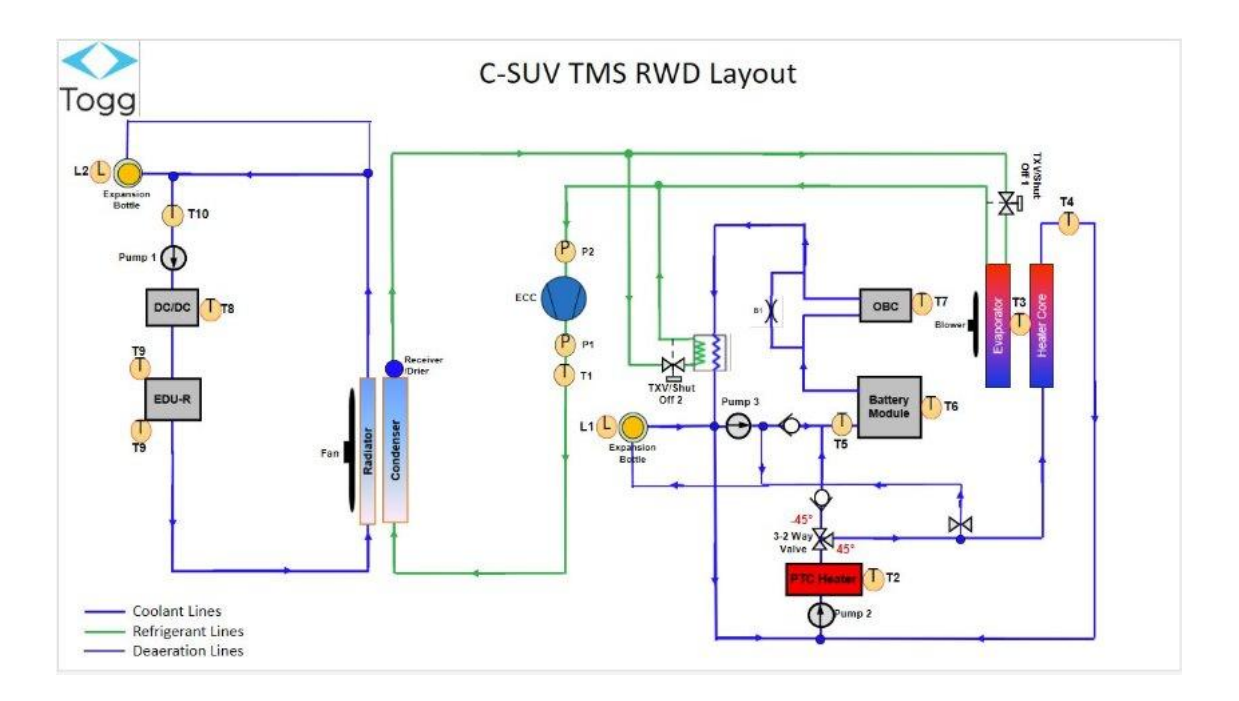


Figure 69 EFFEREST circuit model

4.2 Battery Heating mode (BH)

Problem definition

The Battery Heating mode is activated when the battery temperature falls below its optimal operating range, generally under cold ambient conditions. Proper thermal management in this mode is crucial to preserve battery efficiency, longevity, and safety.

The modelling task is divided into two related regression problems, each addressed by a dedicated neural network:

- Estimation of the battery temperature rate of change, $\frac{dTbatt}{dt}$, which captures the thermal dynamics of the battery as it responds to heating and environmental conditions.
- Prediction of the required electric heating power, P_{el} , necessary to achieve or maintain the target battery temperature.

Both networks take as input key operational and environmental features and output their respective predictions. This division allows for specialized learning focused on the distinct Physics-based phenomena governing thermal variation and power consumption.

Battery Heating Dataset - EFFEREST

The simulation datasets from the **EFFEREST** project, representing the system behaviour during the Battery Heating (BH) phase of an electric vehicle, have the variables defined below. It contains constant conditions and time-series signals sampled at 0.1 s, both used as input for training neural networks.

Initial Conditions for generating EFFEREST data

- Heat loss in the high voltage battery (Qloss_HVBattery_W = [0, 1000, 2000, 3000, 4000, 5000, 6000, 7000, 8000, 9000, 10000])
- Ambient temperature (Tambient_degC = [-20, -15, -10, -5, 0, 5, 10, 15, 20, 25, 30])
- Initial battery surface temperature (Ts_BATT_start_degC = [-20, -15, -10, -5, 0, 5, 10, 15, 20, 25, 30])

Time-Series Signals (sampled at 0.1s)

- Battery surface temperature (Ts_BATT_degC)
- On-board charger temperature (Ts_OBC_degC)
- Coolant temperature entering battery (Tco_BAT_in_degC)
- Coolant temperature exiting battery (Tco_BAT_out_degC)
- Coolant mass flow rate to battery (mdot co BAT kgps)
- Coolant mass flow rate to OBC (mdot co OBC kgps)
- PTC heater electric power (Pel_PTC_W)
- Pump 2 electric power (Pel_pump2_W)
- Thermal power delivered by PTC (Q_PTC_W)

Network Architecture and Data - Estimation of $\frac{dTbatt}{dt}$

The neural network for estimating the derivative of the battery surface temperature is a feedforward model structured as follows:

- Input Layer: 3 neurons corresponding to:
 - Ambient temperature *Tamb*
 - Battery surface temperature Thatt [Real-time battery surface temperature]
 - Battery heat loss $Q_{loss} = \{0,1000,2000,3000,4000,5000,6000,7000,8000,9000,10000\}; [W]$
- Hidden Layer 1: 8 neurons

- Activation function: Swish

Hidden Layer 2: 8 neurons

- Activation function: Swish

• Output Layer: 1 neuron

Output: estimated Pel

- Activation function: Linear

The data are sampled at a fixed time step of **0.1 seconds** (10 Hz), resulting in a total dataset size of **64,051,281 samples**, with 3 input features and one target output.

The dataset is split as follows:

- ~99.89% for training
- 0.1% for validation
- 0.01% for testing

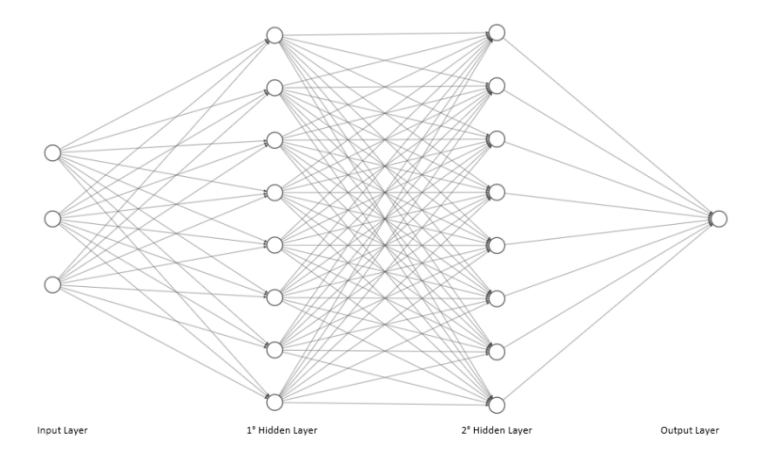


Figure 70 Neural network architecture for Battery Heating mode: estimation of dTbatt/dt

Training Configuration - Estimation of $\frac{dTbatt}{dt}$

• Batch Size: 8192

Number of Epochs: 30

• Optimizer: Adam (Adaptive Moment Estimation)

• Learning Rate: 5×10-3

• Loss Function: Mean Squared Error (MSE)

All input features are normalized to the [0,1] range prior to training.

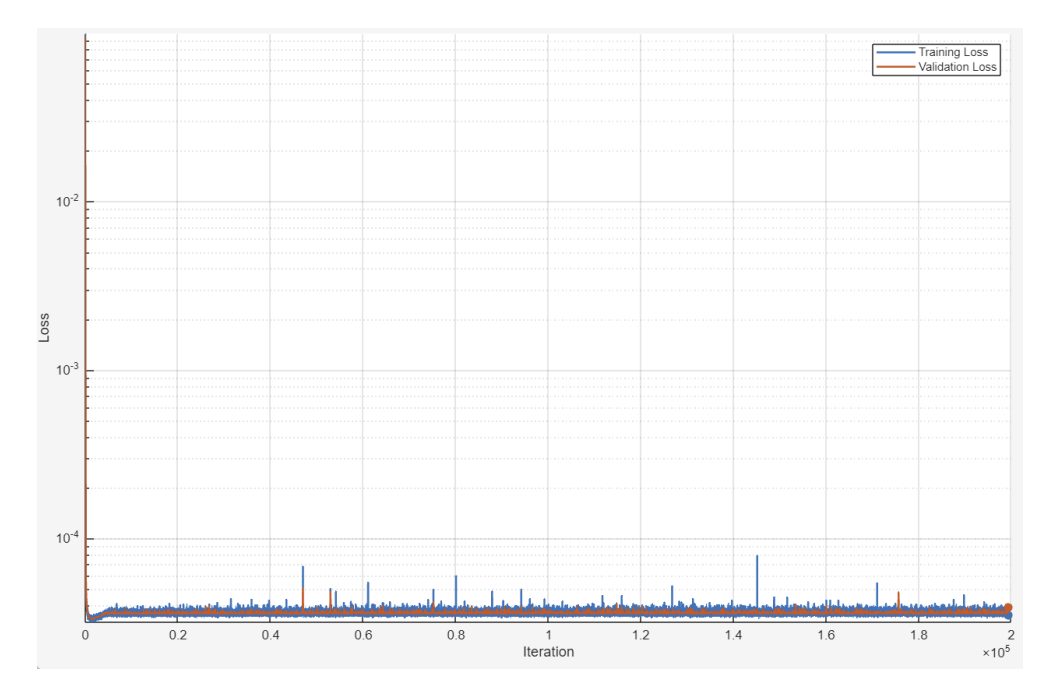


Figure 71 Training and validation loss over epochs for NN dTbatt/dt

Testing - Estimation of $\frac{dTbatt}{dt}$

The model is evaluated on a test dataset composed of samples not used during training, representing typical operating conditions of the Battery Heating mode. *Quantitative assessment* is performed using standard regression metrics, including the Root Mean Squared Error (RMSE).

$$RMSE = \sqrt{\frac{1}{N} \sum_{i=1}^{N} (Data_i - NNprediction_i)^2}$$

The model achieved an *RMSE of 0.00576*, indicating high accuracy in estimating the battery surface temperature derivative. This low RMSE value demonstrates the neural network's capability to accurately predict thermal variations of the system under realistic conditions.

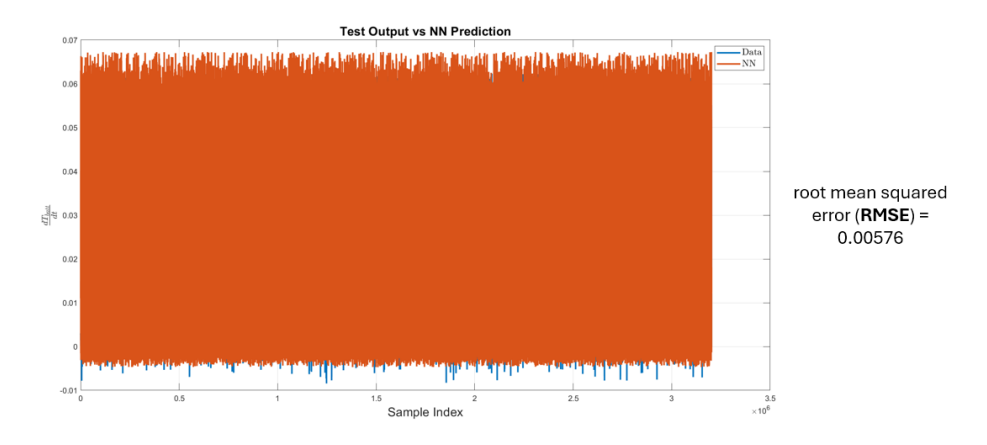


Figure 72 dTbatt/dt: Test output vs NN prediction

Qualitative analysis through plots comparing predicted versus actual values further confirms the model's good fit, with minimal deviations and no evident systematic error patterns. Residual errors may be attributed to noise in the simulation data or limitations in capturing complex thermal dynamics of the system.

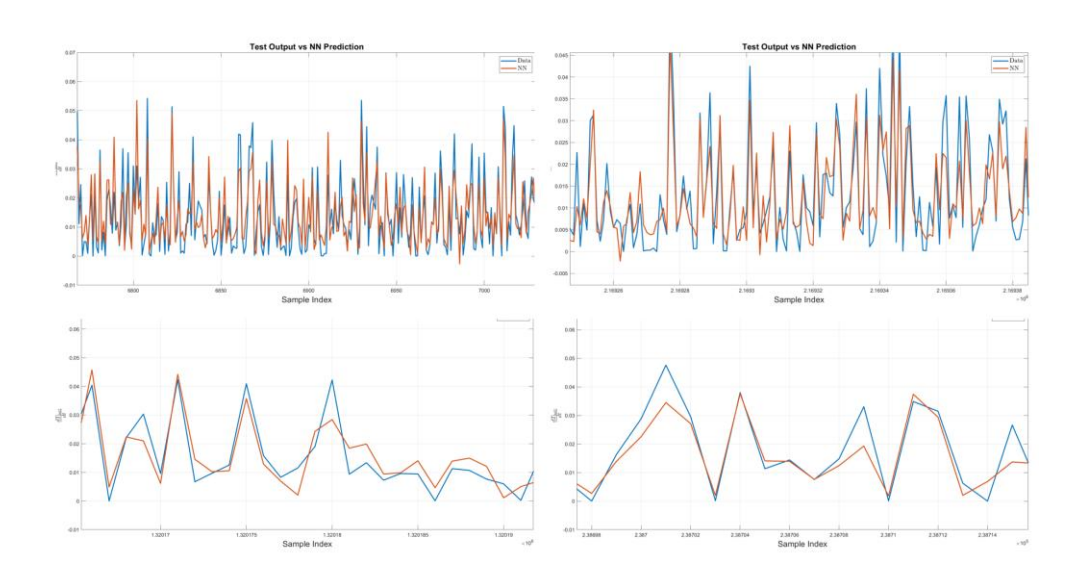


Figure 73 dTbatt/dt - qualitative analysis: Test output vs NN prediction

This architecture provides a balance between model complexity and training efficiency, enabling the network to learn the nonlinear thermal behaviour of the battery system with a compact and computationally efficient structure.

Simulation of the Neural Network – Estimation of $\frac{dTbatt}{dt}$

To rigorously assess the predictive performance of the trained neural network, a dedicated simulation framework is developed within the Simulink environment, designed to replicate the thermal behaviour of a battery system using experimental data derived from the **EFFEREST** test campaign.

The model accepts as input a representative dataset composed of:

- Ambient temperature (Tamb),
- Battery temperature (*Tbatt*),
- Heat loss (Qloss).

All input variables are first subjected to *normalization* within the [0, 1] range, using the same scaling parameters (minimum and maximum values) applied during the training phase. This preprocessing step ensures consistency between the training and inference phases and maintains the validity of the network's learned representations.

The normalized inputs are subsequently fed into the neural network, which provides as output the time derivative of the battery temperature (dTbatt/dt). This thermal gradient is then integrated over time using a numerical solver to reconstruct the temperature profile of the battery, Tbatt(t). The reconstructed profile is then compared to the experimentally measured battery temperature, enabling a quantitative evaluation of the network's predictive accuracy.

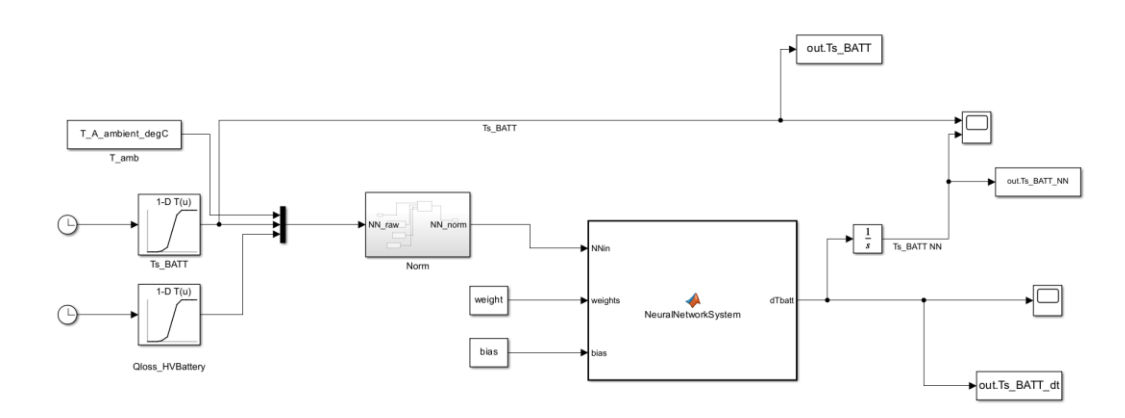


Figure 74 Simulink model for testing dTbatt/dt Neural Network

In addition to serving as a validation platform, the Simulink model is also employed to conduct a sensitivity analysis aimed at investigating the impact of solver configuration on both accuracy and computational efficiency. Specifically, the ODE solver ode4 (Runge-Kutta) is utilized in combination with varying values of the **fixed step size**. The objective of this analysis is to identify the optimal balance between numerical precision and simulation runtime.



Figure 75 Sensitivity analysis - computational time comparison

Each configuration is evaluated in terms of the **Root Mean Square Error (RMSE)** between the simulated and measured battery temperatures, as well as the **computational time** required for execution. The results of this analysis are summarized in Table 5.

Fixed step-size	Simulation time (s)	Ts_BATT (RMSE)
0,001	137.795	6.5647 °C
0,01	14.507	6.5647 °C
0,1	2.584	6.5648 °C
1	1.427	6.5651 °C
5	1.271	6.5665 °C
15	1.317	6.5632 °C

Table 5 Sensitivity analysis dTbatt/dt

A time step of **0.1 s** is determined to be the most suitable, providing a detailed representation of system dynamics without incurring excessive computational cost.

To validate the Simulink model integrated with the neural network, selected input data from the EFFEREST dataset are used. The trained neural network is used to evaluate the derivative of the battery temperature $\frac{dTbatt}{dt}$, which is plotted in the following graph.

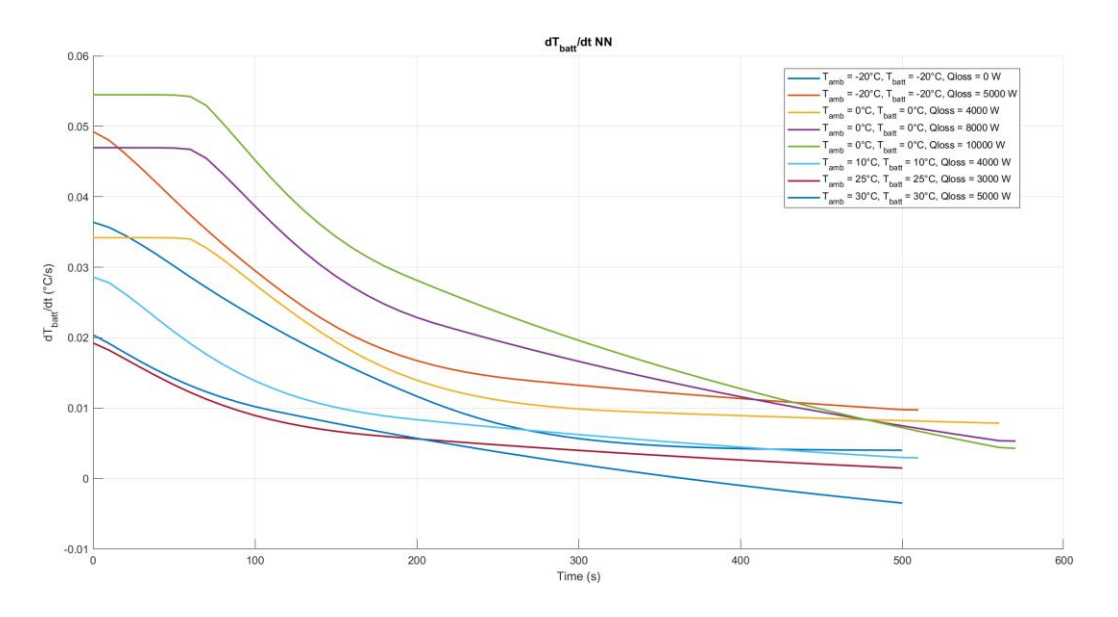


Figure 76 Derivative of the battery temperature (dTbatt/dt) over time, computed by the neural network.

This derivative is then numerically integrated to reconstruct the temperature profile, which is compared to the original data. The model's performance is evaluated using the Root Mean Square Error (RMSE), resulting in an average value of 6.50 °C.

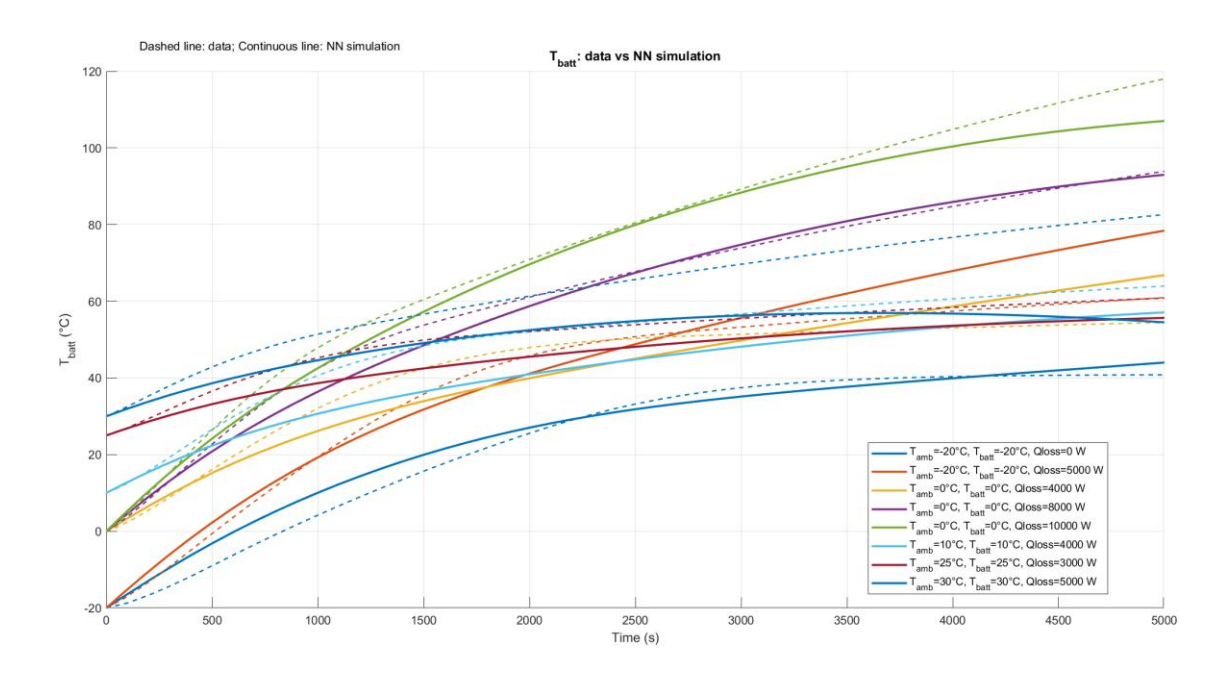


Figure 77 Battery temperature (Tbatt) over time

Network Architecture and Data - Estimation of Pel

The aim of this NN is to estimate the total electrical power consumption, defined as:

$$P_{el} = P_{el\,PTC} + P_{el\,pump2}$$

The first attempt to train the neural network for *Pel* estimation is conducted using the following architecture:

- Input Layer: 3 neurons corresponding to:
 - Ambient temperature *Tamb* [*degC*]
 - Battery surface temperature Tbatt [degC]
 - Battery heat loss Q_{loss} [W]
- Hidden Layer 1: 8 neurons
 - Activation function: Swish
- **Hidden Layer 2:** 8 neurons
 - Activation function: Swish
- Output Layer: 1 neuron
 - Output: estimated Pel
 - Activation function: *Linear*

The data are sampled at a fixed time step of **0.1 seconds** (10 Hz), resulting in a total dataset size of **64,050,000 samples**, with 3 input features and one target output.

The dataset is split as follows:

- ~99.89% for training
- **0.1%** for validation
- 0.01% for testing

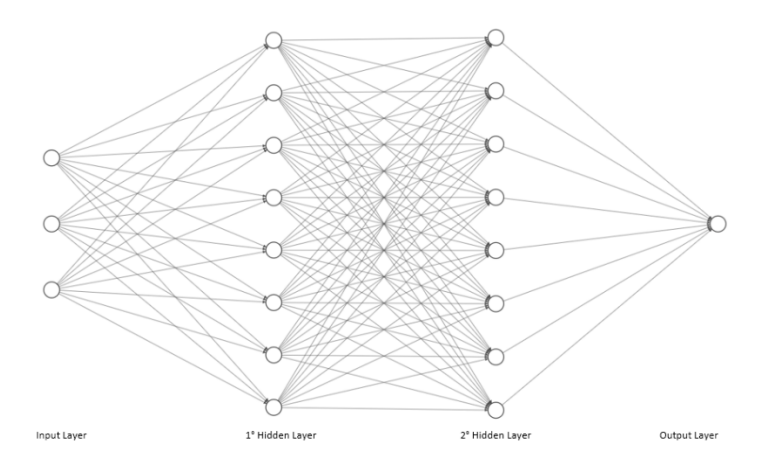


Figure 78 Neural network architecture for Battery Heating mode: estimation of Pel

Training Configuration - Estimation of Pel

• Batch Size: 8192

Number of Epochs: 30

• Optimizer: Adam (Adaptive Moment Estimation)

• Learning Rate: 5×10-3

Loss Function: Mean Squared Error (MSE)

All input features are normalized to the [0,1] range prior to training.

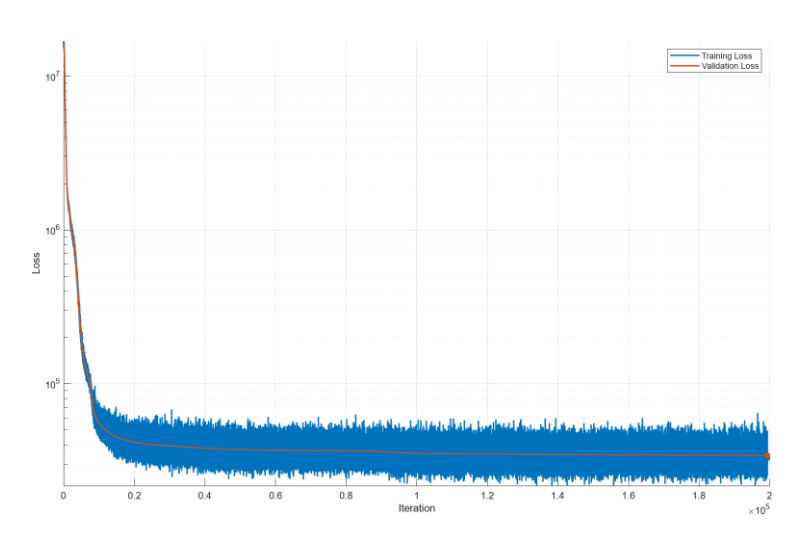


Figure 79 Training and validation loss over epochs for NN Pel

Testing - Estimation of Pel

The neural network developed for Pel estimation is evaluated on the independent test dataset. The model achieved an RMSE of 1.82×10^2 W. Considering that Pel values span up to 10,000 W, this error can be regarded as acceptable in relative terms, as it indicates that the network is generally capable of capturing the power demand dynamics.

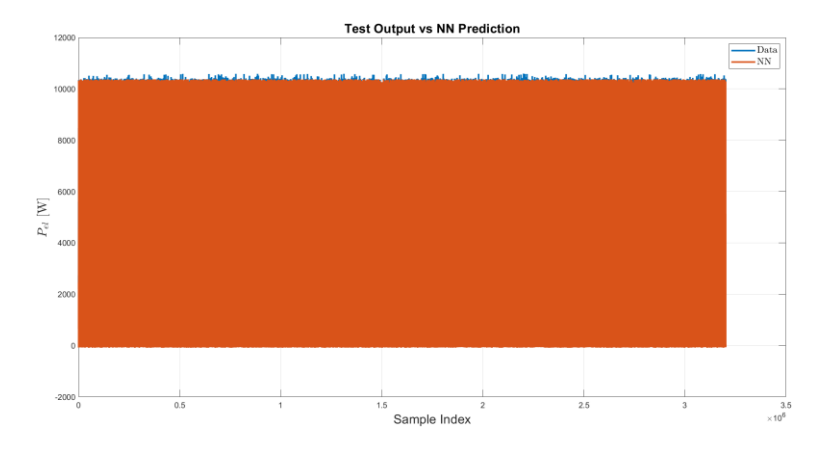


Figure 80 Pel: Test output vs NN prediction

Regarding the *qualitative analysis* on the test set, the predicted and actual *Pel* trends show an overall consistent match. Nevertheless, slight discrepancies can be observed: the predicted slopes are often steeper than the actual ones, and not all peak values are accurately captured by the network.

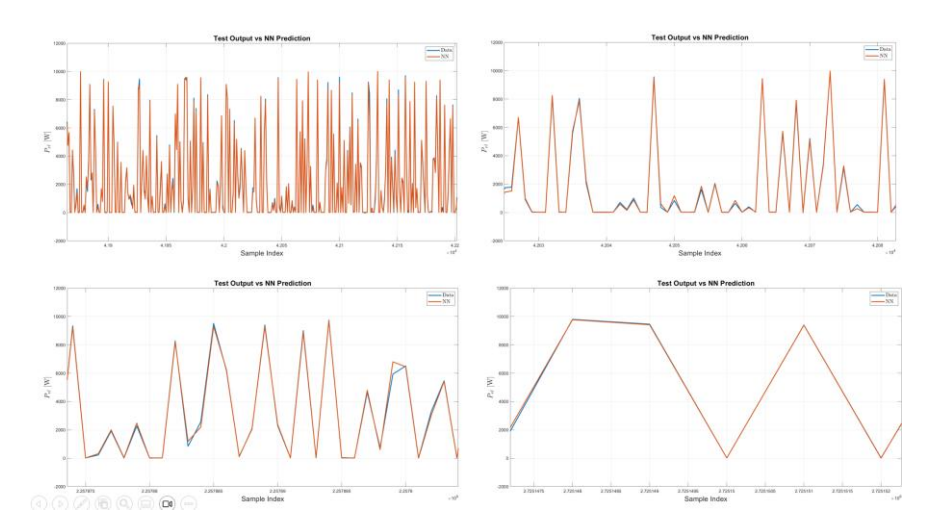


Figure 81 Pel- qualitative analysis: Test output vs NN prediction

Simulation of the Neural Network - Estimation of Pel

To evaluate the performance of the neural network, the *Pel* versus time plots must be considered. Building upon the previously developed *dTbatt/dt* simulation framework, the model is extended to include the neural network for *Pel* prediction. This network directly estimates the electrical power demand, which is then compared to the corresponding measurements from the EFFEREST dataset. The input variables are identical to those used for the *dTbatt/dt* network, ensuring consistent preprocessing and enabling a coherent assessment of the network's predictive accuracy.

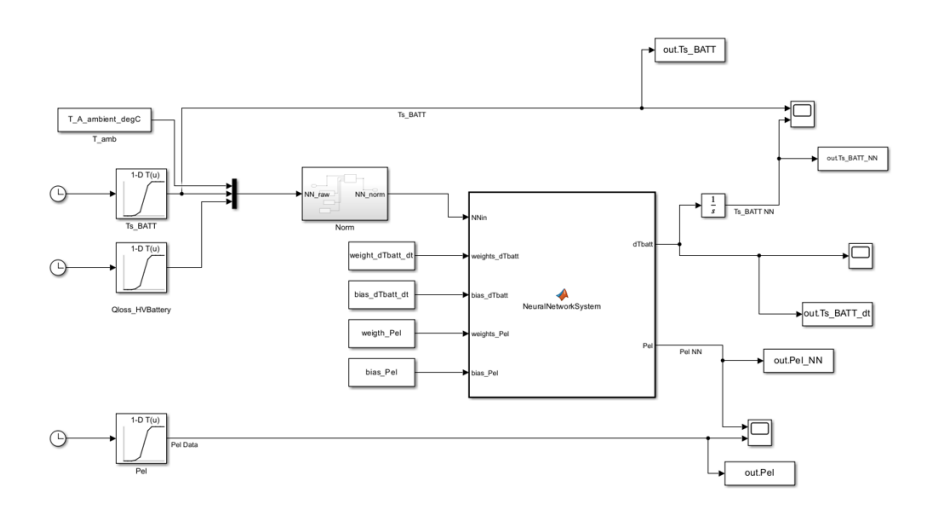


Figure 82 Simulink model for testing Pel and dTbatt/dt Neural Network

The same sensitivity analysis is also performed for the current model, with the results summarized in the following table. As in the previous case, the analysis confirms that a fixed time step of **0.1 s** provides the best compromise between numerical accuracy and computational efficiency and will therefore be adopted for all subsequent simulations.

Fixed step-size	Simulation time (s)	Ts_BATT (RMSE)	Pel (RMSE)
0,001	132.080	6.5647 °C	434.14 W
0,01	12.639	6.5647 °C	434.20 W
0,1	1.729	6.5648 °C	434.82 W
1	0.925	6.5651 °C	443.52 W
5	0.850	6.5665 °C	487.93 W
15	0.846	6.5632 °C	568.43 W

Table 6 Sensitivity analysis dTbatt/dt and Pel

Figure 83 reports the comparison between the measured EFFEREST data and the outputs of the Simulink model integrating the neural network for Pel.

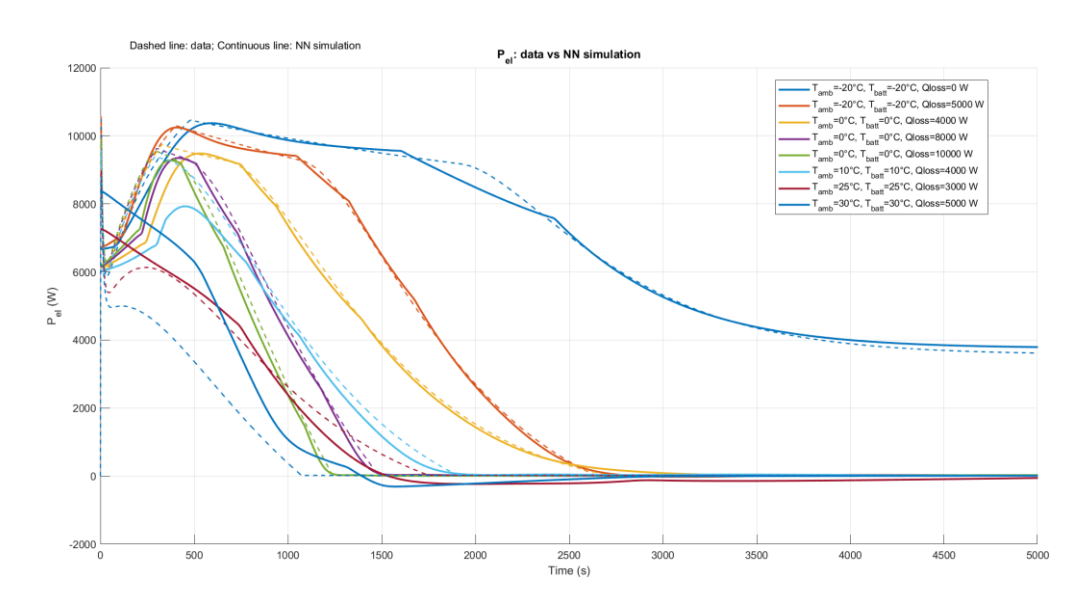


Figure 83 Electric power (Pel) over time

The measured data (dashed lines) are compared with the simulations from the Simulink model integrating the neural network (solid lines). Overall, the model correctly reproduces the dynamics of the low-temperature configurations: the predicted curves faithfully follow both the initial peak phase and the decay toward the steady-state regime, with contained deviations in magnitude and phase.

However, for the last two configurations (Tamb = 25°C and Tamb = 30°C), significant discrepancies are observed. In these cases, the simulation shows substantial errors in the magnitude of the

peaks (sometimes overestimated or not reconstructed with the same amplitude), as well as in the

slope of the curves during transient phases: the predicted response tends to have steeper slopes

and a decay with different temporal characteristics compared to the data.

Refinement of the Neural Network for Pel Prediction

Due to the limitations observed in the previously presented neural network, a refined version is

developed. While preserving the same preprocessing methodology, this updated model

introduces architectural modifications aimed at enhancing its ability to capture nonlinear system

dynamics. Specifically, an additional hidden layer is introduced, and the number of neurons per

layer is increased from 8 to 64, thus improving the network's representational capacity. The most

significant refinement, however, lies in the input set: alongside the original variables, the

previous battery temperature (Tbatt_prev), corresponding to the value recorded 10 seconds

earlier, is included to account for temporal dependencies, while the coolant temperature

difference (ΔT co = T co,BAT out – T co,BAT in) is incorporated to directly capture the thermal

exchange occurring within the cooling circuit. The new configuration is detailed below.

• Input Layer: 5 neurons corresponding to:

- Ambient temperature (Tamb)

Battery surface temperature (Ts_batt)

- Battery surface temperature 10s prior (Ts batt prev)

- Battery heat loss (Qloss)

- Temperature difference of the battery coolant (deltaT co)

• Hidden Layer 1: 64 neurons

Activation function: Swish

• **Hidden Layer 2:** 64 neurons

Activation function: Swish

• Hidden Layer 3: 64 neurons

Activation function: Swish

• Output Layer: 1 neuron

- Output: estimated Pel

Activation function: Linear

Training details:

- Batch size: 2056

Epochs: 50

- Optimizer: Adam (adaptive moment estimation)

76

Learning Rate: 5 × 10⁻³

The data are sampled at a fixed time step of **0.1 seconds** (10 Hz), resulting in a total dataset size of **63,923,181 samples**, with 5 input features and one target output.

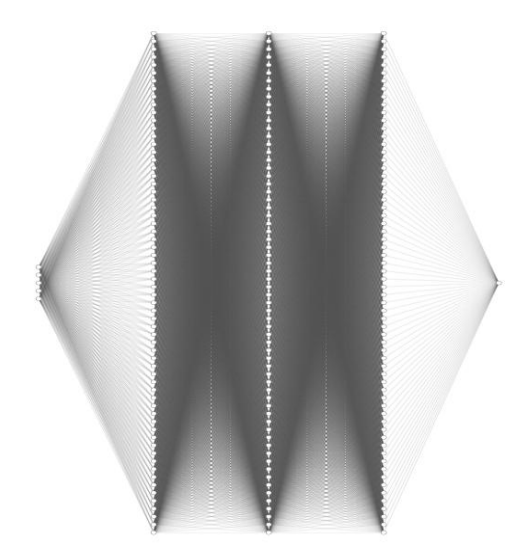


Figure 84 Neural network architecture for Battery Heating mode: estimation of Pel

The training process of the refined neural network confirmed its ability to learn the system's dynamics. Both training and validation losses exhibited a smooth, decreasing trend across epochs, converging to values on the order of log(10) without any evidence of overfitting. This convergence indicates that the prediction error is consistently minimized for both the training and validation sets, demonstrating that the model generalizes well to unseen data. The low magnitude of the final losses further supports the adequacy of the chosen architecture and input set in capturing the nonlinear relationships governing the electrical power demand.

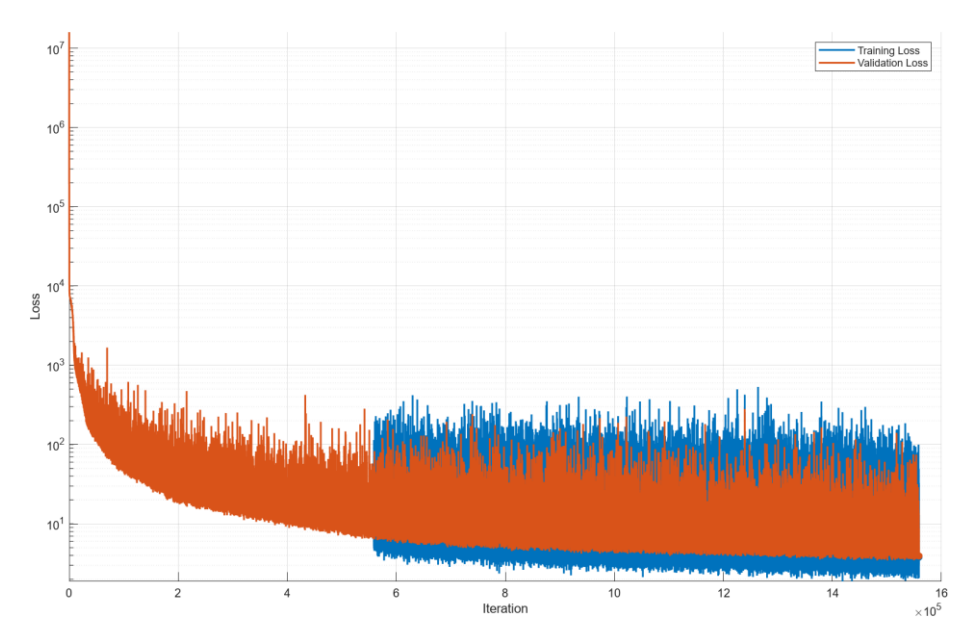


Figure 85 Training and validation loss over epochs for NN Pel

The model produces a low **RMSE of 1.96 W**, corresponding to an approximate relative error of 2–3% with respect to typical Pel values. This demonstrates that the deviations between predicted and measured values are minimal and that the network accurately reproduces the overall power demand dynamics.

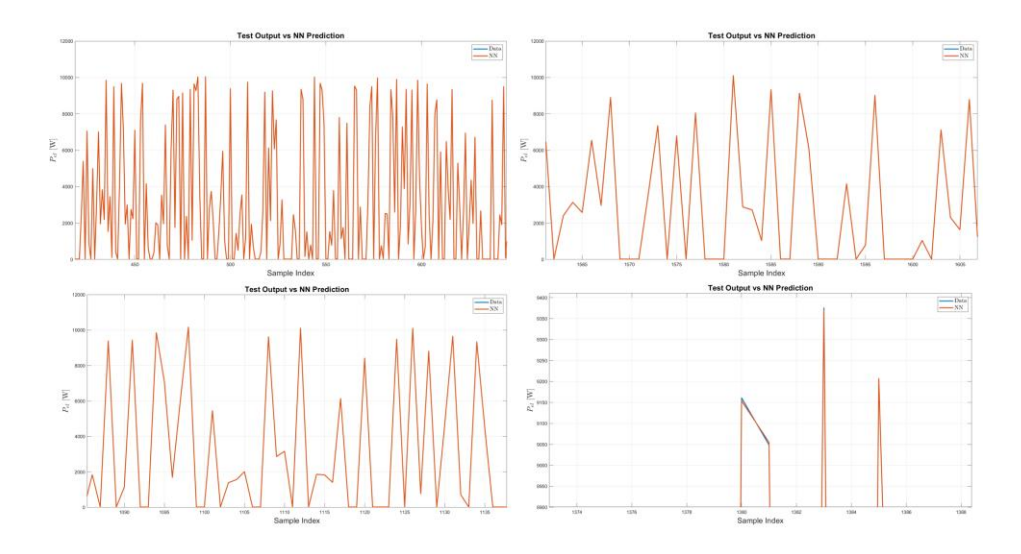


Figure 86 Pel- qualitative analysis: Test output vs NN prediction

A *qualitative comparison* between the predicted and actual *Pel* signals shows an excellent agreement, with the simulated and measured trends appearing almost identical. Deviations are minimal and hardly noticeable, indicating that the network accurately captures the system dynamics.

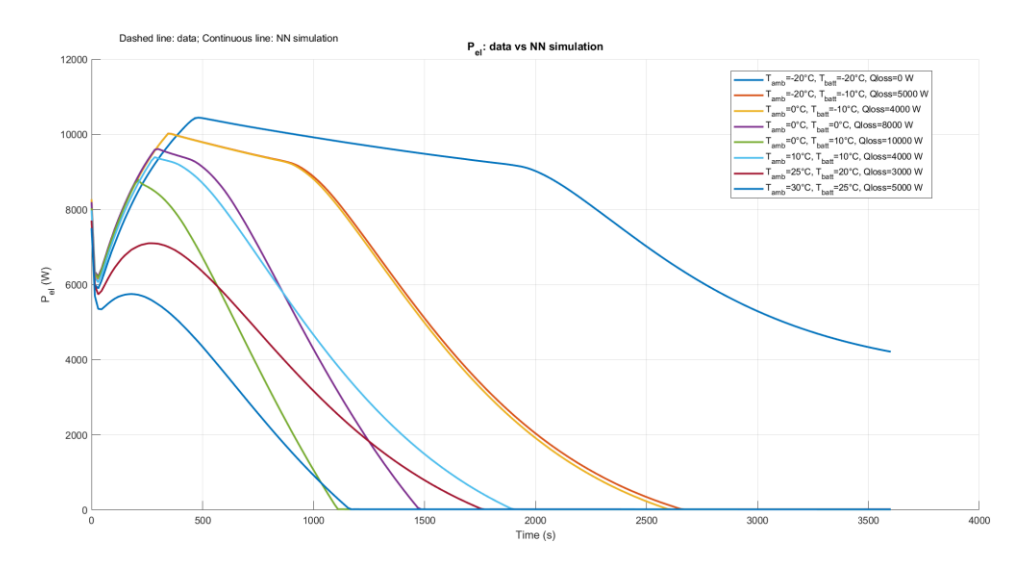


Figure 87 Electric power (Pel) over time

Applying this neural network to the same configurations as those previously tested, a significant *qualitative* improvement can be observed in the agreement between reference data and

simulations. This enhancement is *quantitatively* supported by the reduction of the root mean square error (RMSE) from **434.8 W** (Figure 83) to **2.40 W** (Figure 87Figure 87).

The following table reports the RMSE values of Pel for each of the tested curves in Simulink. All tested conditions confirm the network's ability to accurately generalize across a wide range of scenarios, consistently maintaining an average prediction error of around 2 W—equivalent to just 0.02% on a typical power value of 10,000 W.

Tamb [°C]	Tbatt [°C]	Qloss [W]	Pel RMSE (W)
-20	-20	0	3.39
-20	-10	5000	1.81
0	-10	4000	1.88
0	0	8000	2.49
0	10	10000	2.58
10	10	4000	3.53
25	20	3000	0.99
30	25	5000	2.56

Table 7 RMSE values for different simulation of Pel

4.3 Battery Cooling mode (BC)

Problem definition

The Battery Cooling mode activates when the battery temperature exceeds its optimal operating range, typically in hot ambient conditions. Proper thermal management in this mode is essential to maintain battery performance, lifespan, and safety.

The modelling task is divided into two related regression problems, each addressed by a dedicated neural network:

- Estimation of the battery temperature rate of change, $\frac{dTbatt}{dt}$.
- Prediction of the required electric heating power, P_{el} .

Battery Cooling Dataset - EFFEREST

The **EFFEREST** dataset of battery cooling has the following information:

Initial Conditions for generating data

- Heat loss in the high voltage battery (Qloss_HVBattery_W = [0, 1000, 2000, 3000, 4000, 5000, 6000, 7000, 8000, 9000, 10000])
- Ambient temperature (Tambient_degC =[40,35,30,25,20,15])
- Initial battery surface temperature (Ts_BATT_start_degC = [40,35,30,25,20,15])

Time-Series Signals (sampled at 0.1s)

- Battery surface temperature (Ts_BATT_degC)
- On-board charger temperature (Ts_OBC_degC)
- Battery coolant inlet temperature (Tco_BAT_in_degC)
- Battery coolant outlet temperature (Tco_BAT_out_degC)
- Battery coolant mass flow rate (mdot_co_BAT_kgps)
- Compressor electric power (Pel_comp_W)
- Fan electric power (Pel_Fan_W)
- Pump electric power (Pel_pump3_W)

Simulation of the Neural Network - Estimation of $\frac{dTbatt}{dt}$

To develop the neural network aimed at estimating the time derivative of the battery temperature, two simulations are performed: the first one using three input variables, and the second one using five.

Neural Network a:

- **Input Layer**: 3 neurons
 - Ambient temperature (Tamb)
 - Battery surface temperature (Ts_batt)
 - Battery heat loss (Qloss)
- Hidden layers:
 - 2 hidden layers with 8 neurons each
 - Activation function: Swish
- **Output Layer**: 1 neuron
 - $\blacksquare \frac{dTbatt}{dt}$
- Training details:
 - o Dataset: 14256396x4
 - o Batch size: 2056
 - o Epochs: 30
 - Optimizer: Adam (adaptive moment estimation)
 - Learning Rate: 5×10^{-3}

Neural Network b:

- **Input Layer**: 3 neurons
 - Ambient temperature (Tamb)
 - Battery surface temperature (Ts_batt)
 - Battery heat loss (Qloss)
- Hidden layers:
 - <u>2 hidden layers</u> with <u>64 neurons</u> each
 - Activation function: Swish
- **Output Layer**: 1 neuron
 - dTbatt
- Training details:
 - o Dataset: 14256396x4
 - o Batch size: 2056

o Epochs: 30

Optimizer: Adam (adaptive moment estimation)

Learning Rate: 5×10^{-3}

Neural Network c:

Input Layer: 3 neurons

Ambient temperature (Tamb)

Battery surface temperature (Ts_batt)

Battery heat loss (Qloss)

- Hidden layers:

2 hidden layers with 64 neurons each

• Activation function: *ReLU*

Output Layer: 1 neuron

dTbatt dt

Training details:

Dataset: 14256396x4

o Batch size: 2056

o Epochs: 30

Optimizer: Adam (adaptive moment estimation)

○ Learning Rate: 5×10^{-3}

The different neural network configurations for the estimation of $\frac{dTbatt}{dt}$ have been developed, trained, and tested entirely in the MATLAB environment, using the same criteria for splitting the dataset into training, validation, and testing described above.

In the quantitative analysis, the **Root Mean Squared Error (RMSE)** has been adopted as the main evaluation parameter, as it allows to measure the average deviation between the values predicted by the network and those measured.

During the training phase, the RMSE is calculated on the derivative of the battery temperature, $\frac{dTbatt}{dt}$ and represents the error with respect to the real derivative present in the dataset. However, in complete system simulations, the required output is the temperature of the battery itself (T_{batt}), obtained by integration of the derivative.

For this reason, an additional RMSE is calculated in the simulations that evaluates the estimated battery temperature deviation from the actual data, in order to verify the actual accuracy of the network in the dynamic context of the system.

All the results obtained from the quantitative analyses and simulations are reported in Table 8 Testing and simulation RMSE for each Battery Cooling dTbatt/dt neural network configuration, which allows a direct comparison between the tested configurations.

Configuration	Architecture	RMSE training (°C/s) dTbatt/dt	RMSE simulation (°C) Tbatt
NN a	3 inputs (Tamb, Ts_batt, Qloss) 2 hidden layers (swish) 8 neurons	2.68e-03	2.24
NN b	3 inputs (Tamb, Ts_batt, Qloss) 2 hidden layers (swish) 64 neurons	3.034e-03	1.86
NN c	3 inputs (Tamb, Ts_batt, Qloss) 2 hidden layers (ReLU) 64 neurons	2.50e-03	1.93

Table 8 Testing and simulation RMSE for each Battery Cooling dTbatt/dt neural network configuration

Afterward, a qualitative analysis is conducted to assess the accuracy of the neural network model compared to experimental data. In particular, the temporal trend of the battery temperature is observed, comparing the simulated values (solid lines) with those measured (dotted lines). From the graphs obtained, it can be seen that the simulations provided by the neural network show a linear trend over time. This behaviour can be attributed to the fact that the network has been trained to estimate the time derivative of temperature $\left(\frac{dT_{batt}}{dt}\right)$, while the complete temperature profile (T_{batt}) has been derived through a numerical integration of this derivative.

Therefore, in the absence of significant temporal variation in the estimated derivative, the model produces a nearly linear thermal response, failing to accurately reproduce the nonlinear dynamics observed in the experimental data, such as stabilization phases or slope variations related to complex thermal effects (e.g. heat exchanges with the environment, variable heat capacity, etc.). In some cases, there is a fair amount of overlap between simulation and real data, while in others the network tends to overestimate or underestimate thermal evolution. This suggests that the model, while able to capture a general trend, needs further improvement to accurately model the entire system dynamics.

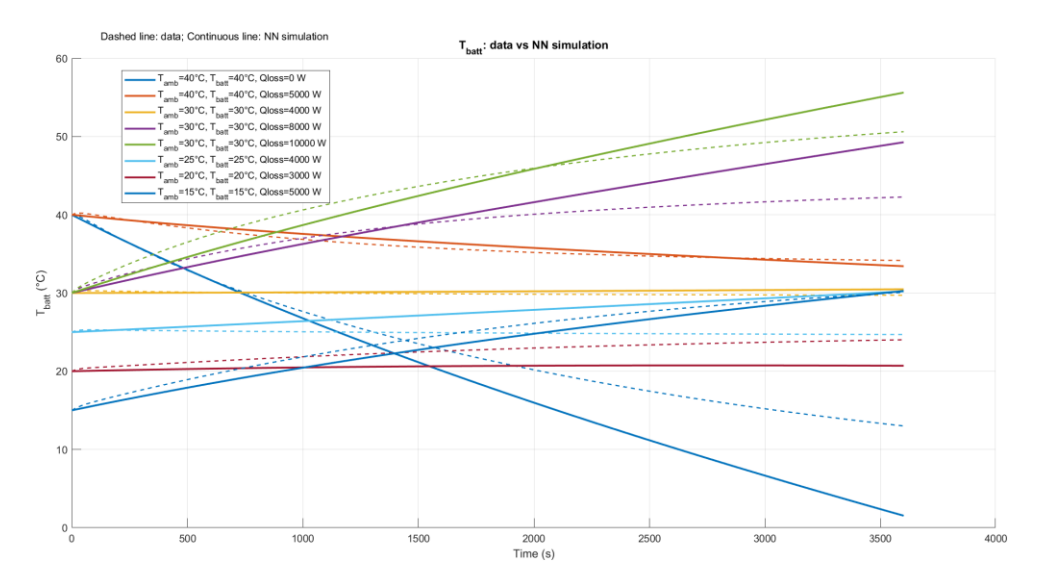


Figure 88 NN a

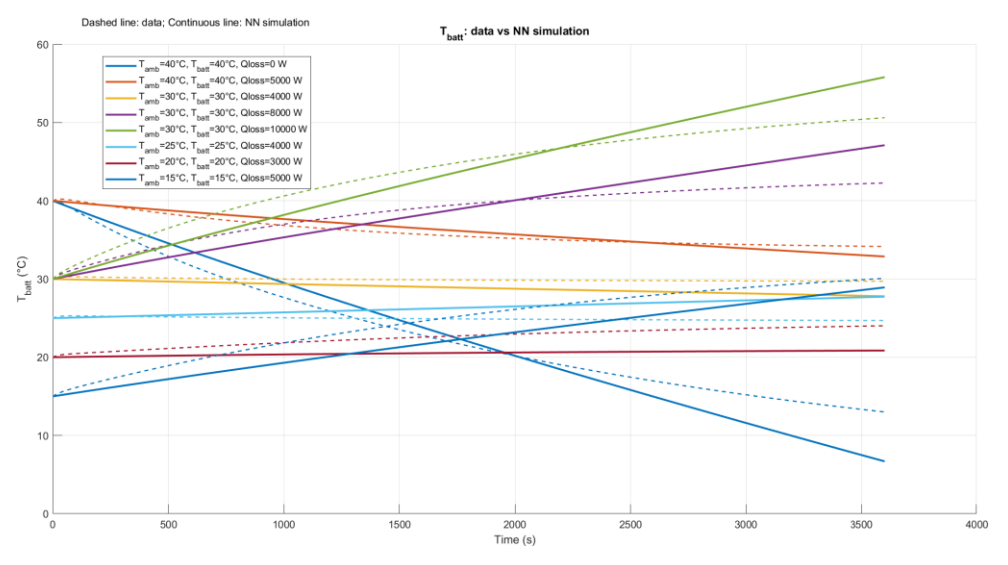


Figure 89 NN b

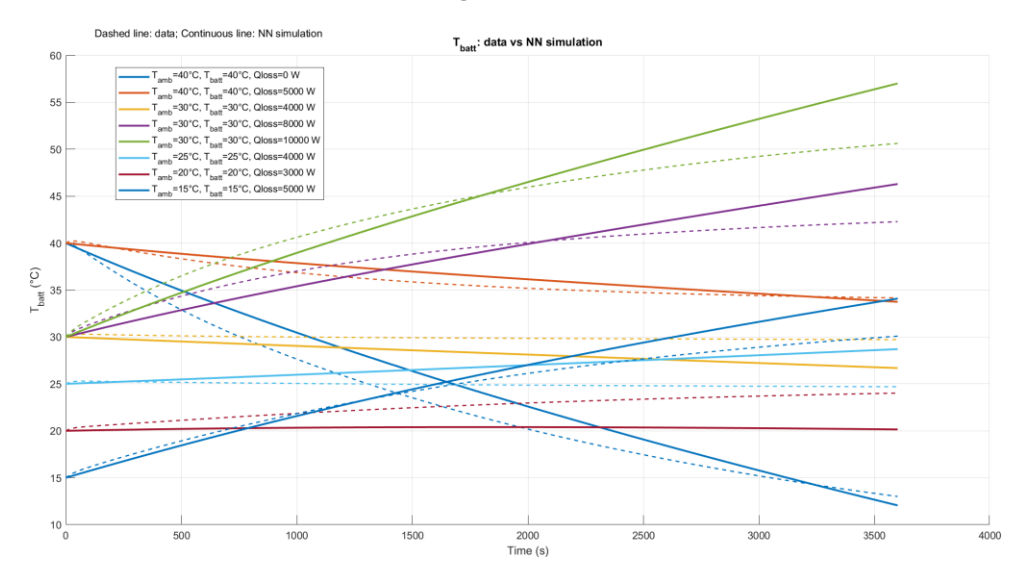


Figure 90 NN c

The analysis of the results shows that an increase in the number of neurons in the hidden layers leads to a significant qualitative improvement in the performance of the neural network. In particular, comparing the **NN** a and **NN** b models, both characterized by the same structure and activation function (Swish), but with 8 and 64 neurons respectively, a significant reduction in error is observed on the battery temperature simulation, which goes from 2.24 °C to 1.86 °C. This suggests that a greater expressive capacity of the network, obtained by increasing the number of neurons, allows a better approximation of the complex thermal dynamics of the system.

Furthermore, comparing **NN b** and **NN c**, which share the same structure and number of neurons but differ in activation function (*Swish* vs *ReLU*), it is noted that the *Swish* function provides superior performance. Specifically, **NN b** (*Swish*) achieves a lower simulation RMSE than **NN c** (*ReLU*), at 1.86 °C and 1.93 °C, respectively. This confirms that *Swish* is more effective for non-linear thermal modelling, thanks to its smooth, non-monotonic nature

Model selection and performance validation

After selecting the **NN b** neural network, which provided the best accuracy and generalization ability, a detailed analysis of the training and testing phases is carried out.

As it can be seen from the graph, the simulation reached 2.1×10^5 iterations, allowing for very stable training and validation losses at extremely low values, around 10^{-5} . This indicates that the network has effectively learned the target function without significant overfitting. However, there are sporadic spikes that may be due to data noise or momentary jitters, but do not affect training stability or convergence.

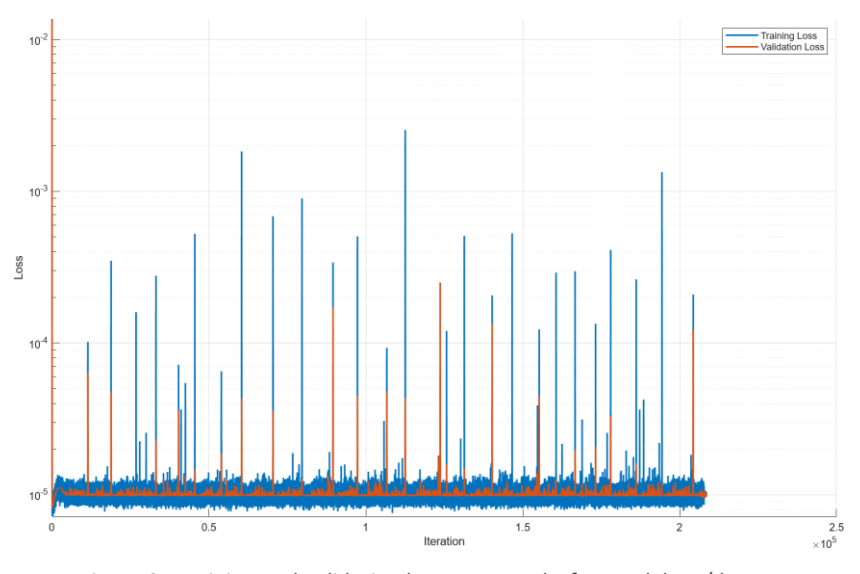


Figure 91 Training and validation loss over epochs for NN dTbatt/dt

The neural network is subsequently tested on previously unseen data to evaluate its predictive capabilities. As shown in the graph, while the predicted output (orange line) does not perfectly follow the reference data (blue line), it still captures the overall trend with reasonable accuracy. This indicates that the model retains acceptable generalization performance, even under new operating conditions.

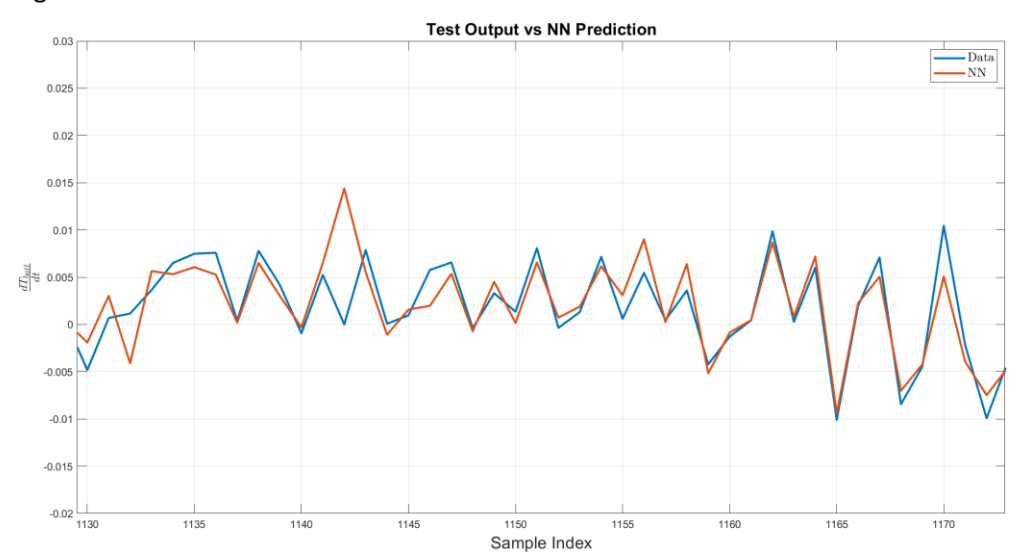


Figure 92 dTbatt/dt - qualitative analysis: Test output vs NN prediction

Network Architecture and Data - Estimation of Pel

To develop a neural network capable of accurately estimating the required electric cooling power (Pel), numerous modelling attempts are carried out.

The target variable Pel is defined as the total electric power used by the cooling system, calculated as the sum of:

$$P_{el} = P_{el\ comp} + P_{el\ Fan} + P_{el\ pump3}$$

Different combinations of input features are tested alongside varied neural network architectures, creating multiple model configurations:

Neural Network A:

- **Input Layer**: 3 neurons
 - Ambient temperature (Tamb)
 - Battery surface temperature (Ts_batt)
 - Battery heat loss (Qloss)
- Hidden layers:
 - 2 hidden layers with 8 neurons each
 - Activation function: Swish
- Output Layer: 1 neuron
 - Electric power (Pel)
- Training details:
 - o Dataset: 14256396x4
 - o Batch size: 2056
 - o Epochs: 30
 - Optimizer: Adam (adaptive moment estimation)
 - Learning Rate: 5×10^{-3}

• Neural Network B:

- **Input Layer**: 3 neurons
 - Ambient temperature (Tamb)
 - Battery surface temperature (Ts_batt)
 - Battery heat loss (Qloss)
- Hidden layers:
 - <u>2 hidden layers</u> with <u>64 neurons</u> each

- Activation function: <u>Swish</u>
- Output Layer: 1 neuron
 - Electric power (Pel)
- <u>Training details</u>:
 - o Dataset: 14256396x4
 - o Batch size: 2056
 - o Epochs: 30
 - o Optimizer: Adam (adaptive moment estimation)
 - Learning Rate: 5×10^{-3}
- Neural Network C:
 - **Input Layer**: 3 neurons
 - Ambient temperature (Tamb)
 - Battery surface temperature (Ts_batt)
 - Battery heat loss (Qloss)
 - Hidden layers:
 - <u>2 hidden layers</u> with <u>64 neurons</u> each
 - Activation function: *ReLU*
 - Output Layer: 1 neuron
 - Electric power (Pel)
 - Training details:
 - o Dataset: 14256396x4
 - o Batch size: 2056
 - o Epochs: 30
 - o Optimizer: Adam (adaptive moment estimation)
 - Learning Rate: 5×10^{-3}
- Neural Network D:
 - **Input Layer**: 4 neurons
 - Ambient temperature (Tamb)
 - Battery surface temperature (Ts_batt)
 - Battery surface temperature 10s prior (Ts batt prev)
 - Battery heat loss (Qloss)
 - Hidden layers:
 - <u>2 hidden layers</u> with <u>64 neurons</u> each
 - Activation function: Swish
 - Output Layer: 1 neuron

- Electric power (Pel)
- Training details:

o Dataset: 14216796 x 5

o Batch size: 2056

o Epochs: 30

Optimizer: Adam (adaptive moment estimation)

○ Learning Rate: 5×10^{-3}

• Neural Network E:

- Input Layer: 4 neurons
 - Ambient temperature (Tamb)
 - Battery surface temperature (Ts_batt)
 - Battery surface temperature10s prior (Ts_batt_prev)
 - Battery heat loss (Qloss)
- Hidden layers:
 - 3 hidden layers with 64 neurons each
 - Activation function: Swish
- Output Layer: 1 neuron
 - Electric power (Pel)
- <u>Training details</u>:

o Dataset: 14216796 x 5

o Batch size: 2056

o Epochs: 30

o Optimizer: Adam (adaptive moment estimation)

○ Learning Rate: 5×10^{-3}

Neural Network F:

- **Input Layer**: 4 neurons

Ambient temperature (Tamb)

Battery surface temperature (Ts_batt)

Battery surface temperature10s prior (Ts_batt_prev)

Battery heat loss (Qloss)

- Hidden layers:
 - 3 hidden layers with 256 neurons each

• Activation function: <u>Swish</u>

- Output Layer: 1 neuron

Electric power (Pel)

- <u>Training details</u>:

o Dataset: 14216796 x 5

o Batch size: 2056

o Epochs: 50

o Optimizer: Adam (adaptive moment estimation)

○ Learning Rate: 5×10^{-3}

Neural Network G:

Input Layer: 5 neurons

- Ambient temperature (Tamb)
- Battery surface temperature (Ts_batt)
- Battery surface temperature10s prior (Ts_batt_prev)
- Battery heat loss (Qloss)
- Battery coolant mass flow rate (mdot_co)

- Hidden layers:

- 3 hidden layers with 64 neurons each
- Activation function: **Swish**
- Output Layer: 1 neuron
 - Electric power (Pel)

Training details:

o Dataset: 14216796 x 6

o Batch size: 2048

o Epochs: 50

Optimizer: Adam (adaptive moment estimation)

○ Learning Rate: 5×10^{-3}

Neural Network H:

- **Input Layer**: 5 neurons

- Ambient temperature (Tamb)
- Battery surface temperature (Ts_batt)
- Battery surface temperature10s prior (Ts_batt_prev)
- Battery heat loss (Qloss)
- Temperature difference of the battery coolant (deltaT_co)

- Hidden layers:

3 hidden layers with 64 neurons each

Activation function: Swish

Output Layer: 1 neuron

Electric power (Pel)

- Training details:

o Dataset: 14216796 x 6

o Batch size: 2048

o Epochs: 50

Optimizer: Adam (adaptive moment estimation)

○ Learning Rate: 5×10^{-3}

All neural network configurations are developed and trained in MATLAB, using the previously defined data splits for training, validation, and testing. The Root Mean Squared Error (RMSE) is adopted as the primary performance metric, as it quantifies the average deviation between the predicted and measured values of Pel. A first evaluation is conducted over the entire test dataset to produce a global RMSE value for each configuration, ensuring that all models are compared under the same statistical conditions. However, while this global RMSE offers a valuable measure of accuracy, it does not fully capture the ability of the models to reproduce the temporal dynamics of Pel in realistic operating scenarios. To address this, a qualitative assessment is also carried out by selecting representative time sequences from the dataset and comparing the predicted and measured Pel profiles. For each sequence, the RMSE is calculated and then averaged to obtain the "RMSE simulation," which emphasizes the capability of the networks to track rapid fluctuations and transient behaviours. The results of both evaluations are summarized in Table 9, where for each configuration the global and qualitative RMSE values are reported side by side to facilitate direct comparison.

Configuration	Architecture	RMSE training (W)	RMSE simulation (W)
NN A	3 inputs (Tamb, Ts_batt, Qloss) 2 hidden layers (swish) 8 neurons	461.65	390.60
NN B	3 inputs (Tamb, Ts_batt, Qloss) 2 hidden layers (swish) 64 neurons	437.52	362.25
NN C	3 inputs (Tamb, Ts_batt, Qloss) 2 hidden layers (ReLU) 64 neurons	488.57	467.83

NN D	4 inputs (Tamb, Ts_batt, Ts_batt_prev, Qloss) 2 hidden layers (swish) 64 neurons	431.87	340.39
NN E	4 inputs (Tamb, Ts_batt, Ts_batt_prev, Qloss) 3 hidden layers (swish) 64 neurons	416.22	308.76
NN F	4 inputs (Tamb, Ts_batt, Ts_batt_prev, Qloss) 3 hidden layers (swish) 256 neurons	411.60	304.95
NN G	5 inputs (Tamb, Ts_batt, Ts_batt_prev, Qloss, mdot_co) 3 hidden layers (swish) 64 neurons	97.92	62.30
NN H	5 inputs (Tamb, Ts_batt, Ts_batt_prev, Qloss, deltaT_co) 3 hidden layers (swish) 64 neurons	20.45	20.98

Table 9 Testing and simulation RMSE for each Battery Cooling Pel neural network configuration

Complementing these numerical results, Figure 93 - Figure 100 display the time histories of *Pel* for the selected sequences, overlaying predicted and measured values to allow a visual assessment of model accuracy and dynamic tracking performance, thereby highlighting the strengths and limitations of each network architecture.

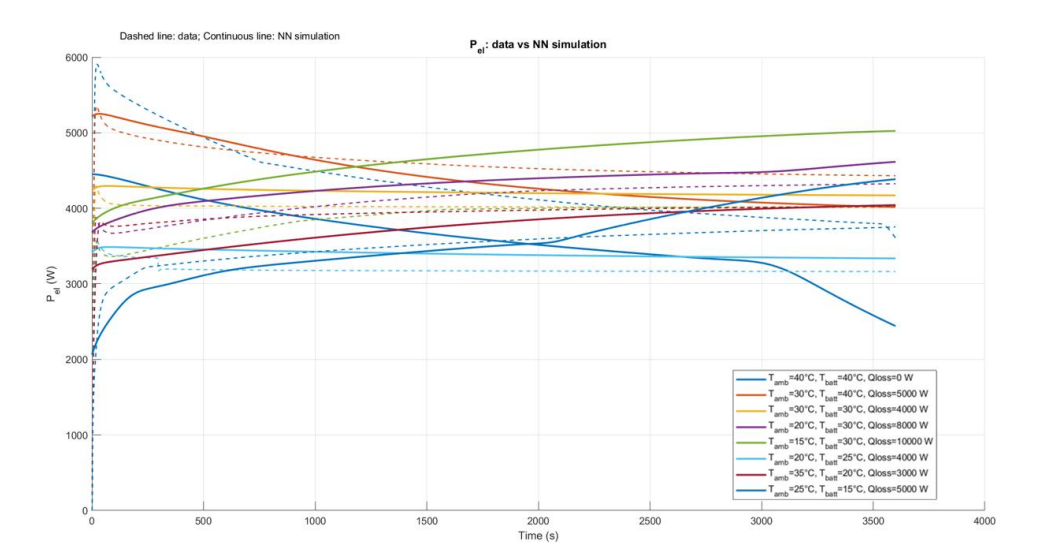


Figure 93 NN A

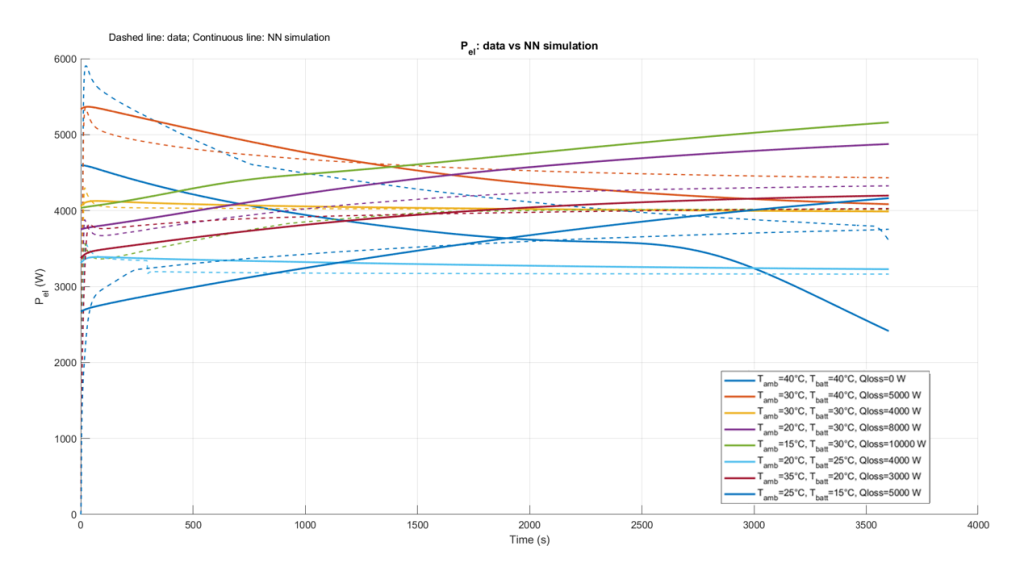


Figure 94 NN B

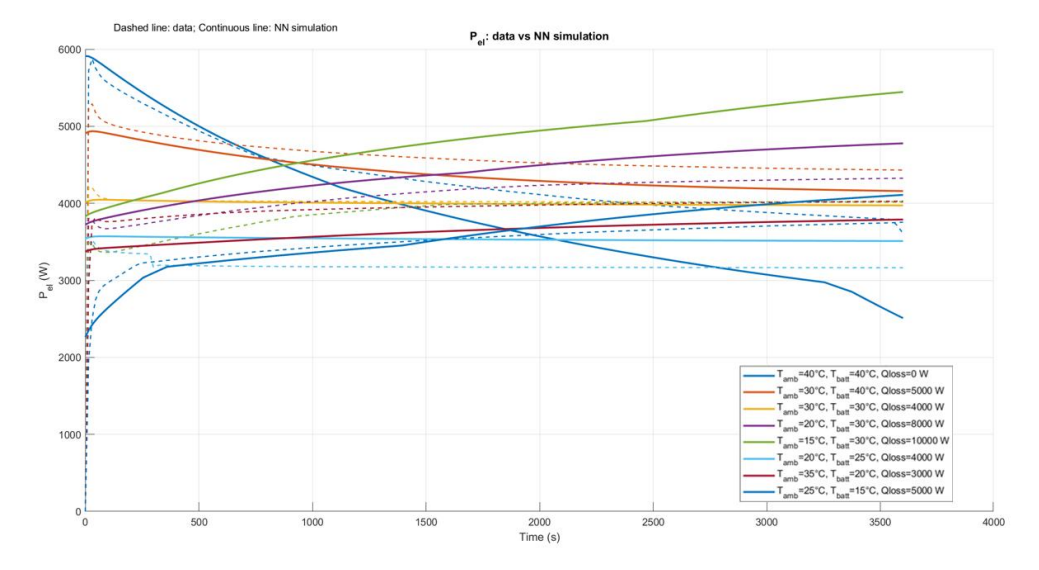


Figure 95 NN C

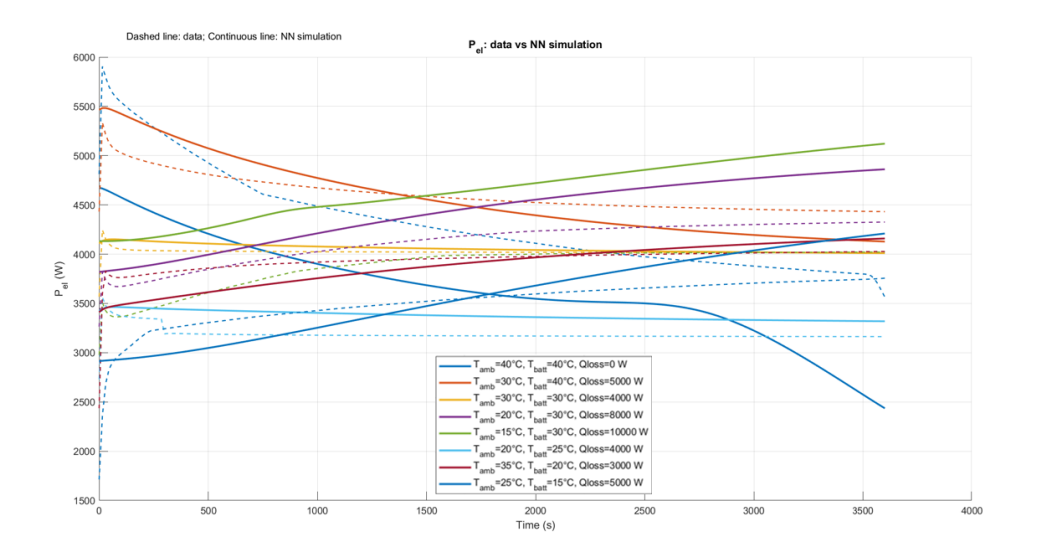


Figure 96 NN D

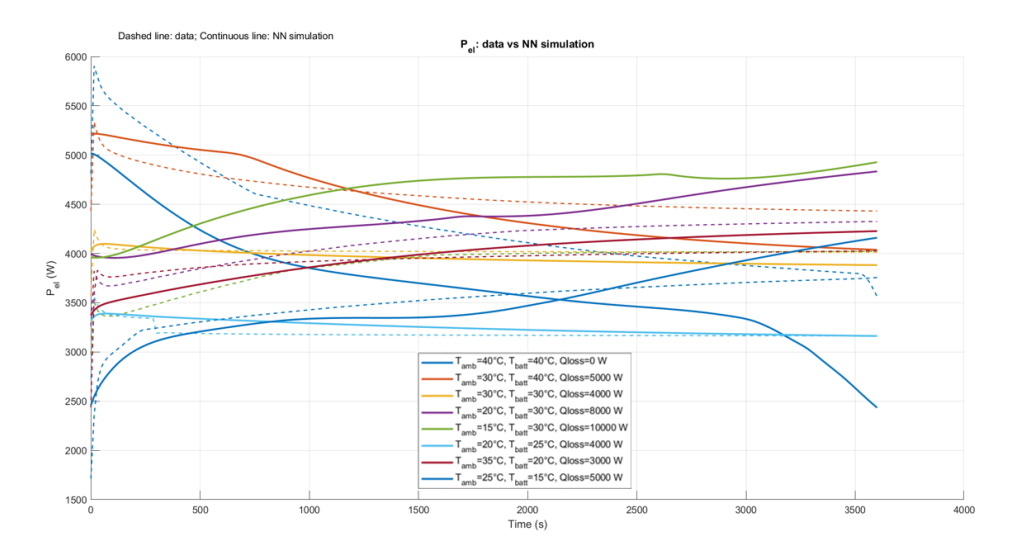


Figure 97 NN E

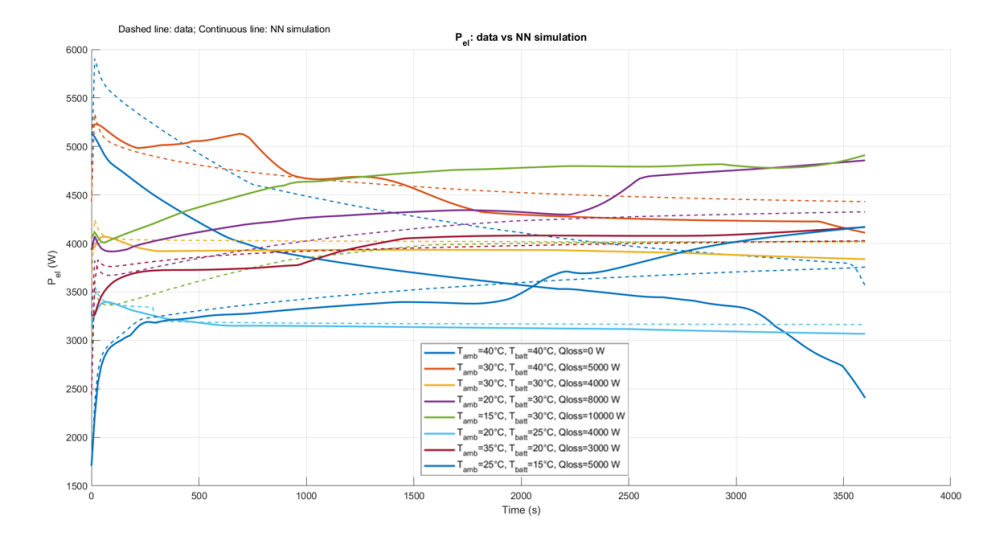


Figure 98 NN F

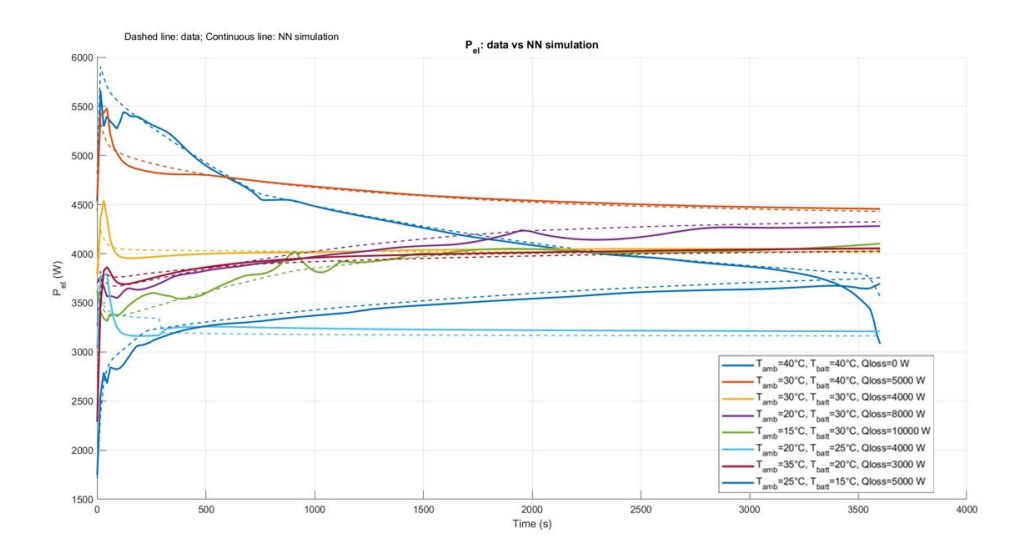


Figure 99 NN G

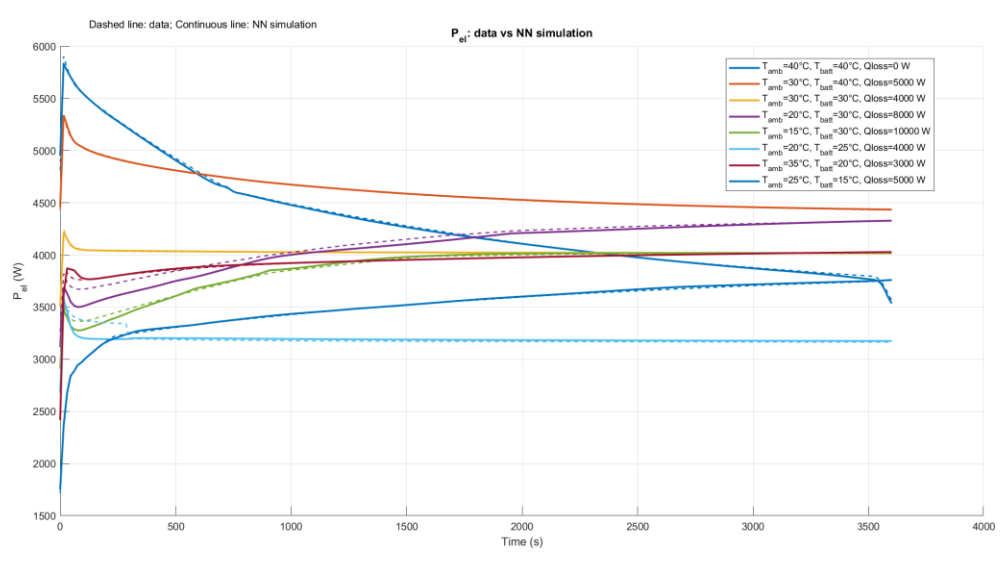


Figure 100 NN H

The comparative analysis of the neural-network configurations reveals a coherent progression in accuracy driven primarily by the informativeness of the input set and, to a lesser extent, by architectural choices (depth, width, activation). Baseline models with three inputs (Tamb, Ts_batt, Qloss) exhibit relatively high errors: **NN A** (Swish, 2 hidden layers × 8 neurons) attains RMSE_train=461.65W, indicating that limited capacity constrains the mapping from coarse thermal descriptors to *Pel.* Increasing capacity at fixed inputs improves performance: **NN B** (Swish, 2×64) reduces RMSE_sim to 362.25W, whereas replacing Swish with ReLU at identical width/depth (**NN C**, ReLU, 2×64) degrades accuracy to RMSE_train=488.57W and RMSE_sim=467.83W.

This contrast isolates activation choice as a relevant factor, with Swish's smooth, nonmonotonic response better capturing the mild nonlinearities typical of thermal-electrical couplings than piecewise-linear ReLU.

Introducing short-term state information through Ts_batt_prev_yields a clear step forward even at constant width: **NN D** (Swish, 2×64; 4 inputs: Tamb, Ts_batt, Ts_batt_prev, Qloss) reaches RMSE_train=431.87W and RMSE_sim=340.39W, showing that minimal temporal context helps the network disambiguate transients that temperatures alone cannot resolve. Deepening the network architecture by increasing the number of layers, while maintaining a fixed number of inputs and outputs, further enhances the predictive accuracy of the neural network: **NN E** (Swish, 3×64) improves to RMSE_train=416.22W and RMSE_sim=308.76W, consistent with added hierarchical feature extraction; by contrast, widening substantially at the same depth (**NN F**, Swish, 3×256) yields only a marginal gain (RMSE_train=411.60W; RMSE_sim=304.95W), suggesting diminishing returns from brute-force capacity once a minimal temporal feature is present.

The most pronounced accuracy gains arise when coolant-loop information is incorporated, aligning with first-principles heat-balance considerations for cooling power: adding the coolant mass-flow rate mdot_co (**NN G**, Swish, 3×64 ; 5 inputs) reduces errors dramatically to RMSE_train=97.92W and RMSE_sim=62.30W, reflecting the direct influence of flow-driven heat removal on compressor/fan/pump electrical demand. Replacing mdot_co with the coolant temperature rise Δ Tco=Tco,in-Tco,out (**NN H**, Swish, 3×64 ; 5 inputs) delivers the best results by a wide margin—RMSE_train= 20.45W and RMSE_sim=20.98W.

Across all the models, the **NN H** configuration, which incorporates Δ Tco as a key input, achieved the best performance, proving to be the most accurate and reliable model for Pel estimation.

Model selection and performance validation

After selecting the **neural network architecture** H that demonstrated the best performance in terms of accuracy and generalization, a more in-depth analysis of the training and testing phases is conducted. The training process lasted approximately two hours and involved 350,000 iterations. During this phase, the network progressively minimized the loss function, as shown in Figure 101, which displays the evolution of both the training and validation loss. The convergence behaviour and the absence of significant overfitting confirm the effectiveness of the learning strategy and the regularization techniques adopted.

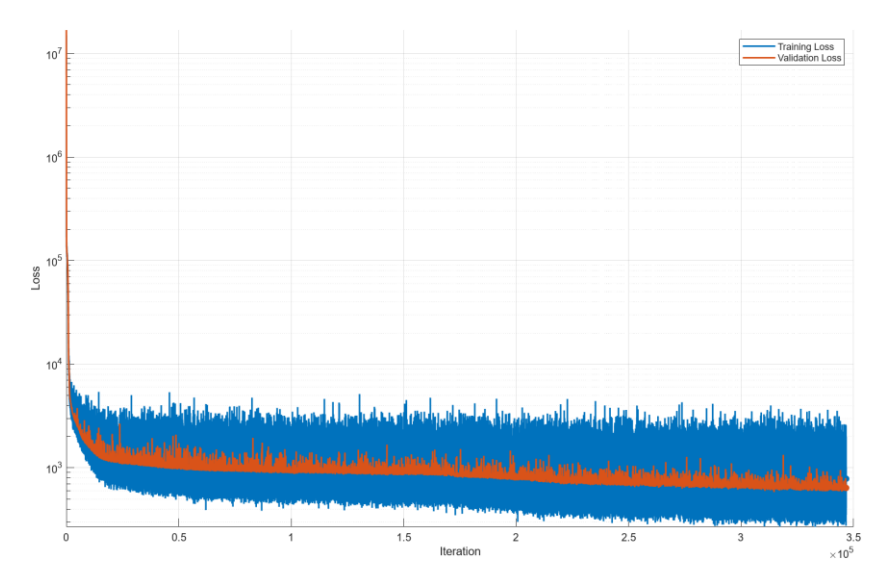


Figure 101 Training and validation loss over epochs for NN Pel

Once training is completed, the network is tested on previously unseen operating conditions, consistently demonstrating excellent predictive capabilities. The high level of agreement between the simulated and reference values confirms the network's ability to generalize beyond the training data and to provide reliable estimations across a variety of conditions.

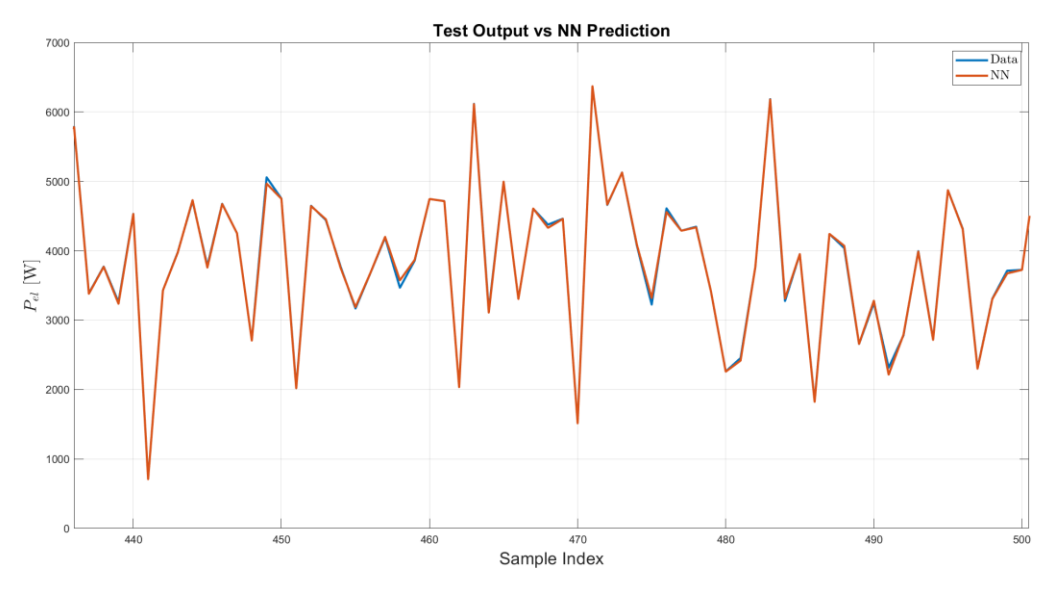


Figure 102 Pel- qualitative analysis: Test output vs NN prediction

4.4 Cabin Cooling mode (CC)

Problem definition

Cabin cooling is a critical function in automotive HVAC systems, especially in electric vehicles where thermal loads impact both passenger comfort and energy consumption. To support efficient thermal management, a neural network model is developed to estimate the cooling power (Pel) based on key operating parameters. This data-driven approach captures the nonlinear behaviour of the system and enables accurate prediction across a range of conditions.

Cabin Cooling Dataset - EFFEREST

The **EFFEREST** dataset of cabin heating mode HVAC has the following information:

Initial Conditions for generating data

- HVAC inlet air temperature (T_A_HVAC_in_degC =[45,40,35,30,25,20,15,10])
- Ambient temperature (T ambient degC =[45,40,35,30,25,20,15,10])
- Inlet air relative humidity (rH_A_HVAC_in_pct =[30,40,50,60,70,80,90])
- Setpoint evaporator outlet air temperature (SP_T_A_Evap_out_degC =[5,10,15])
- Blower control signal (blower_pct =[100,80,60,40,30,20])

Time-Series Signals (sampled at 0.1s)

- HVAC outlet air temperature (T_A_HVAC_out_degC)
- HVAC outlet air mass flow rate (mdot_A_HVAC_out_kgph)
- HVAC outlet air relative humidity (rH_A_HVAC_out_pct)
- Compressor electric power (Pel_Comp_W)
- Fan electric power (Pel Fan W)
- Blower electric power (Pel_Blower_W)
- Air-side evaporator heat load (Q_A_Evap_W)

Simulation of the Neural Network - Estimation of P_{el}

In cabin cooling mode, an accurate estimation of the total electric power consumption (Pel) is essential for both optimising system performance and enabling real-time control strategies in vehicle thermal management.

The target variable Pel is defined as the sum of the main electrical loads of the HVAC system:

$$P_{el} = P_{el\ comp} + P_{el\ Fan} + P_{el\ blower}$$

To simulate the total electric power consumption (*Pel*) in cabin cooling mode, three neural networks are developed and compared to determine the best-performing model. The difference between these networks is in the set of input features:

Neural Network L:

- **Input Layer**: 4 neurons
 - Ambient temperature (Tamb)
 - Setpoint evaporator outlet air temperature (SP evap)
 - Air-side evaporator heat load (Q_A_evap)
 - Air temperature difference of the battery coolant (deltaT_A = T_A_HVAC_out
 T A HVAC in)
- Output Layer: 1 neuron
 - Electric power (Pel)

Neural Network M:

- **Input Layer**: 4 neurons
 - Ambient temperature (Tamb)
 - Setpoint evaporator outlet air temperature (SP evap)
 - Air-side evaporator heat load (Q A evap)
 - HVAC outlet air mass flow rate (mdot_A)
- Output Layer: 1 neuron
 - Electric power (Pel)

Neural Network N:

- **Input Layer**: 5 neurons
 - Ambient temperature (Tamb)
 - Setpoint evaporator outlet air temperature (SP_evap)
 - Air-side evaporator heat load (Q_A_evap)
 - HVAC outlet air mass flow rate (mdot_A)
 - Air temperature difference of the battery coolant (deltaT_A = T_A_HVAC_out
 T_A_HVAC_in)
- Output Layer: 1 neuron
 - Electric power (Pel)

All three neural networks are built on a common architecture, summarized as follows:

- Hidden layers:
 - 3 hidden layers with 64 neurons each

Activation function: <u>Swish</u>

- Training details:

o Batch size: 2048

o Epochs: 50

Optimizer: Adam (adaptive moment estimation)

○ Learning Rate: 5 × 10⁻³

A comparative analysis is performed to evaluate the effectiveness of three neural network configurations, all trained and validated in MATLAB. Model performance is quantitatively assessed using Root Mean Squared Error (RMSE) through a two-step evaluation process. First, a global RMSE on the test dataset and validation process provides a consistent benchmark across all models. Second, a targeted simulation RMSE is computed on representative time sequences to critically appraise each model's proficiency in replicating complex transient dynamics.

The analysis reveals a clear progression in predictive accuracy. The initial configuration, using the input features [T_amb, SP_Evap, Q_A_evap, Δ T_air], demonstrates satisfactory performance with a training RMSE of 172.50 W and a simulation RMSE of 144.90 W. A significant improvement is observed when the input Δ T_air is replaced with the mass flow rate, mdot _A. This modification reduces the training RMSE to 147.05 W and, more notably, the simulation RMSE to 90.49 W, indicating a superior ability to model dynamic behaviour. Ultimately, the best overall performance is achieved by a combined model incorporating all available inputs, which yields the lowest errors of 137.11 W (training) and 84.56 W (simulation), confirming that this comprehensive feature set provides the most accurate and dynamically consistent model.

Configuration	Inputs	RMSE training (W)	RMSE simulation (W)
NN L	Tamb, SP_evap, Q_A_evap, deltaT_A	172.5	144.90
NN M	Tamb, SP_evap, Q_A_evap, mdot _A	147.05	90.49
NN N	Tamb, SP_evap, Q_A_evap, mdot _A, deltaT_A	137.11	84.56

Table 10 Testing and simulation RMSE for each Cabin Cooling neural network configuration

A qualitative analysis is conducted to evaluate the efficacy of three distinct neural network (NN) models in accurately representing the real-world behaviour of a system. Specifically, each model

is tasked with simulating identical reference curves, and their electrical power outputs (Pel) are rigorously compared against the corresponding available experimental data. The evaluation is based on four key criteria: qualitative adherence to reference data, accuracy in the transient phase, temporal stability, and consistency across diverse operational conditions.

The first neural network, **NN L**, exhibited significant limitations. Its adherence to experimental data is only partial, with visible deviations observed across multiple curves, particularly under high-power conditions. The model demonstrates a weak representation of the system's initial transient phase, failing to accurately capture its early-stage dynamics. While overall stability is sufficient, the simulations are not lacking minor irregularities. Furthermore, consistency across different operational scenarios is highly variable, leading to heterogeneous performance from case to case.

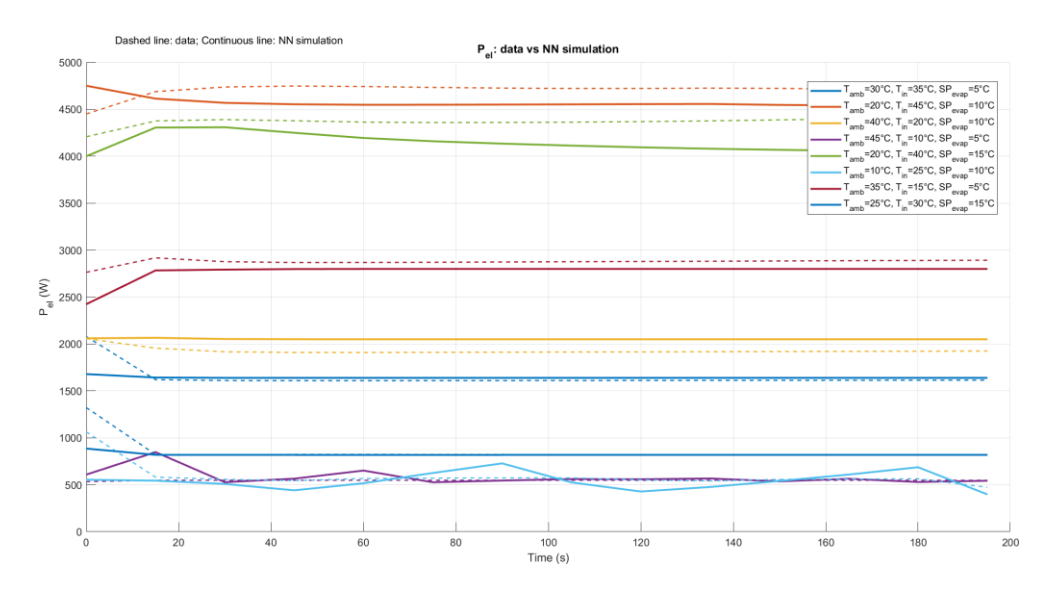


Figure 103 NN L

A substantial improvement is observed in the second model version, **NN M**. This iteration showed markedly enhanced precision in tracking the experimental data, with a much closer overlap between simulated and real curves, especially in high-power scenarios. Its performance in the transient phase is also superior, although minor discrepancies persist under certain conditions. The model exhibited good temporal stability without anomalous oscillations, and its consistency across various cases is generally satisfactory, despite slight performance variations.

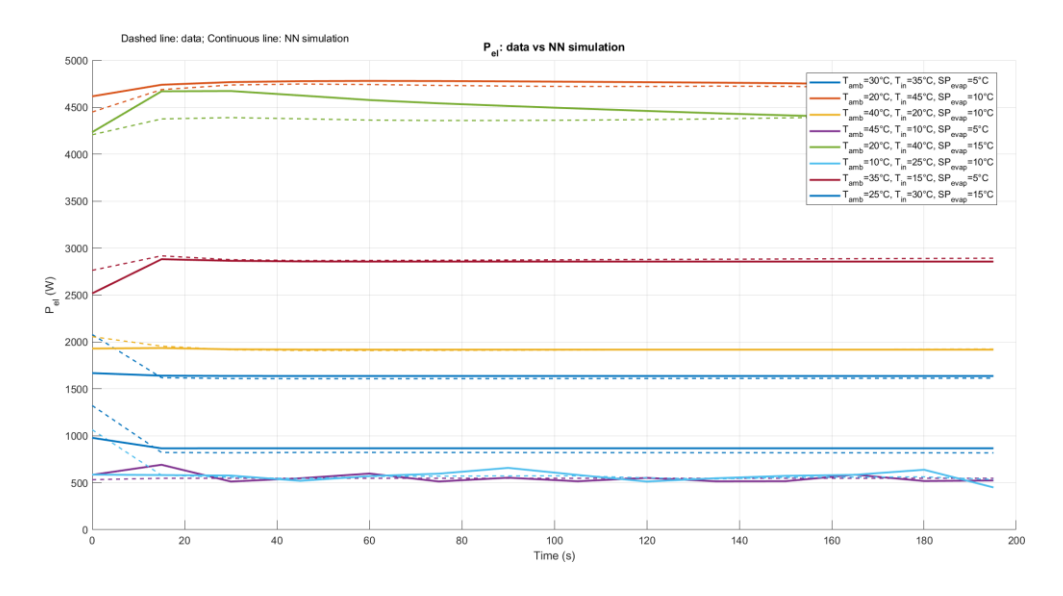


Figure 104 NN M

The third version, **NN N**, represents the greatest outcome. Its simulations demonstrate high adherence to the experimental data, with output curves precisely following the real system's behaviour throughout the entire temporal interval. The model exhibits a superior ability to capture transient dynamics, coupled with enhanced stability that yields smoother output curves and highly consistent performance across all operational conditions.

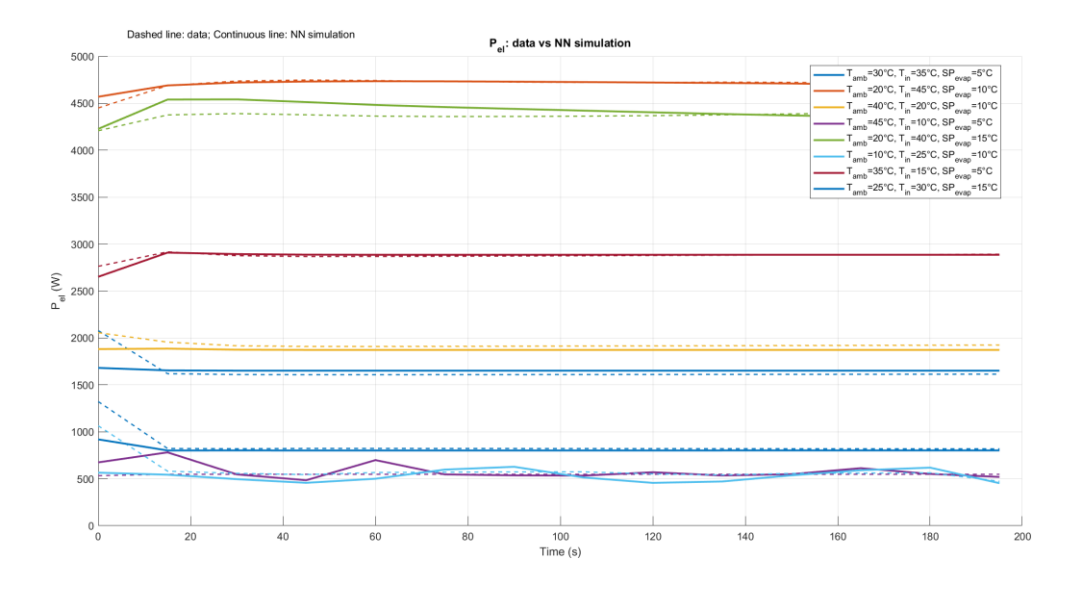


Figure 105 NN N

Model selection and performance validation

The analysis demonstrates a clear progression in performance with each iterative enhancement of the model architecture. Among the evaluated networks, **Neural Network N** emerges as the most accurate, stable, and generalizable version. Its superiority is quantitatively confirmed by its

optimal Root Mean Squared Error (RMSE), establishing it as the most suitable candidate for simulating the Cabin Cooling Mode across diverse operating conditions.

The robustness of Neural Network N is further reinforced by its training history. The network undergoes nearly 400,000 iterations, effectively minimizing the loss function to values on the order of 10²(log scale). As depicted in Figure 106Figure 106 Training and validation loss over epochs for NN PelFigure 106, the training and validation loss curves exhibit smooth and stable convergence without indications of overfitting, affirming the effectiveness of the learning strategy and regularization methods employed.

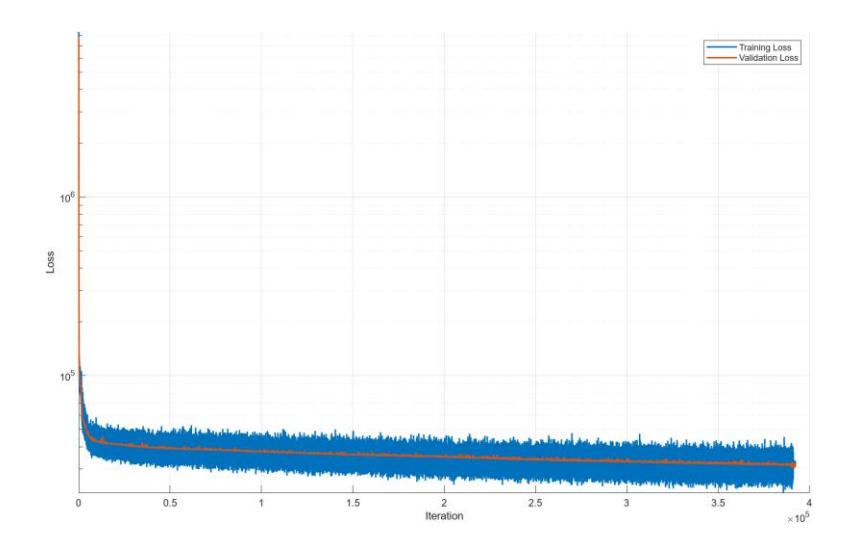


Figure 106 Training and validation loss over epochs for NN Pel

Generalization capability is conclusively validated through testing on previously unseen data. The predictions show close alignment with experimental measurements, confirming that the model accurately captures the underlying thermal dynamics. These results solidly establish Neural Network N as a reliable and generalizable solution for real-world simulation of the Cabin Cooling Mode.

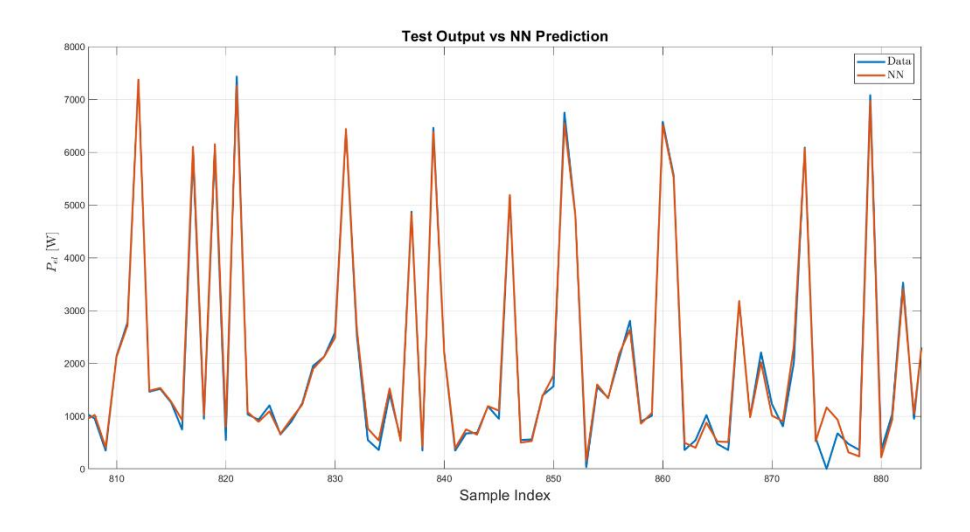


Figure 107 Pel- qualitative analysis: Test output vs NN prediction

4.5 Cabin Heating mode (CH)

Problem definition

Cabin heating is a key function in automotive HVAC systems, especially in electric vehicles where waste-heat sources are limited. To ensure comfort with minimal impact on energy consumption, a neural network model is developed to estimate the heating power (Pel) from key operating parameters, capturing system nonlinearities and enabling accurate performance prediction.

Cabin Heating Dataset – EFFEREST

The **EFFEREST** dataset of cabin heating mode HVAC has the following information:

Initial Conditions for generating data

- HVAC inlet air temperature (T_A_HVAC_in_degC =[-20,-15,-10,-5,0,5,10,15,20])
- Inlet air relative humidity (rH_A_HVAC_in_pct =[20,40,60,80,100])
- Setpoint Coolant-to-Air Heat Exchanger (CoHX) inlet air temperature (SP_T_C_CoHX_in_degC=[25,35,45,55,65,75,85])
- Blower control signal (blower_level_pct=[100,80,60,40,20])

Time-Series Signals (sampled at 0.1s)

- HVAC outlet air temperature (T_A_HVAC_out_degC)
- HVAC outlet air mass flow rate (mdot A HVAC out kgph)
- Blower electric power (Pel_Blower_W)
- PTC electric power (Pel_PTC_W)

- Pump2 electric power (Pel_Pump2_W)
- HVAC outlet air relative humidity (rH A HVAC out pct)
- Air-side CoHX heat load (Q_A_CoHX_W)

Simulation of the Neural Network - Estimation of P_{el}

In cabin heating mode, accurate estimation of the total electrical power consumption (Pel) is crucial for system optimisation and real-time thermal management. The target variable is defined as the sum of the main HVAC electrical loads:

$$P_{el} = P_{el\ PTC} + P_{el\ numn2} + P_{el\ blower}$$

To simulate the total electric power consumption (*Pel*) in cabin heating mode, three neural networks are developed and compared to determine the best-performing model. The difference between these networks is in the set of input features:

Neural Network P:

- **Input Layer:** 5 neurons
 - HVAC inlet air temperature (T_A_HVAC_in_degC)
 - Setpoint Coolant-to-Air Heat Exchanger (CoHX) inlet air temperature
 (SP_T_C_CoHX_in_degC)
 - Air-side CoHX heat load (Q A CoHX W)
 - HVAC outlet air mass flow rate (mdot_A_HVAC_out_kgph)
 - Air temperature difference of the battery coolant (deltaT_A = T_A_HVAC_out
 T_A_HVAC_in)
- Output Layer: 1 neuron
 - Electric power (Pel)

Neural Network Q:

- Input Layer: 4 neurons
 - Blower control signal (blower_level_pct)
 - Air-side CoHX heat load (Q_A_CoHX_W)
 - HVAC outlet air mass flow rate (mdot A HVAC out kgph)
 - Setpoint Coolant-to-Air Heat Exchanger (CoHX) inlet air temperature
 (SP_T_C_CoHX_in_degC)
- Output Layer: 1 neuron

Electric power (Pel)

Neural Network R:

Input Layer: 5 neurons

HVAC inlet air temperature (T_A_HVAC_in_degC)

Blower control signal (blower_level_pct)

Air-side CoHX heat load (Q_A_CoHX_W)

HVAC outlet air mass flow rate (mdot_A_HVAC_out_kgph)

 Setpoint Coolant-to-Air Heat Exchanger (CoHX) inlet air temperature (SP_T_C_CoHX_in_degC)

Output Layer: 1 neuron

Electric power (Pel)

All three neural networks are built on a common architecture, summarized as follows:

- <u>Hidden layers</u>:

■ <u>3 hidden layers</u> with <u>64 neurons</u> each

Activation function: <u>Swish</u>

Training details:

o Batch size: 2048

o Epochs: 50

o Optimizer: Adam (adaptive moment estimation)

○ Learning Rate: 5×10^{-3}

A quantitative analysis is conducted to evaluate the performance of the three neural networks, which are distinguished by their input features. The first network, with inputs [T_in, SP_col, Q_CoHX, mdot_out, dT_air], yielded a training RMSE of 453.30 W and a simulation RMSE of 331.34 W. The second network, utilizing the reduced input set [blower_level, Q_CoHX, mdot_out, SP_col], resulted in a training RMSE of 573.30 W and a simulation RMSE of 331.94 W. The third configuration, with inputs [T_in, blower_level, Q_CoHX, mdot_out, SP_col], showed the highest errors, with a training RMSE of 594.10 W and a simulation RMSE of 339.27 W.

It is important to note the distinction between these error metrics. The training RMSE is computed on random sequences of previously unseen combinations, leading to inherent variability and providing only a partial assessment of robustness. In contrast, the simulation RMSE is calculated on a consistent, standardized dataset for all models, making it a more reliable and valid benchmark for comparative performance.

On this basis, the second network demonstrates the most favourable balance. Despite its higher training error and reduced number of inputs, it maintains a simulation accuracy nearly identical to the first, more complex network.

Configuration	Inputs	RMSE training (W)	RMSE simulation (W)
NN P	T_in, SP_col, Q_coHX, mdot out, dT air	453.3	331.34
NN Q	blower_level, Q_coHX, mdot_out, SP_col	573.3	311.94
NN R	T_in, blower_level, Q_coHX, mdot_out, SP_col	594.1	339.27

Table 11 Testing and simulation RMSE for each Cabin Heating neural network configuration

A qualitative comparison of the neural network predictions against real experimental data reveals significant insights into their dynamic behaviour, particularly during transient phases.

The models generally demonstrate good accuracy in predicting steady-state power values (Pel), as indicated by the close alignment of the solid prediction lines with the dashed real-data lines under constant conditions. However, a critical limitation is observed in the networks' ability to accurately capture transient responses.

In cases with high power peaks followed by steep decays (e.g., the green curve), the model tends to overestimate the magnitude and accentuate the transient, failing to reproduce the dynamic variations. Conversely, for lower-amplitude transients (e.g., the yellow curve), the response of the network appears delayed and attenuated, highlighting its ability in capturing fine temporal dynamics with sufficient accuracy.

This inaccuracy may derive from limitations in the training data. The experimental protocol set many parameters as constant inputs to observe the system's dynamic response to other variables. Therefore, the dataset could result not sufficiently representative of operating conditions with a sharp power reduction in steady state.

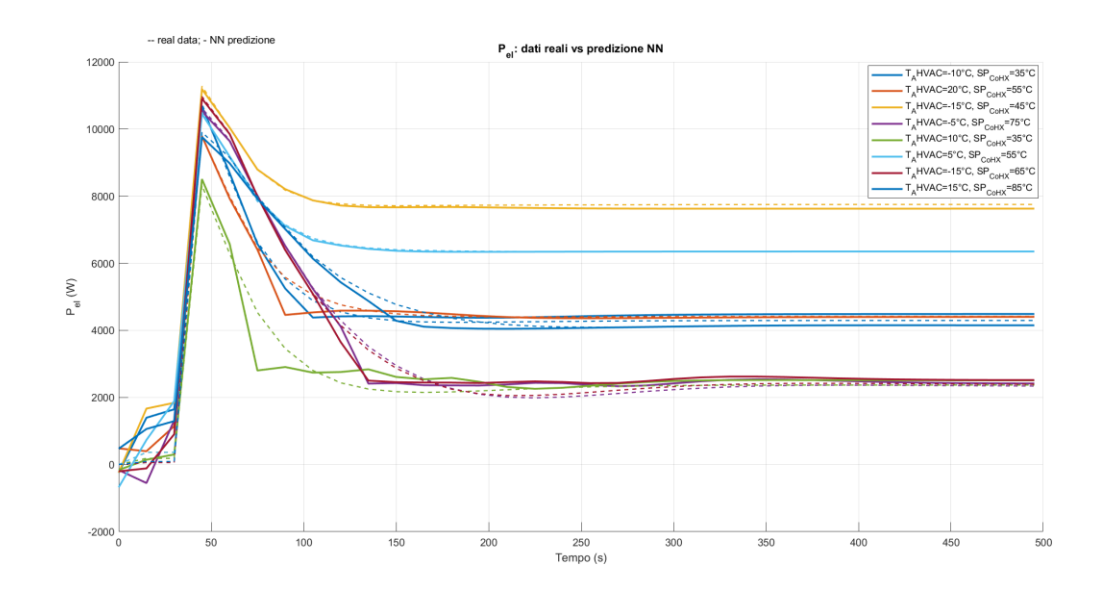


Figure 108 NN P

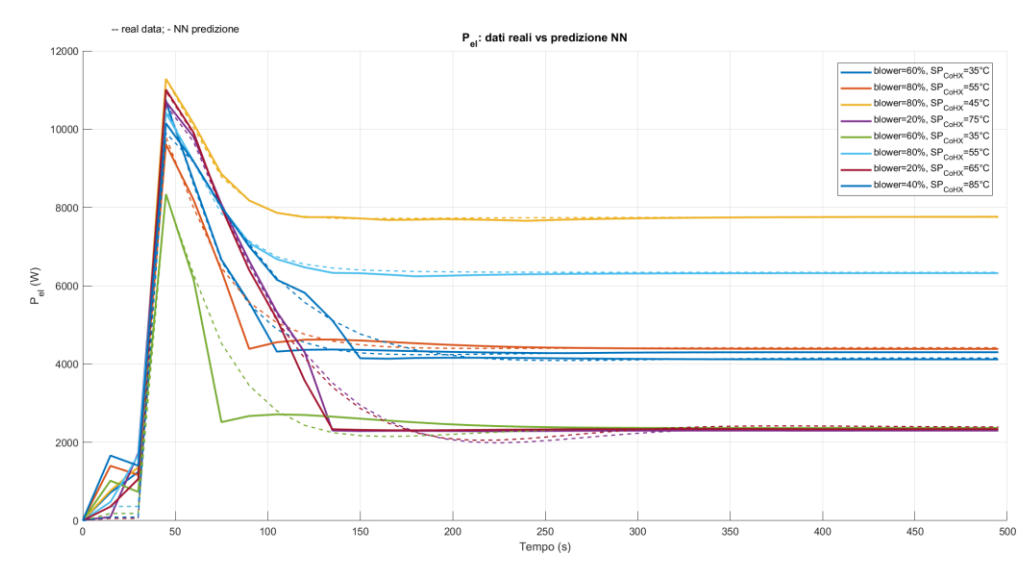


Figure 109 NN Q

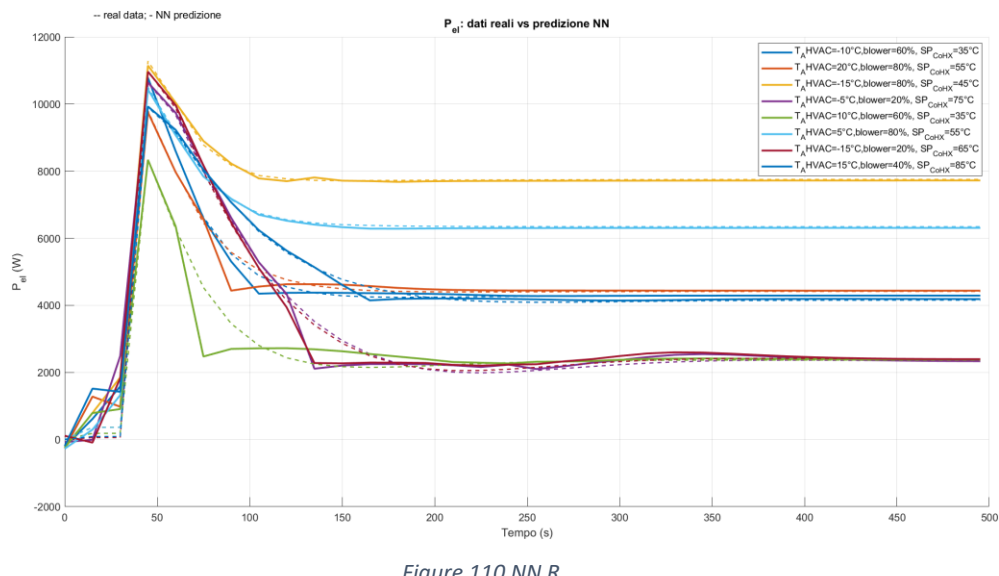


Figure 110 NN R

Between the networks, the second configuration NN Q demonstrates the most favourable balance. A key advantage is its consistent prediction that are coherent with physic, as the model doesn't estimate any negative Pel value. Furthermore, it achieves robust steady-state performance with a reduced input set, making it the most efficient and generalized model, despite the inherent dataset limitations for a fully accurate dynamic representation.

Model selection and performance validation

Considering the training history of Neural Network Q, the model demonstrates a notable increase of robustness, as training iterations progress. Following a rapid initial decrease, both the training and validation losses converge and stabilize around a value of approximately 104. Although some fluctuations remain visible, the overall trend suggests that the network has reached a stable learning regime.

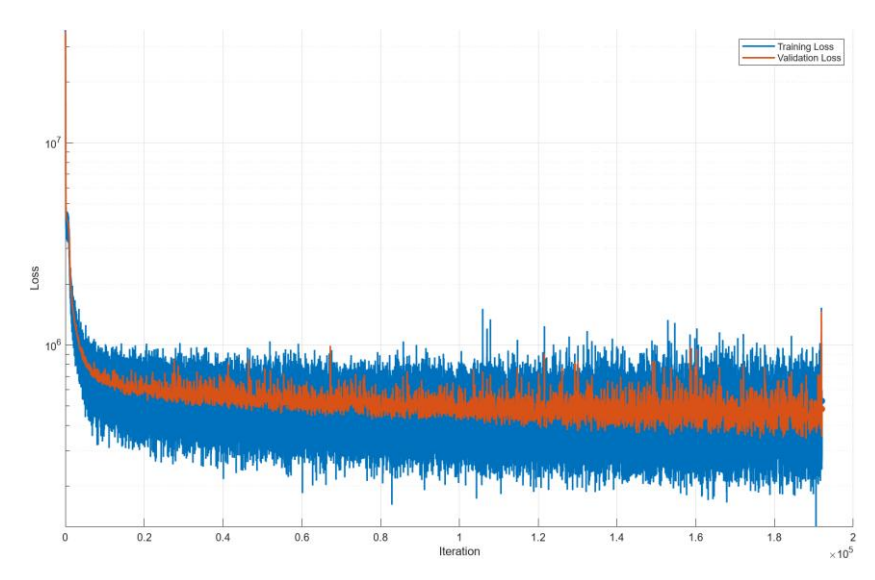


Figure 111 Training and validation loss over epochs for NN Pel

The performance of **Neural Network Q** is further evaluated on a test dataset. As shown in Figure 112, the predicted output (orange) closely matches the actual data (blue) across most samples, confirming the model's good generalization capability. A slight discrepancy is observed in correspondence with a transient, where the network struggles to fully capture the rapid change. Despite this, the overall prediction accuracy remains high, supporting the effectiveness of the trained model.

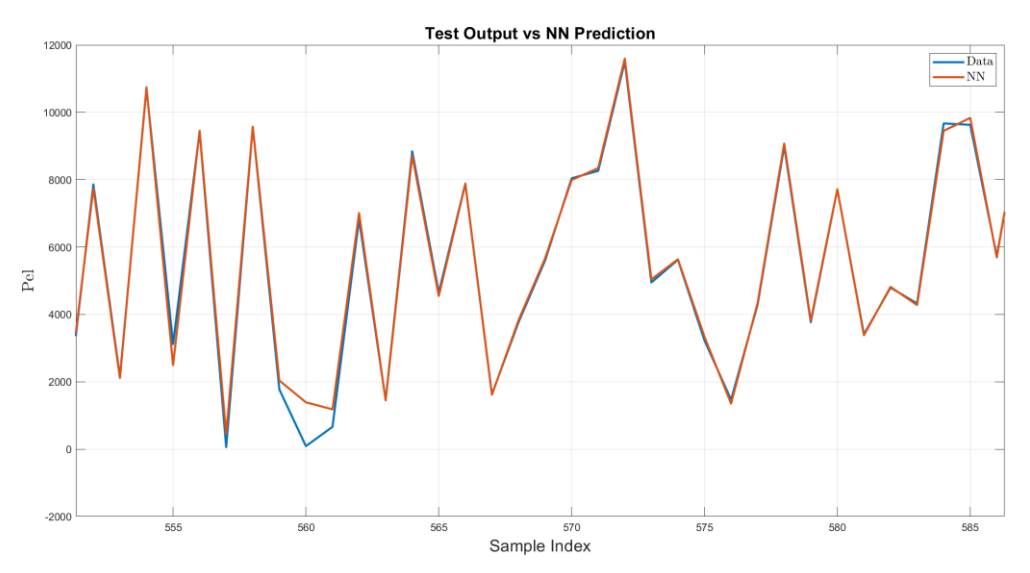


Figure 112 Pel- qualitative analysis: Test output vs NN prediction

4.6 Integrated Model for Thermal Modes

After generating and analysing the four modes predicted by the Thermal Management system, a complete model is created in Simulink. Since the modes cannot be activated simultaneously, the system provides for an exclusive selection. The user is then prompted to specify the desired mode as input, corresponding to:

- Mode 1 → Battery Heating (BH)
- Mode 2 → Battery Cooling (BC)
- Mode 3 → Cabin Cooling (CC)
- Mode 4 → Cabin Heating (CH)

Within the Simulink model, a *Variant Subsystem* has been used for each mode: based on the value of the input mode, only the corresponding subsystem is activated. Each subsystem is implemented individually and uses user-chosen inputs from the data in the database. This modular design provides greater clarity in the model, facilitates maintenance and allows for possible extension to additional operating modes.

```
% === mode ===
% 1 = BH
% 2 = BC
% 3 = CC
                                                        mode 1 BH
% 4 = CH
mode = 4;
switch mode
    case 1
        Tamb = 0; % [°C]
                                                        mode 2 BC
        Tbatt = -5; % [°C]
        Qloss = 5000; % [W]
        . . .
    case 2
        Tamb = 15; % [°C]
                                                        mode 3 CC
        Tbatt = 40; % [°C]
        Qloss = 2000; % [W]
                                                        mode 4 CH
```

Figure 113 Unified Simulink model covering all four modes

To evaluate the performance of the model under realistic operating conditions, test cases are considered. The system then runs a full simulation for the chosen configuration, and two key indicators are recorded:

- Computation time to evaluate how quickly the neural network returns valid output;
- *Prediction accuracy* assessed via the Root Mean Square Error (RMSE) between the network output and the baseline data.

The test is repeated for different combinations of input modes and conditions, as shown in the following table.

Mode	Inputs	Simulation Time (s)	RMSE simulation (W)
ВН	Tamb = 25°C, Tbatt=-20°C, Qloss=4000 W	0.317	2.2984
ВН	Tamb=30°C, Tbatt=-10°C, Qloss=8000 W	0.374	3.2723
ВН	Tamb=-15°C, Tbatt=20°C, Qloss=2000 W	0.427	1.1259
ВН	Tamb=0°C, Tbatt=-5°C, Qloss=5000 W	0.276	0.6252
ВС	Tamb=20°C, Tbatt=30°C, Qloss=8000 W	0.150	60.1550
ВС	Tamb=30°C, Tbatt=15°C, Qloss=4000 W	0.153	6.1192
ВС	Tamb=40°C, Tbatt=15°C, Qloss=6000 W	0.149	12.8090
ВС	Tamb=15°C, Tbatt=40°C, Qloss=0 W	0.185	23.5134
СС	Tamb=20°C, Tin=40°C, SP _{evap} =15°C	0.150	23.3075
СС	Tamb=35°C, Tin=15°C, SP _{evap} =5°C	0.163	29.7905
СС	Tamb=45°C, Tin=45°C, SP _{evap} =5°C	0.114	47.3018
СС	Tamb=30°C, Tin=20°C, SP _{evap} =10°C	0.155	30.5242

СН	blower=100%, SP _{CoHX} =45°C	0.181	322.1938
СН	blower=20%, SP _{COHX} =35°C	0.156	363.9424
СН	blower=60%, SP _{COHX} =85°C	0.173	93.9526
СН	blower=80%, SP _{COHX} =55°C	0.163	96.8090

Table 12 Computation Time & RMSE Across Modes and Inputs

As can be seen, the results confirm that the model provides accurate predictions in a very short time (\approx 0.2 seconds), demonstrating its suitability for real-time applications or for integration into embedded systems.



Figure 114 Computational time across different modes

The following graphs show the results produced by neural networks for the different modes using the combinations described in the table. In each graph there are also the corresponding lines of real data, and from the comparison it can be seen that the neural network is very effective in all cases.

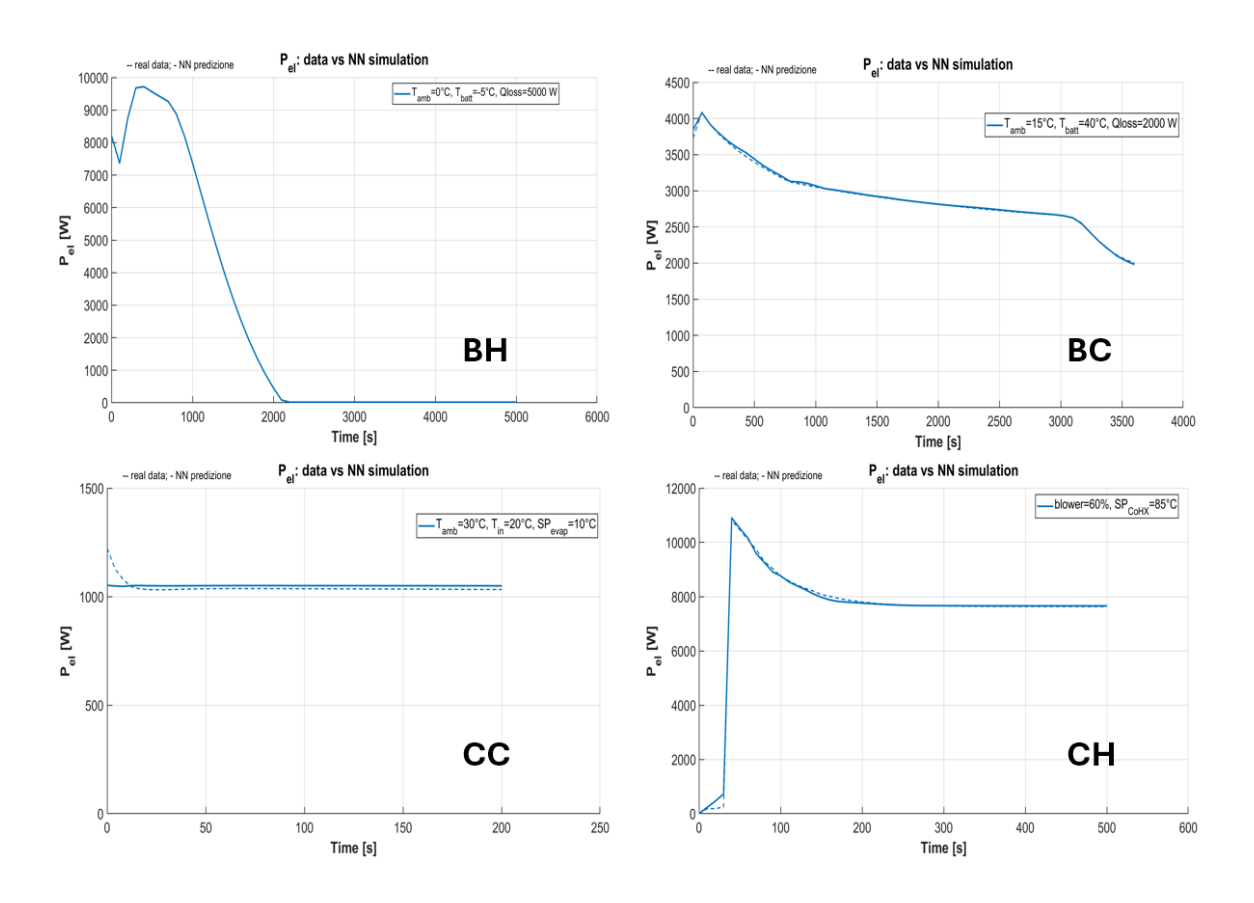


Figure 115 Neural network results and real data for the different modes (in order: BH, BC, CC, CH)

Comparative Analysis of Physics-Based and Neural Network Modelling Approaches

This chapter proposes a comparison between the Physics-based and data-driven models, based on a critical analysis of their distinctive characteristics, advantages and limitations.

Complexity and implementation

The *Physics-based model* is inherently very sophisticated from the early stages of development. Although simplified formulations have been developed with the aim of reducing the computational demands, a substantial part of the model take recourse in coefficients derived by fitting operations. These fitted parameters are difficult to replicate in different scenarios and often require complex experimental campaigns to be validated. The consequence is that the reliability of the model continues to rely heavily on the context within these parameters are obtained and their accuracy. In fact, even small inaccuracies in their determination make the output deviate by large amounts, compromising the ability of the model to produce consistent and reproducible results. In other words, having fitted coefficients makes the entire system fragile: the more the complexity of the model is reduced through simplifications, the more the need to overcompensate with accurate fittings increases, which however reduce the overall robustness. While the models of the individual components (compressor, condenser, evaporator and expansion valve) provide valuable information on local phenomena, their combination into a complete cycle highlights this dependence on fitted parameters, showing problematic consistency and reliability replicating in matching the performance of a real system over a wide range of operating conditions.

The *data-driven model* is based upon a reversed scheme in relation to Physics-based models. The construction of a neural network requires a long and accurate training process, which involves the collection of large amounts of data representative of the system, the selection of a suitable architecture, and the parameter tuning through the utilization of iterative approaches that can be particularly expensive both in terms of time and computational resources. In addition, during the validation phase, there is also the need to check the model for its ability to generalize well to new data, and this implies additional testing, tuning, and potentially multiple iterations of retraining. This initial complexity represents a significant barrier, especially in scenarios where data is scarce or difficult to acquire.

However, once the training is complete and a validated model is obtained, the implementation of the network is surprisingly simple. In a development environment, executing a trained neural network is

typically computationally efficient, making such models especially well-suited for real-time applications, including predictive control, dynamic system monitoring, and automated diagnostics. This benefit of paying a high cost of training initially but with simplicity of operational implementation is a strength of data-driven neural models, especially in tasks where speedy

Accuracy and predictive power

computation and model adaptability are relevant issues.

The *Physics-based model* aims to reproduce thermal dynamics through the formulation of the principles of thermodynamics. The results show that, while the model is based on solid theoretical foundations, it captures the general behaviour of the reference refrigeration cycle but with some differences in detail. These differences do not originate from systematic errors in the formulation, but from the complex parametric calibration and simplifications introduced, which compromise the fidelity of the model by reducing its predictive reliability in real contexts.

In the *data-driven model*, numerous attempts at configuration and training have provide the capability to obtain reproductions that are more similar to real data. However, its accuracy is not uniform: while in certain operating regimes the deviations are negligible, in others there are greater discrepancies. This sensitivity depends both on the quality and consistency of the training dataset, as well as on the ability of the input features to adequately represent the intrinsic Physics-based dynamics. A paradigmatic case is thermal prediction: although the network with reasonable accuracy predicts the time derivative of the battery temperature (dTbatt/dt), the numerical integration of this signal gives an excessively linearized trend, unable to reproduce the complex nonlinearity of the real phenomenon.

Robustness

The *Physics-based model* has the advantage of being able to be used in any condition, since it is not based on a dataset for training, but on well-defined Physics-based principles, expressed through mathematical equations. This allows the model to be used from the early stages of design, even in hypothetical scenarios or not yet experimentally verified. However, the practical application of these models is often limited due to the high level of detail required and the complexity associated with the calibration phase. These aspects reduce its effectiveness and flexibility in operational contexts, particularly for real-time control applications.

The *data-driven model*, once trained, is faster and more efficient than a Physics-based model, but has less capacity for generalization. The neural network effectively learns the data provided during training, but its reliability is reduced when it is applied to conditions not represented in the training dataset. Therefore, if the data used for training do not cover the different operating conditions in a representative way, the model may face significant difficulties in providing accurate predictions in scenarios not previously observed.

Computational efficiency

The *Physics-based model* involves a high computational load, especially when it involves the integration of multiple thermodynamic subsystems. This complexity results in long simulation time, approximately 0.7 seconds per run (Figure 22 Computational time in the refrigerant circuit modelFigure 22), and significant compute resource utilization. These characteristics strictly limit their use within predictive control algorithms, where fast response times and high operational efficiency are required.

The *data-driven model*, on the other hand, involves a high computational cost in the initial training phase, which is particularly complex and time-consuming, ranging from 1 to 10 hours. However, once the training is complete, the neural network offers an extremely fast execution, with an average computational time of 0.2 seconds (Table 12 Computation Time & RMSE Across Modes and Inputs). This makes it well-suited for integration into real-time simulations and predictive control algorithms.

6. Conclusion

In this thesis work, a Thermal Management System (TMS) model for electric vehicles was developed, with the primary objective of faithfully reproducing the behaviour of the real system.

The research is organized through modelling, comparison of analysis and validation of different methods approaches, to identify the most effective solution in terms of guaranteeing passenger comfort and safety of critical car components. The ultimate goal is achieved by maintaining the optimal temperature ranges for the battery, electric motors and power electronics, which are essential conditions to ensure both operational efficiency and overall vehicle safety.

The modelling began with the implementation of a simplified Physics-based method, which was then compared to a high-fidelity model made in Simscape by MathWorks, taken as a reference. At the same time, the study of the system's behaviour was deepened through the creation of benchmark models, aimed at isolating and analysing the dynamics of the individual main components.

A parallel line of research explored the potential of a data-driven methodology, based on machine learning algorithms, thus representing an innovative complement to traditional modelling techniques. This model was refined through multiple simulations, which explored different architectures and operating conditions, allowing for continuous improvement of neural network performance and the achievement of optimal results.

From the comparative analysis of the three modelling approaches, the following significant results emerge:

- The simplified physics model stood out for its reduced simulation times (about 0.7 seconds)
 and a remarkable ability to generalize. The results obtained showed a satisfactory agreement
 with the Simscape reference model, proving to be a valid tool for preliminary analyses and
 scenarios in which speed of calculation is a priority.
- The Simscape model, developed by MathWorks, confirmed expectations in terms of accuracy
 and Physics-based detail, providing a reliable benchmark for validating the other models.
 However, this high fidelity comes with a significantly higher computational effort, which limits
 its use in contexts that require repeated simulations or rapid turnarounds.
- The data-driven model represented a virtuous compromise between the two previous methodologies, combining the advantages of the Physics-based approach in terms of efficiency, with a predictive accuracy comparable to that of the high-fidelity model. The computational performance, even faster than the simplified model, suggests its ideal

application in real-time control and online optimization contexts. The main limitation of this method lies in its reliance on a large, varied, and high-quality dataset for training.

Future developments

In conclusion, the results obtained in this study, particularly the ones related to the data driven approach can represent the foundations to develop a long-term predictive control strategy for optimizing thermal management in electric vehicles. The goal will be the design of an architecture capable of dynamically coordinating the main thermal subsystems, optimizing energy allocation, and improving both range and battery life.

Specifically, the controller will target two main domains:

- Thermal management of the cabin, minimizing energy consumption related to comfort;
- Thermal management of the battery, maintaining ideal operating conditions and reducing thermal and cyclic degradation.

The methodology involves integrating predictive thermal models with advanced control techniques, such as Model Predictive Control (MPC). The algorithm will leverage real-time operational data, environmental forecasts, and driving profile information to anticipate thermal demands and optimize control actions over extended time horizons.

The ultimate objective is to contribute to the development of intelligent technologies for sustainable electric mobility, providing an effective solution to one of the main technological barriers still present in the market.

Bibliography

- BloombergNEF. (2024). Electric Vehicle Outlook 2024. Bloomberg Finance L.P.
- Career, E. (2025, June 23). *How heating and cooling reversible heat pump works*. Tratto da YouTube: https://www.youtube.com/shorts/7qPw8bA-c68
- Condenser and Evaporator. (s.d.). MathWorks. Tratto da MATLAB & Simulink: https://uk.mathworks.com/help/hydro/ug/condenser-evaporator.html
- Dalboni, M., Tavernini, D., Concari, C., Montanaro, U., Soldati, A., Dhaens, M., & Sorniotti, A. (2021). Nonlinear model predictive control for integrated energy-efficient torque-vectoring and anti-roll moment distribution. *EEE/ASME Transactions on Mechatronics*, 1212-1224.
- Dubarry, M., & Liaw, B. Y. (2009). Identify capacity fading mechanism in a commercial LiFePO4 cell. *Journal of Power Sources*, 541-549.
- Electric Vehicle Thermal Management. (s.d.). MathWorks. Tratto da MATLAB & Simulink:
 https://uk.mathworks.com/help/hydro/ug/sscfluids_ev_thermal_management.html
- European Commission, Fit for 55. (2021). *Proposal on CO₂ standards*. Brussels.
- Filters, U. (2023, November 13). *The heat pump: The ideal solution for electric vehicles*. Tratto da UFI Filters: https://www.ufifilters.com/en/news-en/the-heat-pump-the-ideal-solution-for-electric-vehicles/
- Funke, S., & al. (2019). How much charging infrastructure do electric vehicles need? *Transportation Research Part D*, 134-150.
- Gao, L., Liu, S., & Dougal, R. A. (2002). Dynamic lithium-ion battery model for system simulation. *IEEE Transactions on Components and Packaging Technologies*, 25, 495– 505.
- Holcomb, B. (2022, October 21). How Simulation Is Used To Design ICE vs. Battery Electric Vehicle Thermal Management Systems. Tratto da Gamma Technologies: https://www.gtisoft.com/blog-post/ice-vs-xev-automotive-thermal-management-simulation/
- International Energy Agency (IEA). (2024). Global EV Outlook 2024. Paris.
- Jeffers, M., & al. (2015). Climate Control Load Reduction Strategies. *SAE Technical Paper 2015-01-0355*.
- Kim, J., Oh, J., & Lee, H. (2019). Review on battery thermal management system for electric vehicles. *Applied Thermal Engineering*, 192–212.

- Lokur, P., & al. (2024). *Thermal Management in Electric Vehicles: A Review.* Energy Reports.
- Lokur, P., Murgovski, N., & Larsson, M. (2024). Control-Oriented Model for Thermal Energy Management of Battery Electric Vehicles. *IEEE Transactions on Vehicular Technology*, 1-12.
- Luo, T., & al. (2020). Impact of Climate Control on EV Range,. SAE Technical Paper 2020-01-1374.
- Ma, S., Jiang, M., Tao, P., Song, C., Wu, J., Wang, J., . . . Shang, W. (2018). Temperature effect and thermal impact in lithium-ion batteries: A review. *Progress in Natural Science: Materials International*, 653-666.
- Master, M. (2023, October 31). Cabin heating explained: Engine cars vs. EVs (PTC heater, heat pump, and Tesla's Octovalve). Tratto da YouTube: https://www.youtube.com/watch?v=RuQ8uDbS4i4
- Moultak, A. L. (2017). Transitioning to Zero-Emission Vehicle. ICCT.
- Najman, L. (2022, Dec 15). Real Range for Electric Cars by Temperature & Weather: How temperature affects electric vehicle range. Tratto da Recurrent Research: https://www.recurrentauto.com/research/how-temperature-affects-ev-range
- Neubauer, J., & Wood, E. (2014). The impact of range anxiety and home, workplace, and public charging infrastructure on simulated battery electric vehicle lifetime utility. *Journal of Power Sources*, 257, p. 12-20.
- Nicholas, M. (2020). *Exploring Range Anxiety and Charging Infrastructure*. ICCT (International Council on Clean Transportation).
- Regulation (EU) 2019/631. (s.d.).
- TLXTechnologies. (2023). *Modular coolant valves for thermal management*. Tratto da https://www.youtube.com/watch?v=4-AzD1iuYn8
- Zhao, Z., Wang, T., Zhang, B., Wang, Y., Bao, C., & & Ji, Z. (2021). Analysis of an integrated thermal management system with a heat-pump in a fuel cell vehicle. AIP Advances, 11. doi:10.1063/5.0056364